A STUDY OF NEUTRAL MESON PRODUCTION

IN HADRONIC INTERACTIONS

Richard Mark Anthony Lucock B.Sc.

Department of Natural Philosophy

University of Glasgow

Presented for the degree of Doctor of Philosophy

in the University of Glasgow.

July 1988.

CONTENTS

TABLES

FIGURES

Acknowledgements

I would like to acknowledge the following people and institutes for their help in my work:

The SERC for providing financial support.

The Department of Physics and Astronomy of the University of Glasgow, under the direction of Professor E.W.Laing, and the High Energy Physics Group, under the direction of Professor I.S.Hughes, for providing a place and environment for work.

Many thanks also to my supervisors, Dr. R.M.Turnbull and Dr. D.Frame, for their help and guidance during my studies.

I would also like to thank Drs J.Wells, A.S.Thompson, P.J.Negus and J.G.Lynch, the students and other members of the Glasgow HEP group, and the members of the other institutes taking part in WA70.

Finally, my thanks to the support staff in the Department, especially in the computing section.

Abstract

This thesis covers the work of the author as a postgraduate student at the University of Glasgow, between October 1982 and September 1985.

The experiment WA70 was designed to study the production of high transverse momentum direct photons in hadron-hadron interactions.

The experiment took place at the CERN laboratory in Switzerland. The apparatus used was the OMEGA spectrometer facility, and a purpose built electromagnetic calorimeter. Data was taken with a hadron beam, at an energy of 280 GeV, incident on a liquid hydrogen target. The beam composition could be selected to be either negative pions, or unseparated protons and positive pions.

One of the principal features of the calorimeter was its source calibration system. Sixteen radioactive sources could be positioned within the calorimeter to provide calibration data. Much of the author's work in the early stages of the experiment was on setting up and understanding the calibration system, and on applying the results to the experiment. The work done, and the results obtained, are presented here.

One of the requirements of an experiment studying direct photon physics is the ability to accurately identify background sources of photons. The main source of such background is the decay of high transverse momentum π^0s, and to a lesser extent, ηs. The study of the production of π^0s and ηs is therefore important to the experiment.

The latter part of this thesis presents the work of the author on the study of these mesons. The aim of the analysis is to derive the cross sections for the production of high transverse momentum π^0 and η mesons. The method of analysis and the results are presented.

1. INTRODUCTION

The experiment WA70, which took place at CERN, was a collaboration of the following institutes: The University of Geneva, The University of Glasgow, The University of Liverpool, Dipartimento di Fisica dell'Università e Sezione INFN Milano, The University of Neuchâtel, and CERN. The experimental proposal was submitted in 1980, and the experiment took data from 1984 to 1986.

The experiment was designed to study the production of high transverse momentum (high P_t) direct photons in hadron-hadron interactions. A lead-liquid scintillator electromagnetic calorimeter was purpose built for this [1].

Hadrons are composite particles; their basic constituents are quarks and gluons. Both carry a colour charge, the charge of the strong force which binds these elementary particles (partons) into composite particles.

In inelastic hadron-hadron events, the interaction is generally between a single parton from each hadron, known as hard scattering. The product of the hard scattering interaction is usually two strongly charged partons. These, together with the 'spectator' partons, fragment into hadrons. The large number of particles produced makes it difficult to study the primary interaction.

This is in contrast to events where the hard scattering produces one strongly charged particle together with a 'direct' photon. Here the photon provides a 'clean' probe into the event, since it is unlikely to interact further. In addition, the electromagnetic force is described by the well understood theory of quantum electrodynamics (QED). The study of events producing direct photons is therefore an important means of studying the strong interaction.

Results of direct photon studies by members of the WA70 collaboration have been published ([2] [3] [4] [5] [6]). In addition, many other experiments have made direct

photons studies (for example, [7] [8] [9] [10] [11] [12] [13]). A full review of direct photon physics can be found in reference 14, and references therein.

The major contributions to the background in such an experiment are made by π^0 and η mesons. The π^0 is one of the main products of inelastic interactions, and decays almost exclusively (99%) into two photons. The production rate for the η is lower, but it nevertheless makes a significant contribution to the background.

Previous experiments ([7] – [13]) have shown that the production of π^0 dominates the production of direct photons at low transverse momenta. Above a P_t of about 3 GeV/c, the contribution of the direct photons becomes significant, and the proportion continues to rise with increasing P_t. At 6 GeV/c however, the ratio is still only about 40%. A proper understanding of the production of π^0 and η mesons in the experiment is therefore important.

In addition, little data has been published on high P_t π^0 cross sections prior to this experiment, although much data is available for π^- and π^+ production cross sections. This is an important point in high energy physics experiments in general, since many rely on published data to model the background via statistical simulations.

Many experiments have been done on π^0 production at transverse momenta below about 3 GeV/c, although much of this comes from proton-proton interactions only ([15] [16] [17] [18] [19]). More recent data has extended the P_t range ([20] [21] [22] [23]), although only the data in reference 23 is in a similar kinematic region to the data taken by WA70. All of these examine proton-proton interactions; pion-proton, proton-antiproton, helium-helium and deuterium-deuterium interactions have also been studied.

The data available on η production is confined to a comparison of the total cross sections of ηs and π^0s ([16] [21] [24]).

The purpose of this thesis is to derive the cross section for the production of π^0 and η at high P_t.

In addition, the work that the author did on the calibration of the detector is presented.

The WA70 calorimeter is unusual in that it uses liquid, rather than solid, scintillator. As a consequence, the basic components could not be calibrated before being built. A system employing moveable radioactive sources was designed to calibrate the fully constructed calorimeter. The author's work on this system had two aspects. One was the setting up and understanding of the calibration system, and the development of techniques to use it efficiently. The second was the study of the calibration data, to determine its accuracy and apply the results to the experimental data.

The following chapter describes the technical details of the experiment, including a description of the OMEGA spectrometer, and the electromagnetic calorimeter. Chapters 3 and 4 describe the experiment's calibration systems, and the results of the author's work with them. The fifth chapter is a description of the pattern recognition program used to reconstruct events in the calorimeter. Chapters 6 and 7 present the method and results of the analysis of the interaction data taken by the experiment. Finally, chapter 8 contains the conclusions.

2. THE WA70 APPARATUS

2.1 Introduction

The WA70 experiment was carried out at the OMEGA spectrometer facility in the West Area at CERN [25]. The OMEGA is a standard facility comprising a superconducting magnet, drift chambers and three sets of multi-wire proportional chambers. In addition, an electromagnetic calorimeter was built specifically for the experiment.

This chapter will present technical details of the OMEGA, the beamline, the calorimeter and the event trigger.

2.2 The OMEGA Spectrometer

The OMEGA magnet is a 4500 ampere superconducting magnet, generating a maximum field of 1.8 Tesla. Inside the magnet are three sets of multi-wire proportional counters (MWPC's), known as the A, B, and C chambers. In this experiment, the C chambers, normally positioned on either side of the target, were not present.

The six B chambers, positioned just downstream of the target, are designed so that the vertex position can be determined accurately. They have an aperture 150 cm wide by 95 cm high, with a chamber separation of 6 cm. The wire spacing is 2 mm in all chambers; the orientation of the wires in successive chambers alternates between (Y,U) and (Y,V), where the Y axis is horizontal, and the U and V axes are + 10.14 and − 10.14 degrees respectively from the horizontal (the wires are placed perpendicularly to the axis that they measure).

Downstream of the B chambers are the seven A chambers, whose main purpose is to define the momenta of the tracks produced in the interaction. They have a larger aperture

than the B chambers (150 cm by 120 cm high) and are are positioned at intervals of 40 cm. The wire spacing is 2 mm, as in the B chambers, but each chamber carries three wire planes in the format (Y,U,V)

In addition a single drift chamber is located at the downstream end of the magnet. This is a four plane chamber (Y,U,Y,V), with a positional accuracy of 100 microns.

The final wire chamber is a 4m by 4m MWPC mounted on the front face of the calorimeter. This was purpose built for the experiment and consists of four planes in the format (Y,U,V,Z), with a wire spacing of 4 mm.

The target used in the experiment was liquid hydrogen. This was contained in a cylinder of radius 2 cm and length 1m. The endpoints of the target were positioned at -101.3 cm and -1.3 cm in the OMEGA co-ordinate system. Figure 1 shows the layout of the apparatus, and the orientation of the OMEGA co-ordinate system (the origin of the system is on a line with, and just forward of, the hydrogen target). It also shows the position of the beam-counters (section 2.6.1).

2.3 The H1 Beamline

The beamline for the OMEGA area is the E1/H1/P1 beamline which is capable of supplying electrons and unseparated hadrons. Only the hadron beam was used during physics data taking runs, although the electron beam was used for calibration purposes.

The hadrons are produced from a beryllium target. Protons from the SPS, with a momentum of 450 GeV/c, are directed onto this target (T1) and the interaction products selected on polarity and momentum. Hadrons of up to 300 GeV in energy, and of either positive or negative polarity can be obtained in this fashion.

The composition of the beam depends on its polarity. For the conditions under which the experiment ran, the negative beam consisted almost entirely (96%) of pions, with a combined K^- and $\bar{p}$ contamination of 4%. The positive beam was split between protons

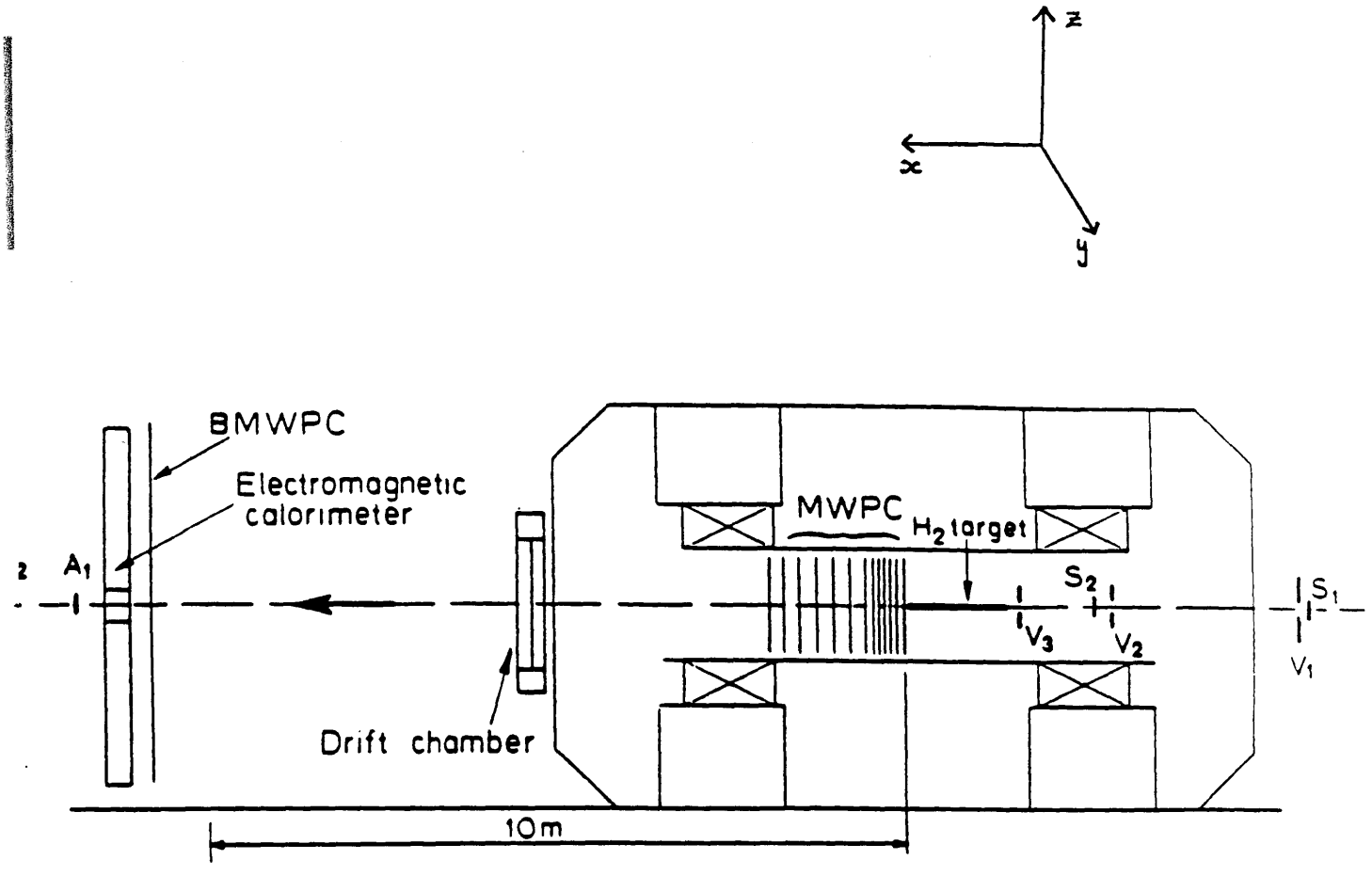

Figure 1: Layout of the WA70 Experiment

(77%) and pions (20%), with a small kaon component of 3%. The proportion of pions in the positive beam is normally lower, but during the experiment it was enhanced by the use of a 2.5 m long polythene filter.

Due to the mode of operation of the SPS, the beam arrives in bursts; each burst lasts 2 seconds, and a start-of-burst signal is available for use in the trigger electronics.

Two differential Cerenkov counters (CEDARS) [26], placed just upstream of the OMEGA magnet, were used to differentiate between the hadron types. The radiator medium in the CEDARS is helium under pressure. By adjusting the gas pressure and/or the optical system, the CEDARs can be tuned to maximum efficiency for either the proton or the pion component of the beam. For the experiment, both CEDARs were tuned for pions at 280 GeV/c.

Each CEDAR contains a ring of eight photomultiplier (PM) tubes to detect the Cerenkov radiation. The CEDAR electronics makes available all eight signals, and in addition provide three coincidence signals; coincidence signals A, B, and C are set when at least 6, 7, and 8 PM tubes respectively give a signal in coincidence.

2.4 The Calorimeter

The calorimeter [1] consists of twelve segments arranged in four quadrants around the beam axis. A quadrant consists of three segments arranged one behind the other; the first two segments are identical, while the third, although similar in design, has a poorer spatial resolution. (Because of the increasing width of the shower as it develops through the calorimeter, it is unnecessary to maintain the same spatial resolution in the back segments). All segments have an active volume of 205 cm by 205 cm by 10 cm.

The segments are sampling detectors – that is, layers of converting material are interleaved with detector layers, and the electromagnetic shower is sampled as it develops through the segment. The converting material is lead arranged in 10 sheets, each 0.4 cm thick.

The detector layers are constructed from teflon tubes filled with scintillator, and coupled to photomultipliers. In a single layer, the tubes are parallel to one another, and embedded in epoxy. Stainless steel strips within the layer provide mechanical strength. The ten detector layers are then arranged with the tubes running alternately in the Y and the Z directions, giving a matrix capable of resolving the Y,Z position of a shower. Figure 2 shows the layout of the calorimeter segments, with an exploded view displaying the the arrangement of the scintillator tubes and their coupling to the photomultipliers.
Figure 3 shows a more detailed cross section of a single segment.

The diameter of the individual teflon tubes is approximately 0.5 cm; however, the tubes are bunched in groups of either two or four before being coupled to light mixers, giving channels that are either 1.07 or 2.14 cm wide. In addition, for a particular Y or Z co-ordinate, the tubes from all five layers of scintillator are coupled to the same light mixer and hence to a single PM (Figure 2). The group of tubes leading to a single PM are referred to as a channel.

Segments one and two contain both wide and narrow channels; along either co-ordinate, the first 96 of the 144 channels are narrow channels – that is, for half the width of the segment. In segment three, all of the 96 channels are wide channels.

The active volume of each segment is supported in an aluminium frame and covered, on the back and front faces, with a steel skin , 0.2 cm thick. Aside from mechanical support for the detector volume, the frame serves two other purposes. The first is to house the light mixers and PMs, which are placed along the two edges of the segment farthest from the beam. Inserted into the two inner edges are guides for a set of optical fibres, which couple each scintillator channel to a laser. These are used by the laser calibration system (see below).

The segments are separated from each other by a 'source plate' and a thin bag of epoxy. The epoxy bags are designed to take up any irregularities on the segment faces (during construction liquid epoxy was poured into polythene bags, the segments clamped together and

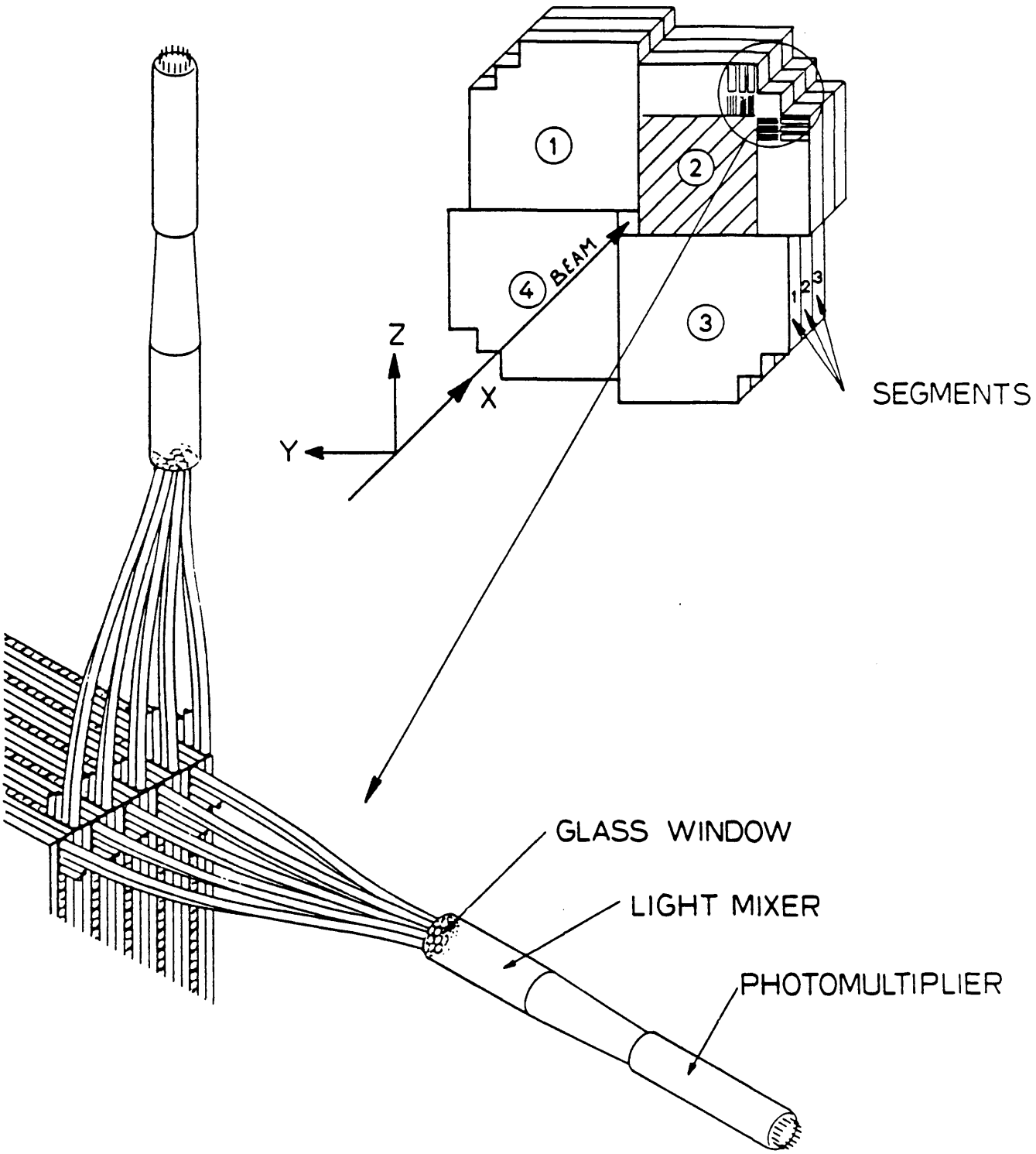

Figure 2: Construction of the WA70 Calorimeter

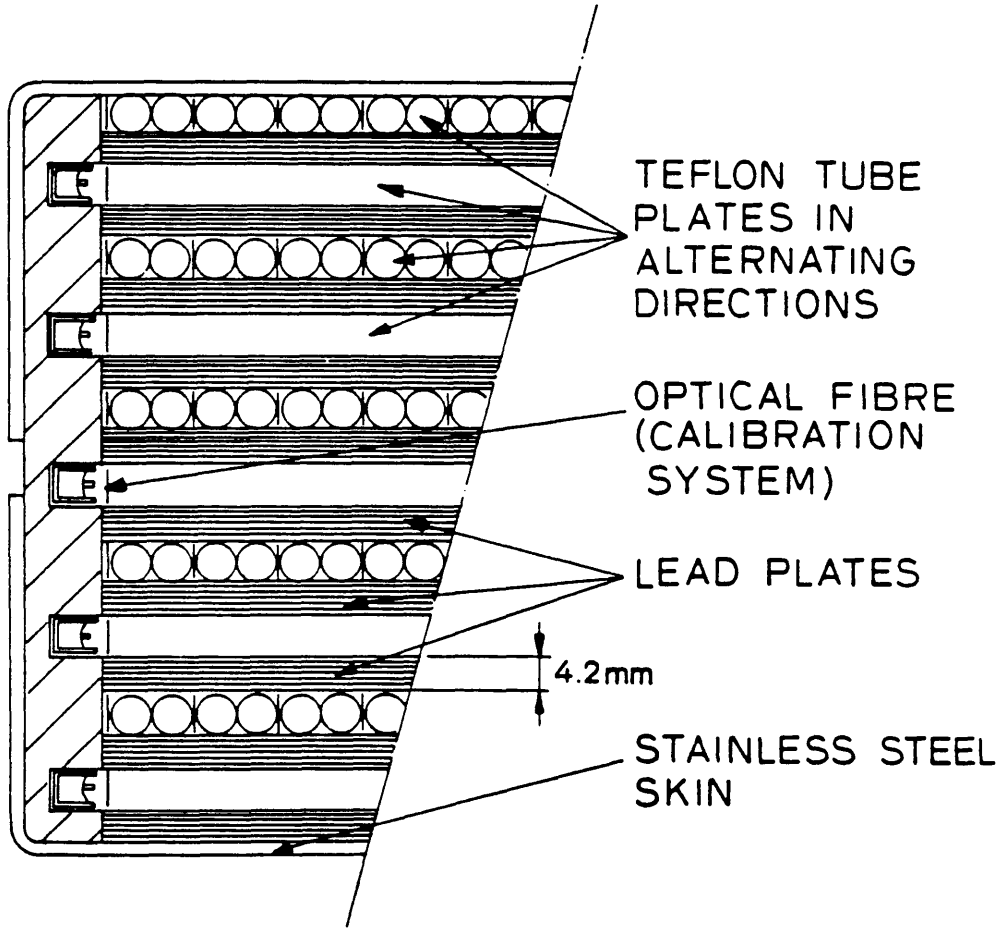

Figure 3: Cross Section of a Calorimeter Segment

the epoxy allowed to set). The source plates are part of the source calibration system (see below). Two compression modules on the back and front faces of the quadrant help prevent the surface of the outer segments bowing under the hydrostatic pressure of the scintillator. On completion, the quadrants were put under vacuum, and then filled with scintillator. This allowed any gas dissolved in the scintillator to escape during filling. A bellows assembly on the corner of each quadrant contains a reservoir of scintillator fluid. This is under a slight excess pressure, to ensure that scintillator escapes from any leaks in the calorimeter, rather than air being allowed in. It also compensates for thermal expansion in the system.

The calorimeter has two independent calibration systems built into it. One uses a laser to inject light directly into the detector channels, the other uses a set of radioactive (^{60}Co) sources. Both the source calibration system and the laser calibration system are described in more detail in chapter 3.

2.5 Electronics Associated with the Calorimeter

2.5.1 Photomultiplier Tubes, HT Supplies and ADCs

Before being mounted on the calorimeter, the photomultiplier tubes [27] were individually tested and calibrated. The calibration was to measure the gain, G, of each tube as a function of supply voltage, and was parametrised in the form

$$G = \beta K V^{\alpha}$$

where β, K, and α are the parameters of the tube, and V is the voltage applied. From the parametrisation, a value of V was calculated for each tube such that each one had the same gain, calculated to give the best 'working energy range' for the calorimeter. This was calculated from the analysis of test runs using an electron beam and a prototype calorimeter module.

Using the results of the parametrisation, the tubes were divided into two groups. The first group comprised those tubes whose gain was less sensitive to voltage, and the second, those that were more sensitive. The tubes in the first group were used closer to the beam hole than those in the second, since they would be less susceptible to the effects of high counting rates.

The parametrisation was also used by the laser equalisation system when adjusting the PM gains (chapter 3).

The HT supplies used were the LeCroy System 1440 programmable HT crates. Each of the 256 channels in a crate can be individually adjusted and monitored via CAMAC. Twelve crates were used, giving one HT channel per PM. An online monitoring program was set up to give warning should the supply voltages drift or fail.

The output signal from the PMs is read via LeCroy Analogue to Digital Converters (ADC's). These are 12 bit devices, allowing a signal resolution of 1 part in 4000; they are gated and read via the data acquisition system. The signal from each ADC channel comes from two sources – the output current from the PM, and the leakage current from the ADC electronics; the latter is known as the pedestal. The pedestal for each ADC channel must be measured when there is no PM signal, and later subtracted from any data recorded for that channel.

2.5.2 Time-of-Flight System

A Time-of-Flight (TOF) system [28] was incorporated into the calorimeter in order to aid the event reconstruction during the analysis, and to remove background events from the beam's muon halo. The system measures the time taken for a particle to cross from the interaction point in the target to the calorimeter, plus the time taken for the signal generated in the calorimeter to travel from the shower point to the relevant PM. The TOF uses information from segment 1 only, taking its signals directly from the next-to-last dynode on each PM. There is one TOF channel for each detector channel in segment 1. Figure 4 a) shows

a block diagram of the TOF system. The signal from the PM triggers the overlap unit for that channel, which then generates a constant current until halted by the stop signal. The constant current is integrated by the ADC module to give a digital signal proportional to the time for which the current was generated. Figure 4 b) shows the relative timing of the input signals.

The stop signal is taken from the S2 counter, which is part of the beam-trigger system (described below) and is common to all TOF channels. The signal is delayed so that the stop signal cannot reach the timers before any possible start signal. The length of the delay is precisely known and can be taken account of when calculating flight times.

The use of the S2 signal causes a problem since the time difference between the S2 signal being generated in the counter, and the actual event occurring in the target is variable. In principle, this 'jitter' in the S2 signal means that the flight times are only known to plus or minus the maximum error in S2; in practice it was found that the error for a particular event could often be corrected for during event reconstruction.

The TOF system was calibrated using laser pulses to simulate the shower signals.

2.6 The Event Trigger Logic

Events were only written to tape when several conditions were satisfied, the purpose of the conditions being to ensure that the event was one that we wished to study; this meant that time was not wasted recording unwanted data. The trigger conditions set can be broken down into those relating to the incident particles (the beam-trigger) and those relating to the information in the calorimeter (the calorimeter-trigger). If the beam-trigger decided that an event of some kind had occurred it sent a signal to the calorimeter-trigger [29], which then processed the calorimeter data to see whether or not the event could have been a high P_t interaction. If it could, then the trigger would send a signal to the data acquisition system, and the event would be written to tape. The criteria applied by the two triggers, and their implementation, are described below.

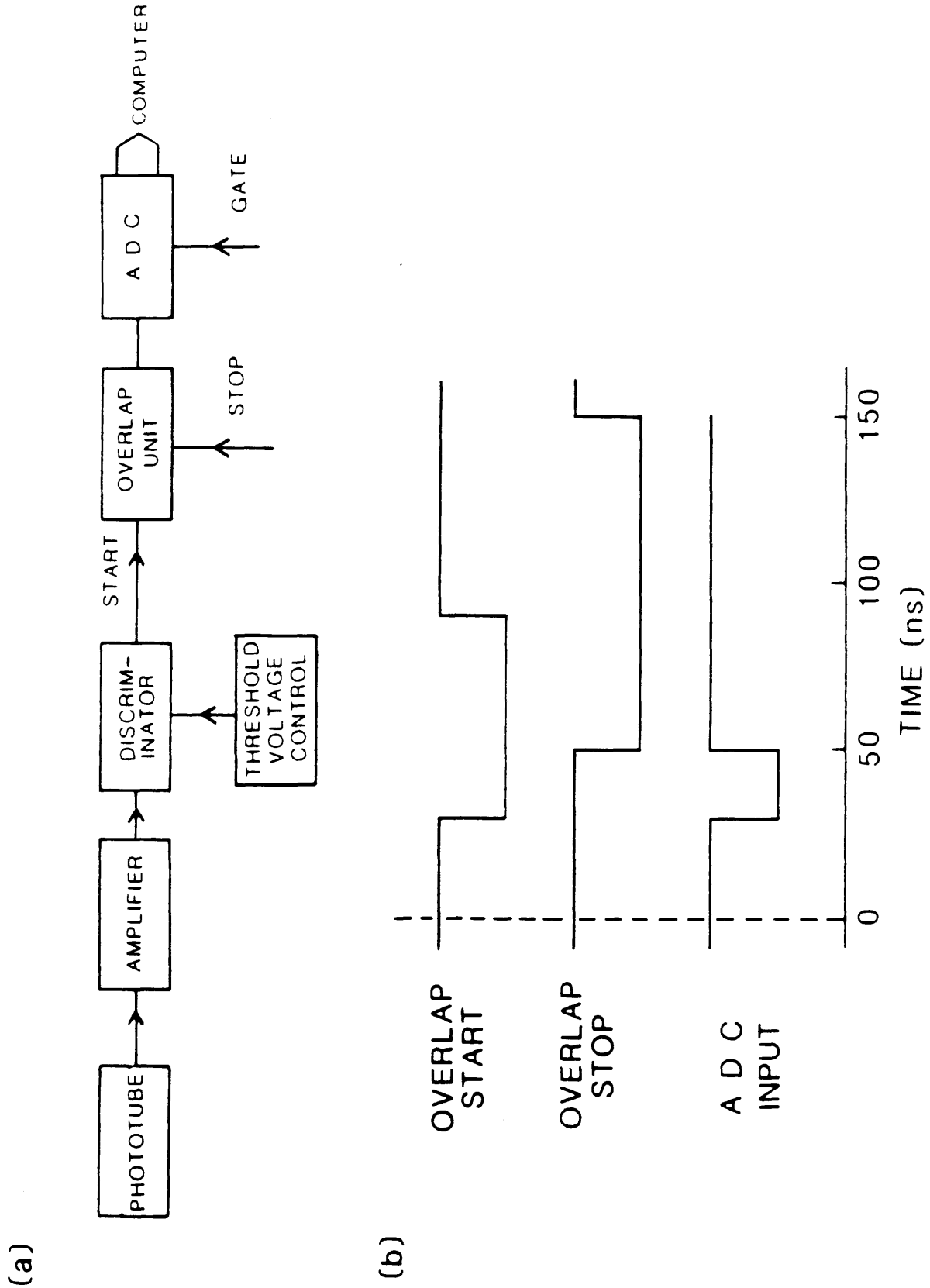

Figure 4: WA70 Time-of-Flight system: a) Block diagram, b) Timing of input signals

2.6.1 The Beam Trigger

The purpose of the beam-trigger was to detect particles which passed down the beam-line to cause an interaction in the target. A series of beam counters (solid plastic scintillator) were placed along the beam axis, both upstream and downstream of the target. The signals from these were passed to a logic circuit where a trigger/no-trigger decision was made. In addition, the logic circuit also provided signals for a set of scalers which were used to monitor and record quantities such as beam rate and interaction rate.

The positions of the beam counters are shown in figure 1. The S1 and S2 counters are disc shaped, while the V1, V2 and V3 counters are annuli. The logic circuit in figure 5 shows how the signals from these five detectors were combined to produce TOTB = $S1.\overline{V1}.S2$ and CB = $TOTB.\overline{(V2+V3)}$ the total beam and clean beam signals respectively. Only particles which passed through the S counters but missed the V counters caused TOTB and CB to be high.

The A1 and A2 counters were placed to detect beam particles passing through the target without interacting. Their signals were combined with CB to produce the interaction signal, INT = $CB.\overline{(A1+A2)}$.

The CEDAR counters have been described earlier in this chapter; only two of the four sets of signals available from each of these counters were used by the beam logic. The first of these, the six-fold coincidence signal, was fed to a pattern unit, which was later written to tape by the data acquisition system. Since the coincidence-signals were slow to arrive, the trigger also used the CEDAR PM signals directly. These were summed into a single analogue signal and fed to a threshold discriminator to produce the CED.A signal. If this signal was low, it implied that the particle was a proton, while if it was high, it implied a pion. The CED.A signal is logically combined with the INT signal to produce three further signals – INT.PI, INT.P, and TRIGGER (= INT.P + INT.PI). A high TRIGGER signal implied that an interaction had occurred, and was used to gate the calorimeter-trigger electronics. INT.P and INT.PI were stored in the pattern unit mentioned above.

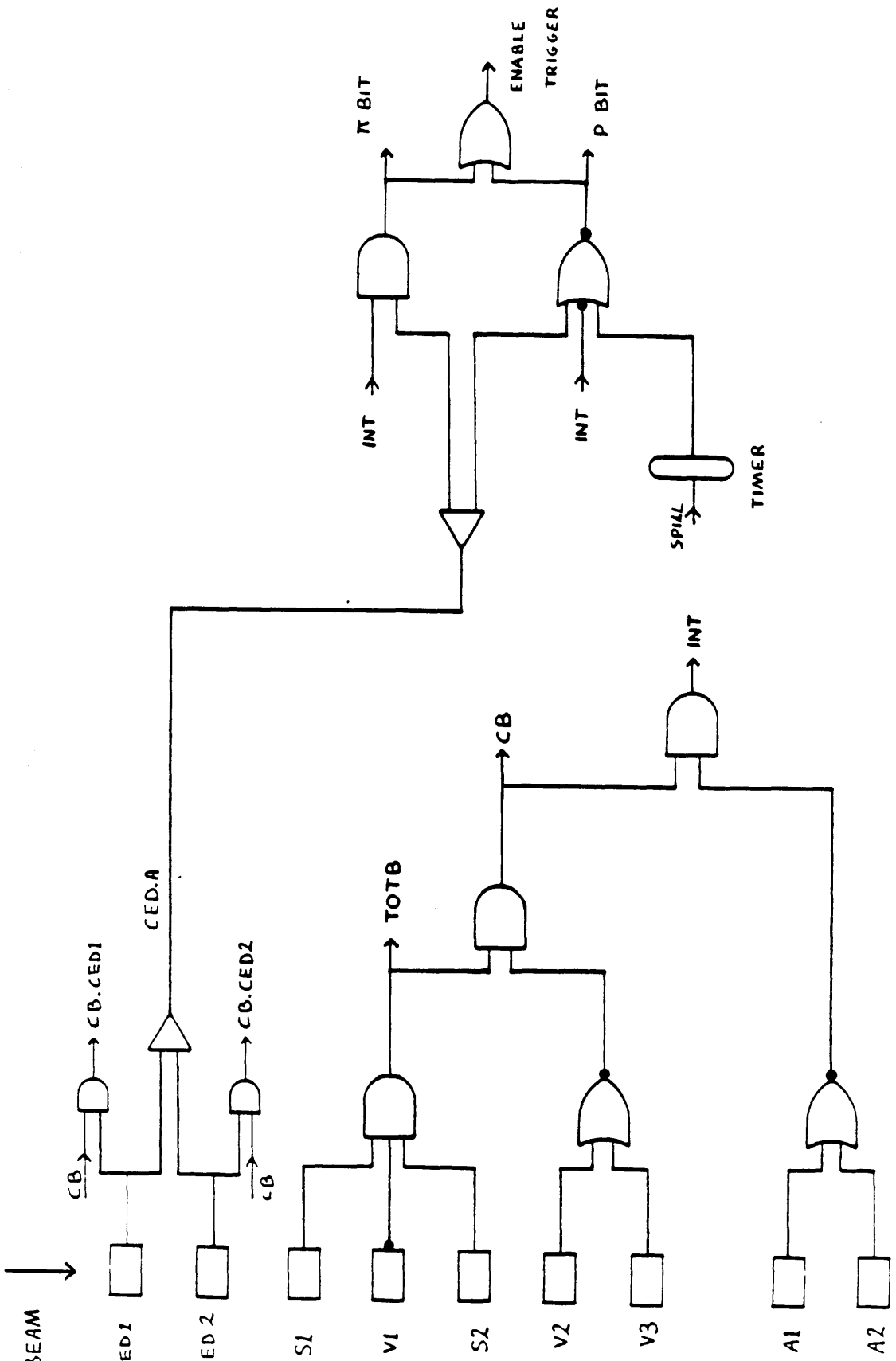

Figure 5: The logic circuit for beam counters

The 1 second timer shown in figure 5 was used to enhance the proportion of pion to proton events written to tape when taking data with a positive beam. The timer was gated by the start-of-burst signal, and while its output was high, both pion and proton events could cause a TRIGGER signal. After the timer had gone low (half way through the burst) the logic circuit would only allow pion events to cause a trigger.

2.6.2 The Calorimeter Trigger Requirements

The calorimeter-trigger was required to trigger on the occurrence of one or more of four types of event having:

i) a particle with $P_t > 3$ GeV/c

ii) a particle with $P_t > 4$ GeV/c

iii) a particle with $P_t > 1.8$ GeV/c

iv) two particles, each with a $P_t > 1.8$ GeV/c, hitting the calorimeter in different quadrants.

Any or all of these trigger conditions could be operating at any one time. Obviously, an event satisfying trigger condition ii) would also satisfy trigger condition i). However, flags for each successful trigger type were be set, allowing events of particular trigger types to be directed to a separate output stream if required.

Trigger condition iv) was designed to trigger on events that might contain a J/Ψ decaying to an e^+e^- pair.

Each quadrant had its own trigger; the output from the four quadrant-triggers are logically OR'ed to give the calorimeter-trigger signal.

2.6.3 The Implementation of the Calorimeter Trigger

There are three main problems in designing a trigger to look for high P_t particles in the calorimeter; these are due to the type of information available from the calorimeter.

The information provided by the calorimeter gives Y and Z co-ordinates separately – there is no direct method of knowing which Y signal matches with which Z signal, although the P_t for the whole event can be calculated. The trigger conditions, however, are to be imposed on single particles, so a fast method of event-reconstruction must be found.

In addition, a signal produced in a PM measuring the Y co-ordinate could have come from a particle incident anywhere along the 2 metre length of the scintillator tube. The signal attenuation over this length is a factor of 3, again making it impossible to calculate the transverse momentum without matching the Y and Z signals.

The final factor is that the signal at the PM is proportional to the momentum of the incident particle, P, and not to its transverse momentum, P_t This must be corrected for by calculating a value of $\sin\theta$ for each signal, where θ is the angle between the X axis of the experiment, and the particle's trajectory.

A solution to all of these problems is to divide the quadrant into strips running in the Y and Z directions. The cells formed by the intersection of the strips are then considered individually, with the assumption that all the Y signals from strip **i** and all the Y signals from strip **j** actually originate in trigger cell **ij** (figure 6). Although this assumption is not necessarily true, it will over-estimate the true value of the P_t and no events will be lost. Figure 6 also shows how the strip signals are fed to a matrix look-up table, which makes the trigger decision.

The cell structure in effect acts as a rudimentary event reconstruction. It allows a Z co-ordinate to be assigned to the Y signals (and vice versa) so that attenuation factors can be calculated, and so that the transverse momentum can be obtained from the actual momentum. The values used for attenuation length and for $\sin\theta$ are average values for each cell.

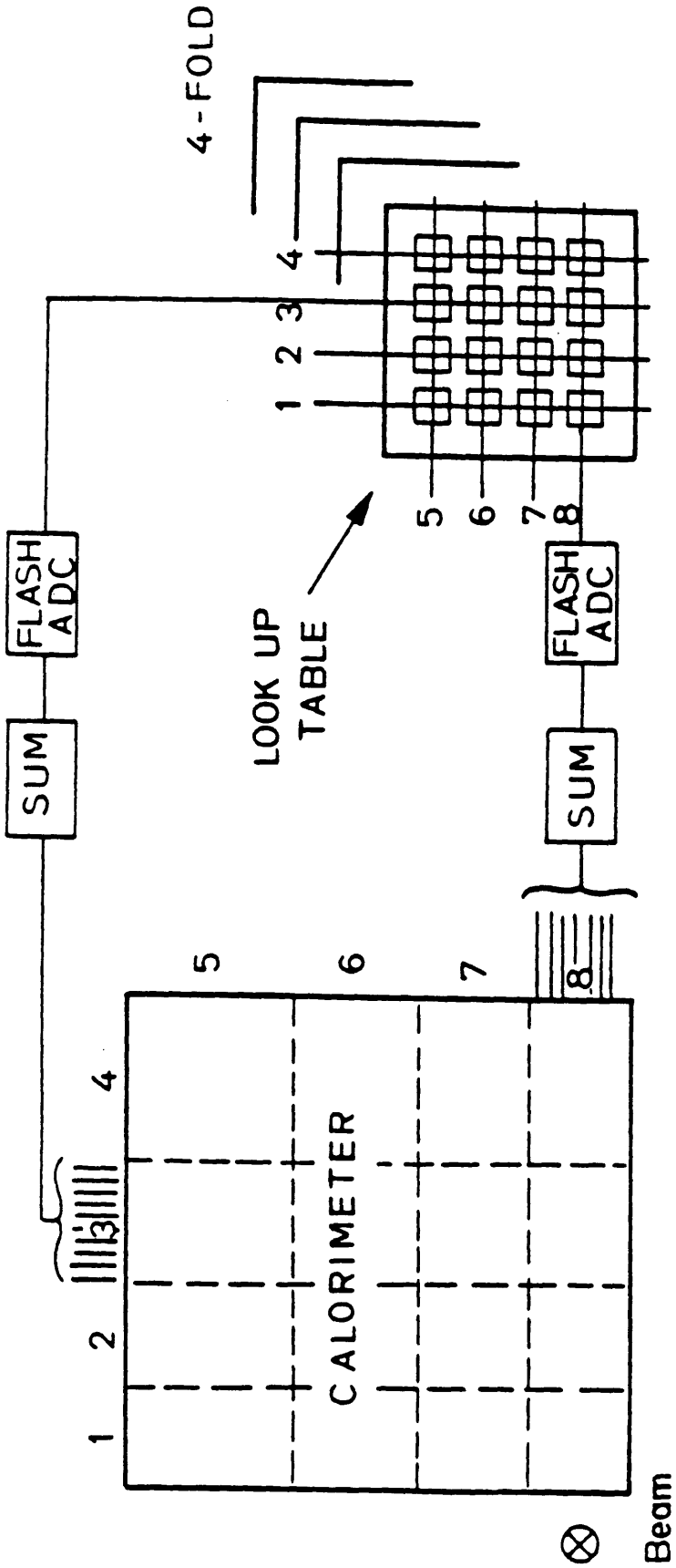

Figure 6: The trigger strips in the calorimeter

The trigger strips were made to overlap one another by one detector channel. This improves the trigger efficiency for those showers that fall on the boundaries of trigger strips.

2.6.4 Trigger Levels

While the trigger is processing information from the calorimeter, no more events can be taken; however, most triggers are rejected as being the wrong type of event. The trigger must therefore work fast, to reduce the trigger 'dead time', but must also make accurate enough calculations that no unwanted events are recorded. These conflicting requirements are resolved by applying the trigger conditions on three different levels. At each level, the calculation is slower, and more accurate, but is only applied to those events passing the previous stage. The sixteen trigger cells are considered simultaneously rather than sequentially, and their output signals logically OR'ed together to produce a trigger signal for the quadrant.

- *Level 1 Trigger:*

  The Y and Z signals are taken directly from the PMs, amplified, and added to produce the signals for each strip. The threshold conditions

  $$Pt_{y,i} > Pt_{threshold} \quad AND \quad Pt_{z,j} > Pt_{threshold}$$

  applied to each trigger cell i,j. (The notation $Pt_{a,b}$ refers to the 'b'th strip of co-ordinate 'a'). This calculation is fast, and is used simply to check that there are signals in the calorimeter.

- *Level 2 Trigger:*

  The strip-signals in Y and Z are digitised using fast ('flash') ADCs, and the output applied to look-up memory tables to decide whether or not the cell signals meet the following conditions:

  i) $$\sqrt{[Pt_{y,i}^2 + Pt_{z,j}^2]} > Pt_{min_1}$$

  ii) $$Pt_{y,i} > Pt_{min_2} \quad AND \quad Pt_{z,j} > Pt_{min_2}$$

iii) $|E_{y,i} - E_{z,j}| / |E_{y,i} + E_{z,j}| < \text{ASYMMETRY LIMIT}$

(Pt_{min_1}, Pt_{min_2} and ASYMMETRY LIMIT are constants for each trigger type.)

All three conditions must be satisfied, and in addition, for trigger type 4, there must be at least two quadrants satisfying the requirements. Condition iii) is a test on how well the energies in each co-ordinate match, and compensates to some extent for the compromise of using trigger strips.

The overall decision time for level 1 and level 2 triggering is 225 ns.

- *Level 3 Trigger:*

  The level three conditions are the same as those applied by the level 2 trigger; however they are made on smaller strips (2 or 4 cm wide) and use the output from the ADCs rather than directly from the PMs. The calculations are carried out by a microprocessor system (known as MICE) [30]. This third level calculation is much slower than the previous two (the decision time is about 10 ms), but since it is carried out on far fewer events, this can be tolerated.

  The MICE can be operated in either flagging mode or in rejection mode. In the former case, all events are passed, but a flag is set to indicate whether the event would have passed the trigger conditions. In rejection mode, events are only passed to the data acquisition system if they do meet the conditions.

  Since the level 3 trigger requires the calorimeter information, the result of the level 2 trigger is used to make the decision to read out the calorimeter and wire chamber information. The level 3 trigger then decides whether that information will be passed on to the data acquisition system.

All the calculations performed in levels 1 and 2 are made in hardware; the calculations for $\sin\theta$ and attenuation, for instance, are made by using resistors to 'weight' the signals from the calorimeter. The level 3 calculations are made in software.

3. SOURCE CALIBRATION SYSTEM

3.1 Introduction

The calorimeter used in the WA70 experiment has a large number (3072) of photomultiplier tubes, all of which must be set to the same gain. In section 2.5.1 the parametrisation of these tubes was described. However, the constants measured for each tube are not accurate enough to allow the tubes to be adjusted simply by setting the HT for each tube. Some form of feedback between the HT setting and the gain of the PM is required. This can be achieved by using either of the two calibration systems.

The primary purpose of the two calibration systems is to set the gain of each of the 3072 photomultiplier tubes to the same value (known as equalising the PMs). When using either system, the same basic algorithm is used; the steps are:

i) A standard 'quantity of energy' is deposited in the scintillator.

ii) The output signal from each PM is measured.

iii) The average output signal is calculated.

iv) A correction factor is calculated for each PM (The correction factor is the fractional change in the gain of the PM required to set it equal to the average gain).

v) The correction factors are related to changes in the supply voltage using the parametrisation described in section 2.5.1.

vi) The supply voltages are changed.

The process is then repeated until all PMs have the same gain.

In addition to equalising the PMs, the calibration systems can be used to monitor drift in the gains during the experiment. The measurements made can be used either to correct the PMs immediately, or for offline correction of the data during the analysis.

An alternative method of calibrating the PMs is to scan the quadrants with an electron beam of known energy. Such scans are very useful, but can be carried out only occasionally, because of the problems of setting up and scanning an electron beam, and because of the demands on beam time. For this reason, little data has been taken using this method.

In this chapter, the construction of the source system will be discussed in detail, together with a description of how it is controlled and driven, and how measurements are made. A brief description of the laser system will also be given. The next chapter will then discuss the data taken using the calibration systems.

3.2 The Source System

3.2.1 The Source Plate

When designing the source system, one of the requirements was that it should be possible to take measurements on each detector channel from two different positions along its length. In addition, these positions should be situated away from the edges of the calorimeter in order to avoid any possible 'edge effects'. This implied that the system had to be capable of positioning a radioactive source anywhere along four 'scan lines', each line parallel to, and inset from, a calorimeter edge. This was achieved by housing the source inside a 'source plate', with an enclosed channel cut into the plate to guide the source along the scan lines. The source plates are constructed from two sheets of polypropylene, each with a groove machined into one surface. When two sheets are laid together, the grooves form the source guide-channel (figure 7 a)). The plates are 9 mm thick. There are four sources per quadrant, with the three detector segments and four source plates interleaved. A drive system is mounted at the corner of each quadrant, so that the source system of each quadrant is independent of the other three.

The source is mounted on a continuous loop of plastic coated wire chain that runs inside the guide channel. An extension of the guide channel at one corner brings the chain out of the source plate to link up with the drive system. Figure 7 b) shows the path of the source around a source plate. The drive mechanism is shared between the four source plates in the quadrant

3.2.2 The Drive System

The source drive system is shown in detail in figure 8. It comprises one motor, one encoder, and four electrically driven clutches. The motor drives a single shaft on which the four clutches are mounted. Each clutch drives a source chain, via a gear wheel; for safety, the clutches are slipping (friction plate) clutches – no damage will be done to the drive system, or to the chain, if any of the sources jam. The encoder is mounted directly on the motor shaft, and measures the rotation of the motor rather than the position of the sources.

To ensure that the sources can never be driven over the drive-gears, a limit switch (microswitch) is positioned at either end of the source path (figure 8). If the source approaches the drive assembly, one of the limit switches trips, and turns off the relevant clutch. In addition, a mechanical stop is placed between the limit switch and the source drive, as a guard against failure of the microswitches.

A lead garage encloses the drive assembly and limit switches, and houses the sources when they are not in use. A radiation alarm system was installed beside all garages, as an additional safety measure.

3.2.3 Measurements along a Detector Channel

The two points on a detector channel where source measurements can be made are known as the level 1 and level 2 points; the level 1 point is the closer to the PMs, and is separated from the level 2 point by 138 cm.

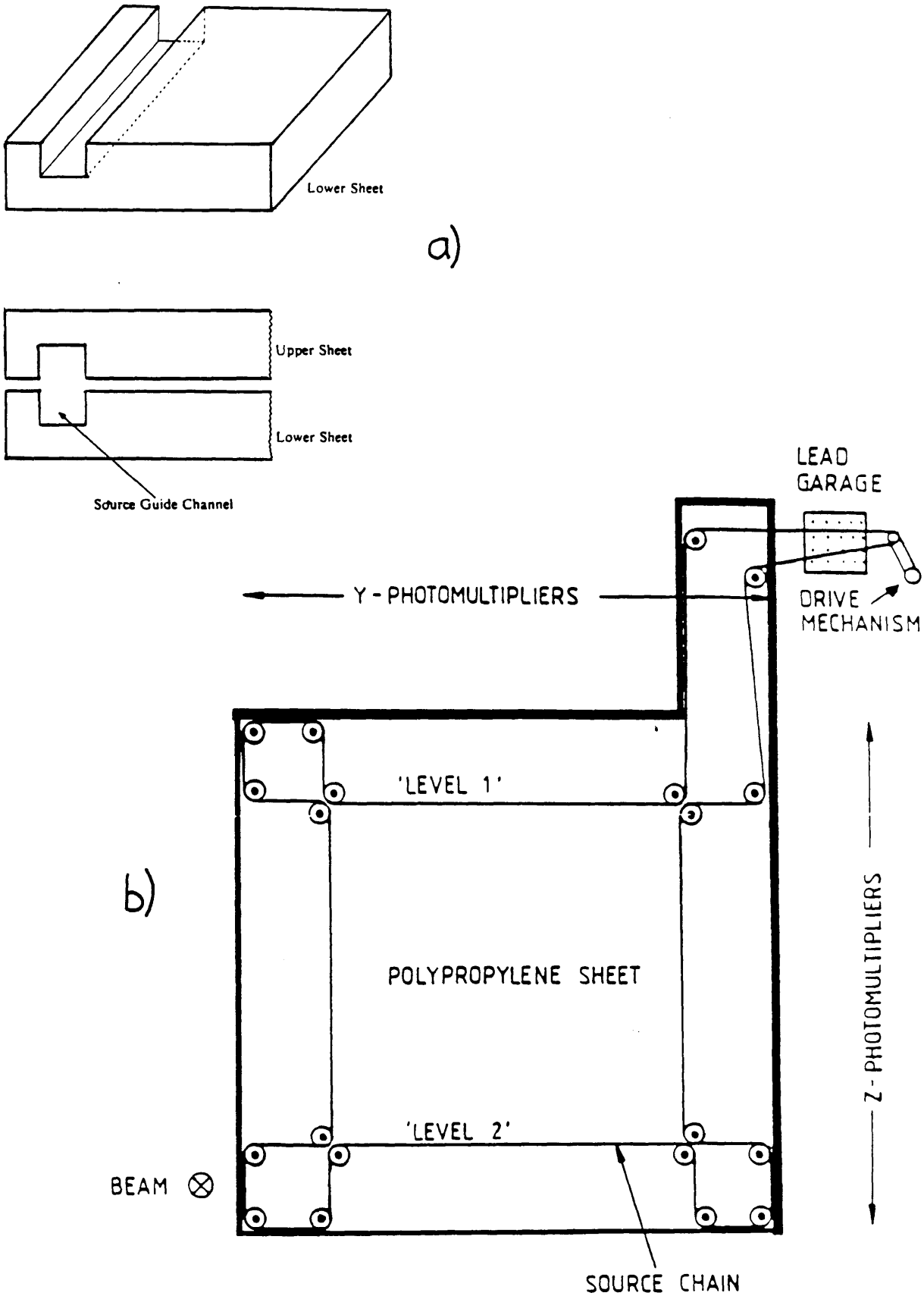

Figure 7: The source plate

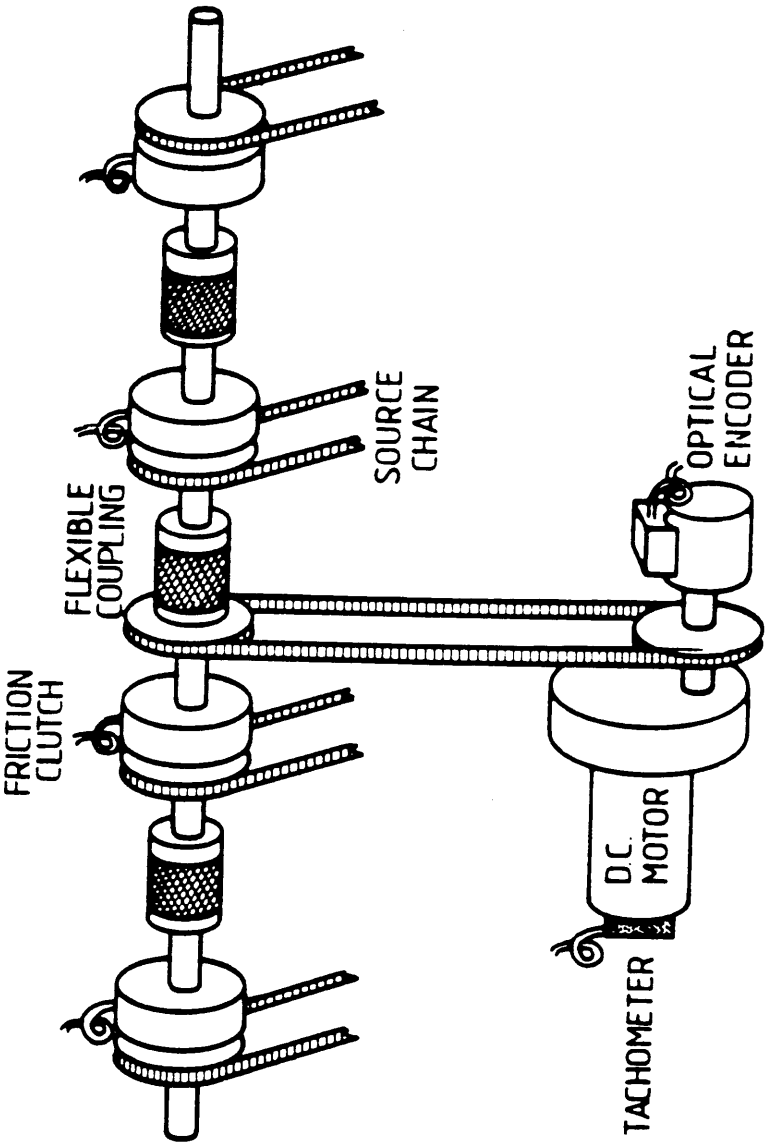

Figure 8: The source drive system

There are two reasons for requiring two points of measurement along each channel. One is simply that it allows data to be cross checked. The second is that it enables a measurement to be made of the light-transmission attenuation length of the scintillator. Whilst the attenuation length was measured in the laboratory before the segments were filled, it is nevertheless important to be able to check for any changes while the calorimeter is in use.

3.3 Controlling the System

The source drive system can be controlled either manually or from the computer. For data taking, it is necessary, for both speed and accuracy, to have computer control of the sources, while in general a manual system is required both for convenience and for safety.

3.3.1 Manual Control System

The manual system is straightforward, and (for each quadrant) consists of a motor control (reverse, off, forward) and four on/off switches for the clutches. A set of LEDs indicate whether the sources are at the limit switches, whether or not the clutches are engaged, and whether the motor is driving. The system was designed so that the sources could not be driven past their limit switches, and onto the drive gears, while at the same time they could be brought *back* off the limit switch in the 'safe' direction. Contacts were provided to enable an audio-visual alarm whenever the sources were out of the garage.

3.3.2 Computer Control System

The computer based system is shown in block form in figure 9.

The 'intelligence' of the system lies in the CAMAC module. Given an (angular) position for a particular motor to reach, the module drives the motor into position, and then monitors it to check that it remains there. The VAX computer itself plays no part in the process as such; it simply runs the control program, sending commands to the module or

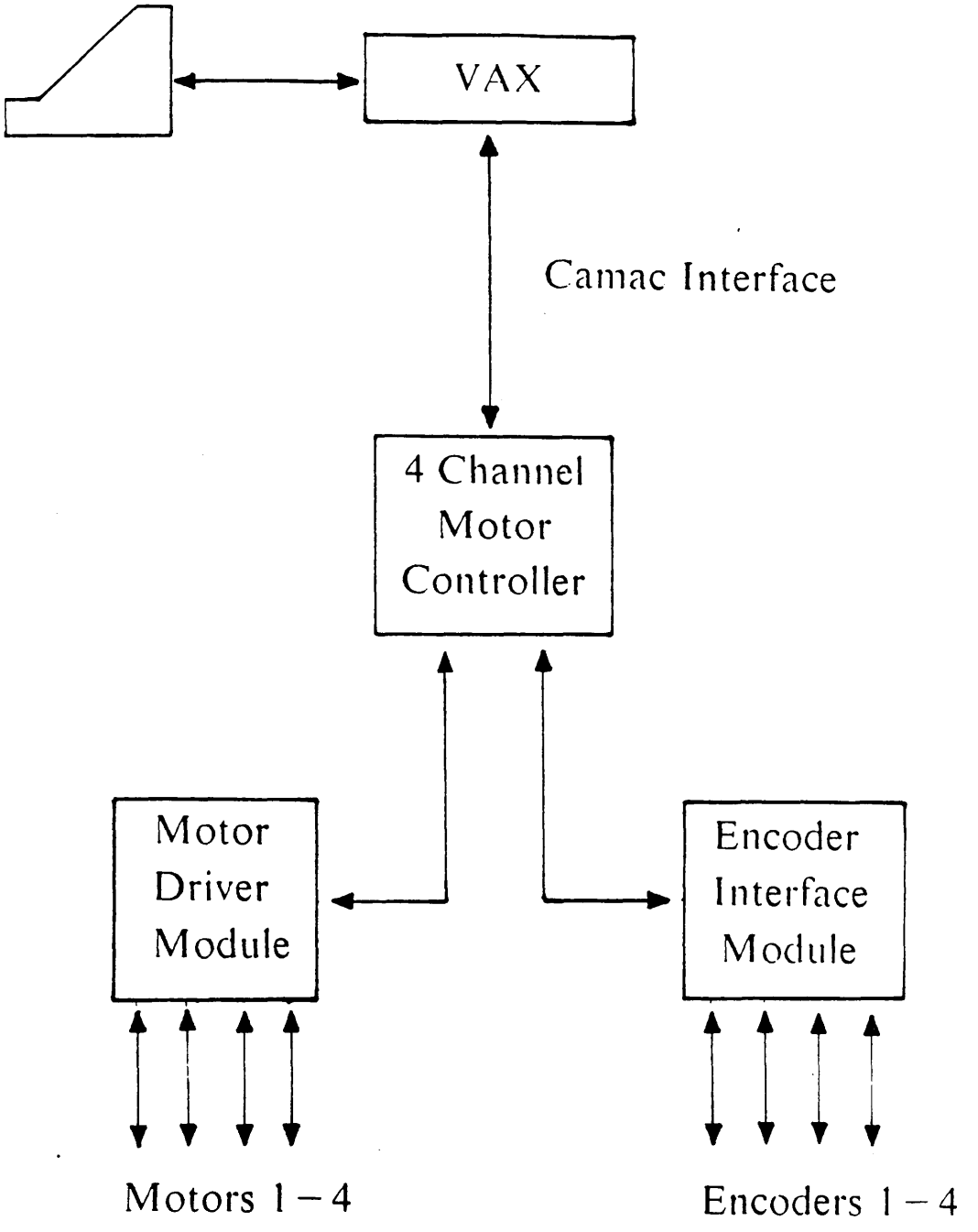

Figure 9: Block diagram of the computer-controlled source drive system

querying it for status information. The CAMAC module, together with the two NIM modules, form a complete motor-control system capable of driving four motors at once. They are standard modules, designed and built by SEN electronics.

3.3.3 Accuracy

In principle, both control systems allow the source to be positioned at a given point to within a millimetre – the accuracy of the motor/encoder combination. In practice, because the clutches can slip, and because the encoder monitors the motor rather than the clutches, a source cannot be simply driven for a pre-calculated distance, but must be monitored (via the signals from the PMs) and its position corrected by a feedback loop.

3.4 The Signal from the Source

To understand the source-signal from a single detector channel, a set of measurements were made of channel output as a function of source position. It was found that the signal is fairly constant over most of the width of the channel, irrespective of whether it is a wide or a narrow channel. As the source moves past its edge, however, the signal from the tube drops quickly (figure 10).

The fall-off is a combination of two factors; the first is due to the inverse square law – as the source moves away from the channel, the amount of radiation received decreases. The second effect arises from the absorption of the gammas in the lead. The gammas from ^{60}Co have an energy of either 1.1 or 1.3 MeV (depending on the decay chain) with an attenuation length in lead of about 1.25 cm. The lead sheets are 0.4 cm thick, but the distance travelled (obliquely) by the gammas increases as the source moves away from the channel, increasing the absorption.

This simple view of the output signal-shape has to be modified when the internal construction of the segments is considered. As described in chapter 2, the segments are made

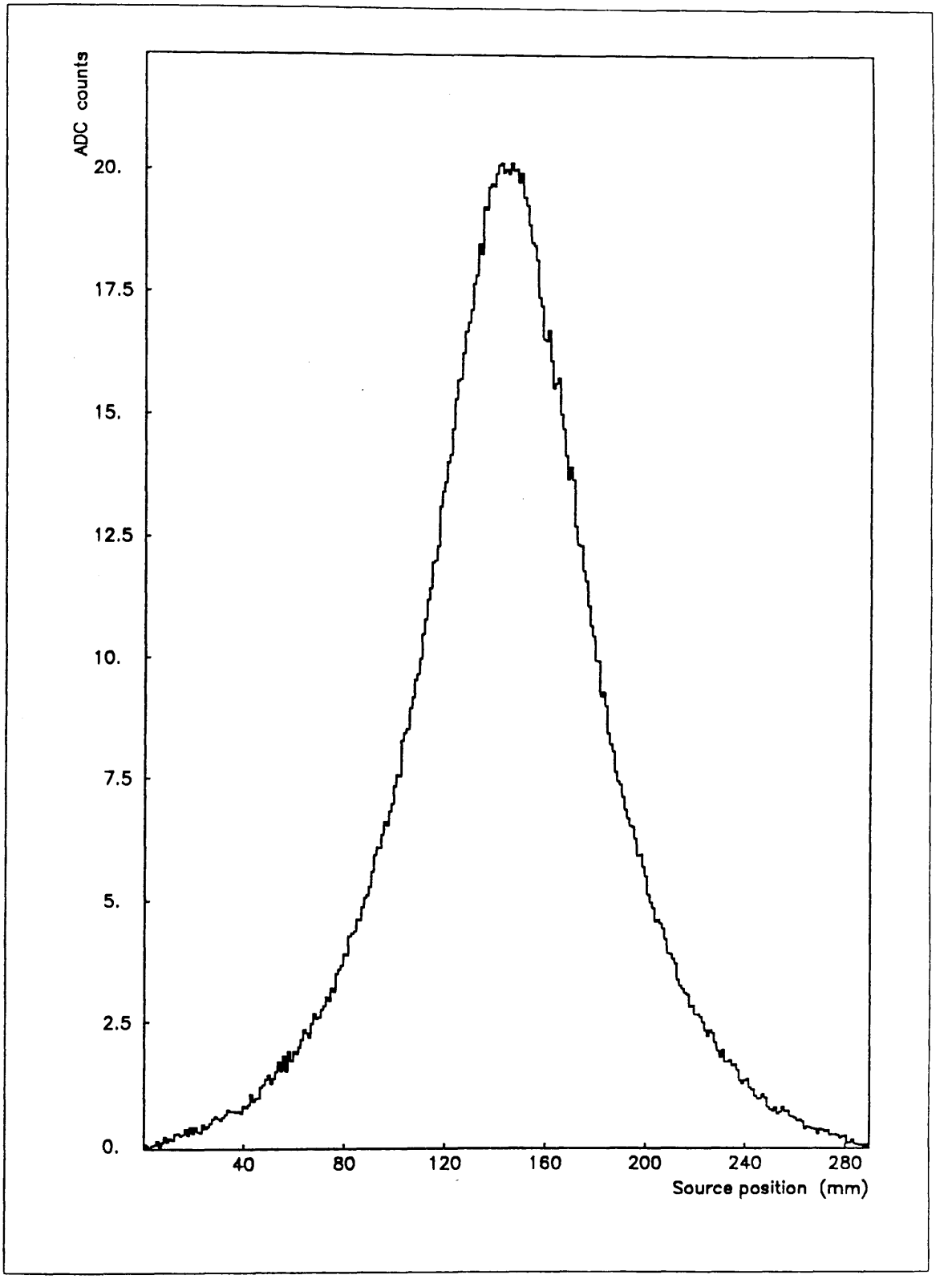

Figure 10: A profile of PM output versus source position

from sandwiches of scintillator and lead, alternate layers of scintillator measuring the Y or the Z co-ordinate. Thus a source on the front face of the segment will see a single layer of lead 'shielding' the first set of Y channels, but will see two layers of lead *and* a layer of scintillator shielding the first set of Z channels. In addition the angle subtended at the source will be smaller for the Z channels than for the Y channels, since the Z channels are on average further back from the source. When the back source is considered as well, there are four possible configurations, differing by the rate at which the signal changes with position, and by the maximum signal size.

Comparing maximum signal sizes, it was found that the ratio

Y (Back) : Z (Back) : Z (Front) : Y (Front)

is approximately

4 : 2 : 2 : 1

It was also found that the larger the maximum signal, the faster the signal decreased as the source moved away from the channel.

The final factor affecting the source signal is the position of the source – whether it is at the level 1 point or the level 2 point. The attenuation length of the scintillator causes a drop in light intensity of a factor of 3 over the 2 metre length of the tube, and a factor of 2 over the distance between the two levels (138 cm).

The absolute output due to the source may be between 5 and 80 ADC counts over a 10 μs 'gate' period (depending on the geometry of the channel being measured). This must be compared with a typical signal of 1000 ADC counts with a gate of 110 ns when the experiment is running and taking physics data.

In addition, because of the low strength of the ^{60}Co sources, the RMS on a single measurement is high – typically 20%. This is too high to be useful, so the source readings finally recorded were an average from 1000 measurements. The error on the average is then reduced by a factor of 32, giving an RMS of typically 0.7 %.

3.5 Source Scanning

Two methods of source scanning were considered during the development of the source system. The first possibility was to run the source continuously around the calorimeter, from one end-stop to the other, using the standard data acquisition system (DAQ) to record the output from the PMs. The alternative was to step the source from one channel to the next, pausing to record the signal from the current channel.

The first method had the advantage of simplicity. However, it was found to have two major drawbacks. The DAQ system used an input buffer which, at irregular intervals, was read and emptied. During this time no further data could be taken. Consequently different numbers of readings were taken from different tubes, making it impossible to calculate a time-average signal for each channel. The second problem was to the fact that the output due to the source is low. Statistical fluctuations were found to contribute an unacceptably large factor to the error on the measurements, and this method had to be abandoned.

The accuracy of the second method is limited only by two factors – the length of time for which the source is left on a given channel, and the accuracy to which it can be positioned on that channel. The price paid for this is the necessity for a complicated control program, and a slow rate of scanning. However, this was the method finally adopted.

3.5.1 Centring the Source

The position of the source at any one time can, in principle, be determined from the encoder on the motor. The accuracy of the encoder is a fraction of a millimetre; taking into account the accuracy of the CAMAC controlling module, the overall accuracy of the system is about 0.25 mm. However, as pointed out in section 3, the encoder is driven directly by the motor, and cannot take account of any slippage in the clutches. Some criteria were needed both to judge the accuracy of the source positioning, and to centre the source on a channel should the source position drift out of tolerance. Since the output signal is fairly insensitive to the source position when the source is directly over the channel, a tolerance of two or three millimetres was found to be acceptable.

Initially, the source position was tested, not by the output of the current channel, but by the relative outputs of the two adjacent channels. Once a source has moved past a given channel, the output decreases quickly and so is sensitive to small changes in position. Since the outputs of the two adjacent channels should be the same when the source is accurately centred on the current channel, their fractional difference provides a sensitive test on the position of the source.

This method was tested and found to have two main drawbacks. The first is that the adjacent channels do NOT have similar outputs (the whole purpose of the exercise being to measure these differences) and in fact the differences were found to be large enough that the method outlined above could not be used to centre a source within the tolerance required. The second problem was a mechanical one. When the centring the source by minimising the difference between the adjacent tubes, an iterative procedure was used, moving the source backwards and forwards by increasingly smaller amounts until it was in position. Backlash in the drive system made this process difficult to control properly.

Because of these problems, this method of centring was only used for one set of source scans; however, it did provide enough data on the system to develop a better centring technique.

3.5.2 An Improved Centring Technique

The shape of the source-signal (as a function of position), discussed in section 4, is dependent only on the 'geometry' of the channel being measured (ie whether it is a Y or a Z channel, narrow or wide, and whether it is being measured with a back or a front source). It follows that if two measurements are made on a given channel, one with the source centred *on* the channel and one with the source centred on an *adjacent* channel, they will have the ratio R :–

$$R = S_1/S_2 = S_3/S_2$$

where S_1, S_2, S_3 are the signals from channel 2 when the source is centred exactly over channel 1, 2, or 3 respectively (figure 11).

R is a function only of the geometry, and is independent of the gain of the channel concerned. Using data taken with the original centring technique, the value of R was calculated for the eight different geometries. The data on each channel consisted of a measurement of the current channel together with a measurement on the two adjacent channels. Although the source was not always centred accurately, enough measurements had been taken to ensure that any variations averaged out to zero.

The ratio R can now be used to centre the source on tube 3 by the following method:

i) The source is positioned over channel 1 (the exact starting position is not important).

ii) The source is then stepped, in small increments, past channel 2. The signal from this channel will grow to a maximum, recorded as S_m. (Since the stepping increments are small, compared to the width of the plateau, at least one measurement will be made on the plateau, where the signal is maximum).

iii) When the signal drops to a value S_c so that $S_c/S_m = R$ (within the tolerance) the source is halted.

iv) The maximum value, S_m , is now recorded as the source reading for channel 2. In addition, because the source was stopped when the signal had dropped by the factor 'R', the source is now accurately centred on channel 3.

This method has the advantage that since the source is only moved forwards, the mechanical slack in the system has no effect on the accuracy.

During source scanning, a 'running' value of R (R') is calculated by comparing the previous measurement on a channel with the current one. If the value drifts outside tolerance, the scan is halted, and the source re-centred. In addition, small corrections are made to

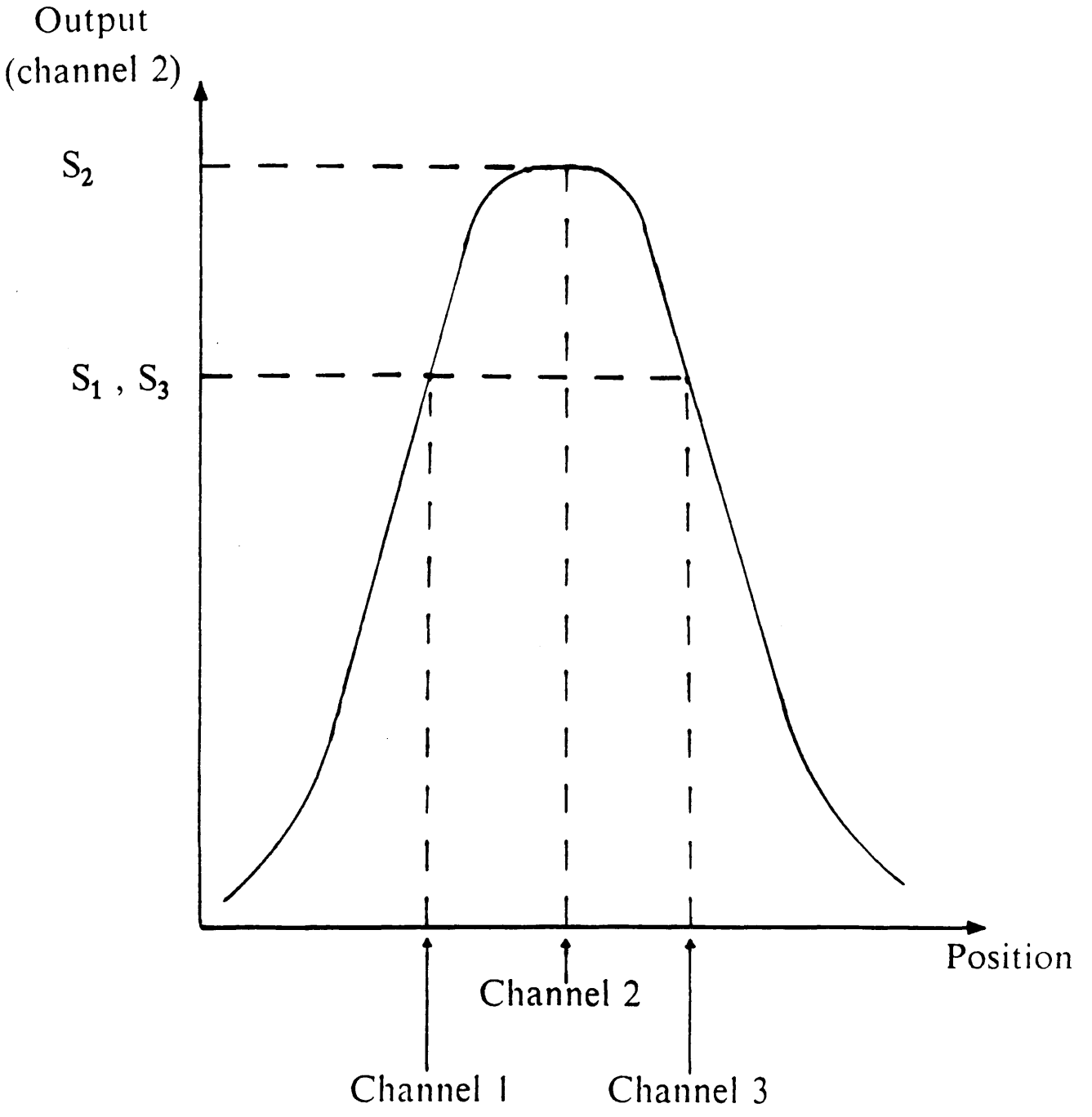

Figure 11: Signals from a channel, with the source in different positions

the source position each time it is moved. The corrections are based on the deviations of R′ from its expected value, R, and were found to be sufficient, in general, to keep the source within tolerance.

3.6 The Laser System

The laser system generates signals in the PMs by injecting light into the bottom of each detector channel. The light originates in a pulsed nitrogen laser, and is guided to the calorimeter via light fibres. In the light path are a set of filters, to control the light intensity, and a converter cell (filled with a stilbene/methanol solution) to change the wavelength to match that produced by the scintillator in the calorimeter. A light mixer ensures that the light is spatially homogeneous. A small fraction of the light is diverted at two points, to provide a trigger for the calorimeter in one case, and to a pair of reference PMs in the second. The reference PMs allow measurements on the pulse to pulse variations of the laser output. Figure 12 shows the way in which a single channel is illuminated. Each channel is coupled to five light fibres, one for each plane of teflon tubes. The set of fibres supplying a single plane is known as a barrette, and each is independent of the others. This is partly to provide redundancy in the system. More importantly, it is used to overcome the problems caused by the variations in light signal found when comparing fibres. The variations are due to two main factors:

i) The transmission characteristics of individual fibres may vary significantly from the average – the RMS is 15%. (In practice this RMS was reduced by making the barrette fibre bundles from fibres which differ from one another by only 5%.)

ii) The coupling of individual fibres to the laser can vary from fibre to fibre.

Using five light fibres per detector channel reduces the effect of these variations. However, there are channels where one or more of the light fibres has failed. For this reason, the laser

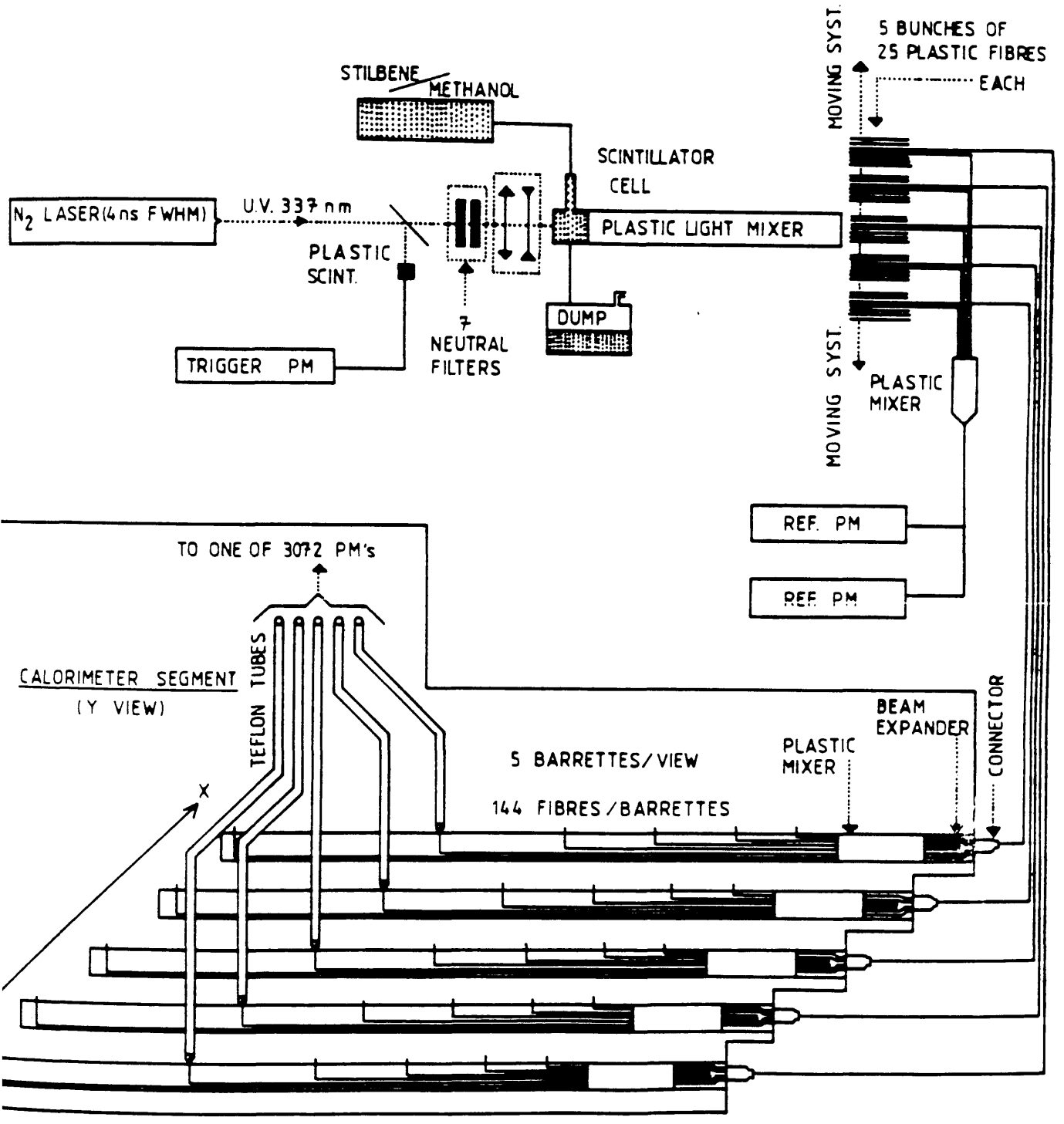

Figure 12: The Laser Calibration System

system can not be used as a stand alone system. Some method is needed to 'calibrate' the light fibres.

Carrying out a laser 'scan' of the calorimeter is very simple, since all channels are illuminated simultaneously, and may therefore be measured simultaneously. Laser scans are therefore very much faster than source scans. In addition, the laser signal is large, and produces ADC readings of around 1000 counts per 100 ns gate (cf. 1000 per 110 ns during data taking, and 40 per 10 μs from the source).

3.7 Conclusions

The laser and source systems are, to an extent, complementary. The laser system is fast (a complete scan can be done in just a few minutes) and produces a signal from the PMs that is comparable with that from the physics data. However, because of the variations in individual light fibres, the laser system itself needs some form of initial calibration.

The source system, on the other hand, uses a single radioactive source to calibrate a complete segment, positioning it over the channel to be measured; the same amount of energy can therefore be deposited in each detector channel. However, a source scan is slow, and the output signal from the PMs is small compared with that due to the laser.

In the next chapter, it will be shown how the two systems can be used in conjunction to form a calibration system capable of equalising the PMs before data taking, and carrying out fast monitoring scans while the experiment is in progress.

4. RESULTS OF THE SOURCE CALIBRATION

4.1 Introduction

In this chapter, the data obtained from the source system will be presented and discussed. This includes both the way in which the source data was used in the experiment, and the tests that were made on the data and on the source system to ensure that the results obtained were valid. This involved comparisons of the source data with data from the laser calibration system, with data from source scans made under varying conditions, and with data from electron-beam scans.

The way in which the source data was obtained will be discussed in detail. However, since the work with the laser system was not carried out by the author, the methods by which results were obtained from this system will not be presented.

4.2 The Source Data

A full source scan of the calorimeter produces a large quantity of data – 4 measurements on each of 3072 channels. Figure 13 shows plots of the data from the Y PMs of segment 2, quadrant 3. The data was taken just prior to the physics run in April 1984, and the PM gains had previously been equalised using the laser system. The plots are of level 1 (back), level 1 (front), level 2 (back), and level 2 (front), shown in Figures 13 a), b), c), and d) respectively.

The data from a complete source scan shows a number of features, all of which appear to some degree in the data shown in figure 13.

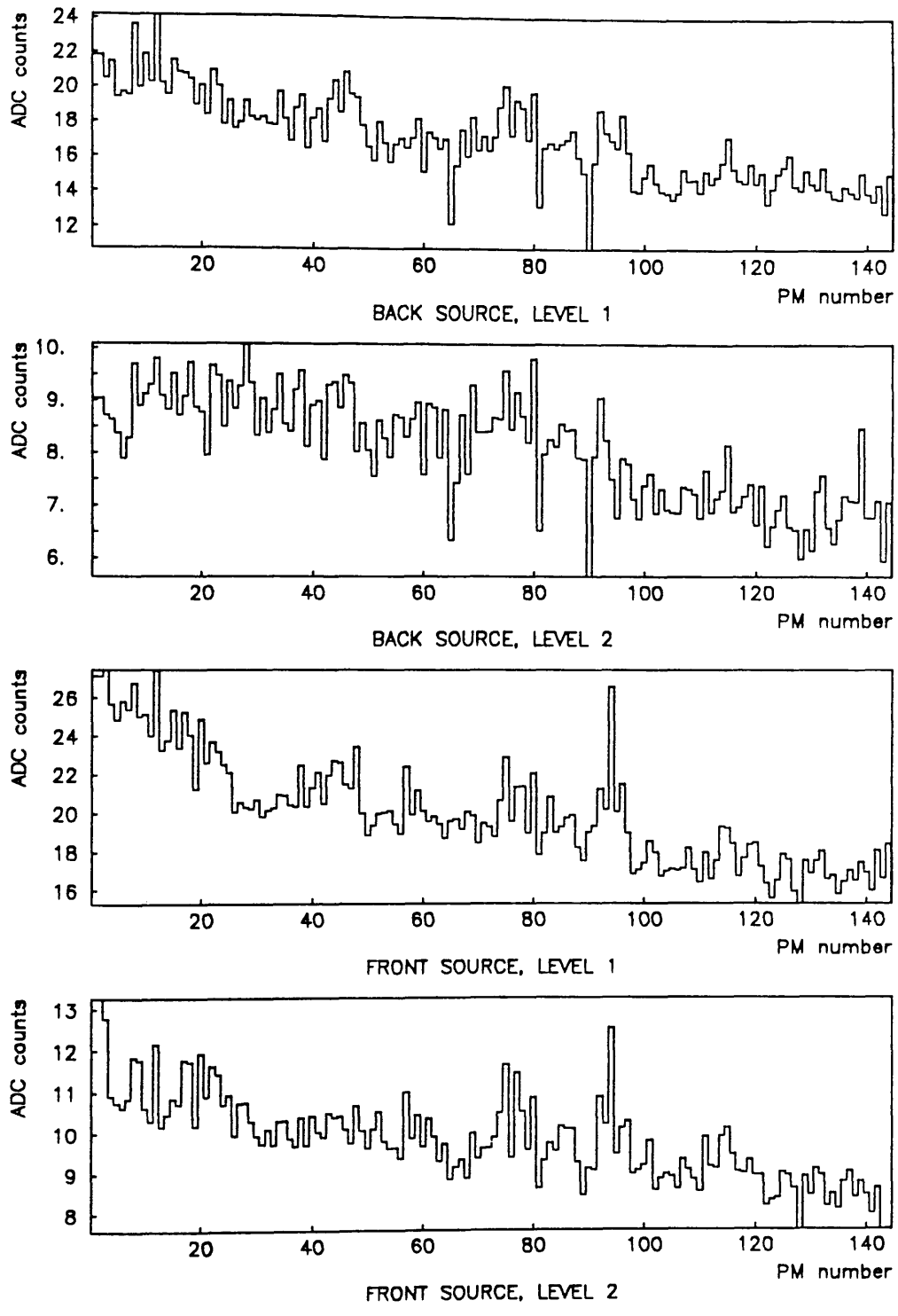

Note that the signals from PMs 97 to 144 have been scaled down by a factor of 2

Figure 13: Plots of data from a source scan

- There is a general decrease (a slope) in the source signal with increasing PM number (increasing distance from the beam hole). The average slope over the calorimeter is about 15%; varying from 0% to 25%, with uncertainties of $\pm$ 5% on individual slopes. The slope is defined as the difference between the signals at each end of the segment divided by their average. This is a naive definition since the degree of slope can vary considerably across the calorimeter. However, it is almost meaningless to try and fit a smooth curve to the data since in addition to the slopes, there are large fluctuations in individual readings (see below); the definition of slope given above is a simple and useful way of categorising the general decrease in the signal across the segment.

- There are large (5 or 10 percent) fluctuations in the signal from tube to tube.

- There are sections of the calorimeter (10 to 20 tubes wide) where the signal is consistently above or below the average for that segment.

- There is a step in the signal size at the junction between the wide and the narrow detector channels. A step-factor of roughly 2 is expected simply from the fact that the wide channels receive about twice as much energy from the source as do narrow channels. The step-factor was measured, and the value obtained was used to correct the data shown in figure 13. However, there is still a residual difference in the average signal from wide and narrow channels.

These features are common to the data from all quadrants and segments and from all source scans made after the laser equalisation of the calorimeter. (This does not necessarily imply that the effects are due to the laser).

4.3 Tests of the Source System

A variety of checks have been made on the source data to check the results of different scans for consistency – that is, to test that the results do not vary with time, and to eliminate as far as is feasible the possibility that any 'features' of the data are due to the source system itself.

4.3.1 Time Stability of the Source System

Figures 14 a) and b) show two scans of the centre section of one segment; the scans were taken one hour apart. Figure 14 c) shows the ratio of these two plots. The RMS of the ratio is 0.91%, implying an RMS contribution from each data set of 0.64%. In the previous chapter, it was calculated that the expected statistical error on a signal of 60 counts would be 0.7%. (It should be noted that the RMS on the raw source data is a measure of the fluctuation of the individual gains about the average gain (or alternatively, a measure of the 'poorness' of the source system), while the RMS on the ratios is a measure of the deviation of a given reading on a tube from the 'correct' reading from that tube). Thus, the two scans are identical to within the statistical errors of the source system.

Figures 15 a), b) and c) show the equivalent plots for two scans of the same section, separated in time by 40 days. The RMS in this case is higher, at 1.7%. There are two contributions to the value of the RMS here, one due to the statistical errors in the source measurements, and one due to the drift in the gains of the PMs over the 40 day period. This drift has been measured using the laser system and is less than 2%. It can be seen, then, that successive source scans are consistent over a period of several weeks.

These two tests were carried out on the centre section of quadrant 2, segment 1-Y, PMs 65 to 125 – that is, both wide and narrow channels were included in the scan. The source was used was the back source for this segment. This section was used for several of the source tests, and will be referred to as 'the standard section' when discussing measurements made on it.

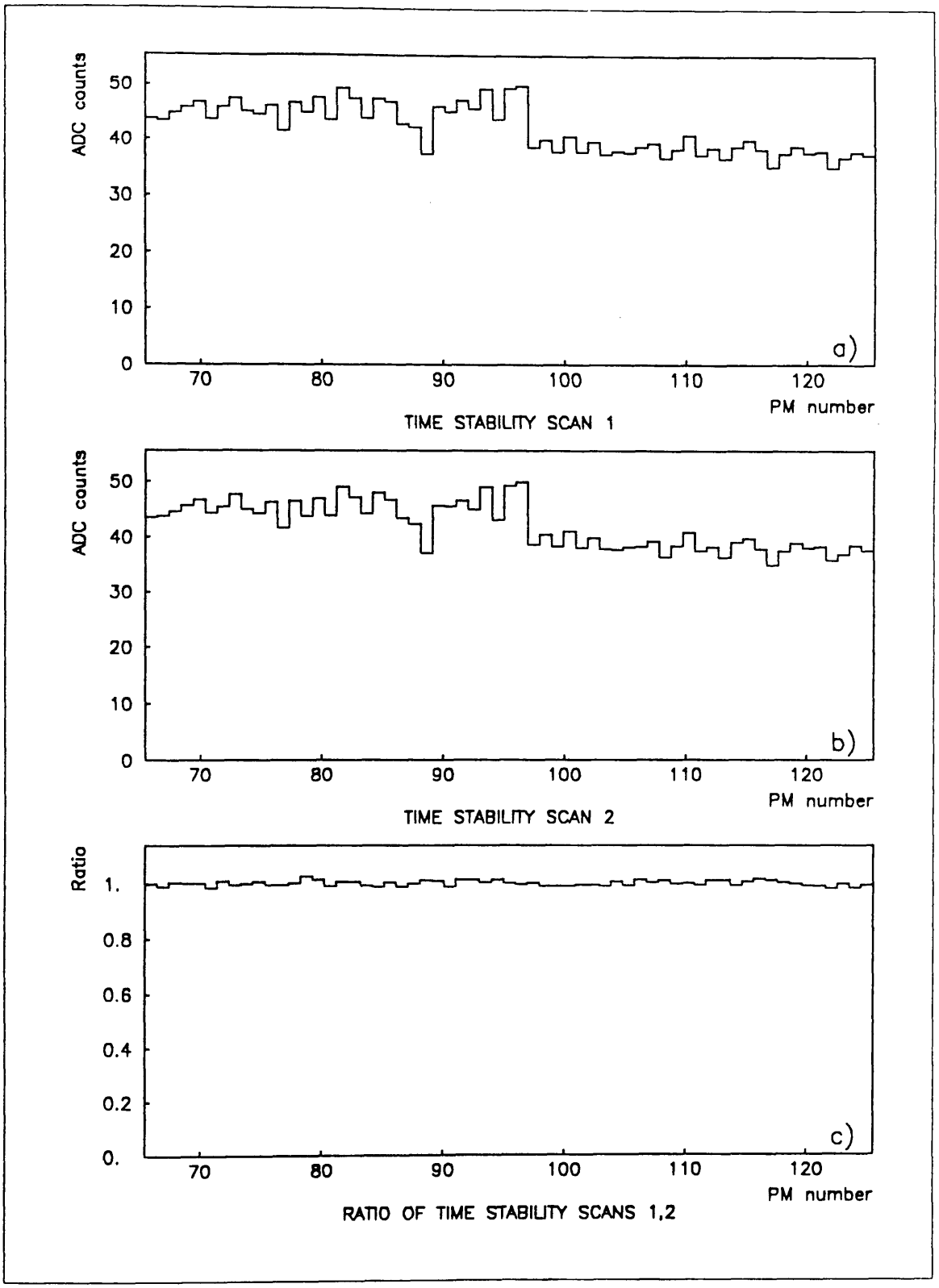

Figure 14: Successive source scans, separated by one hour

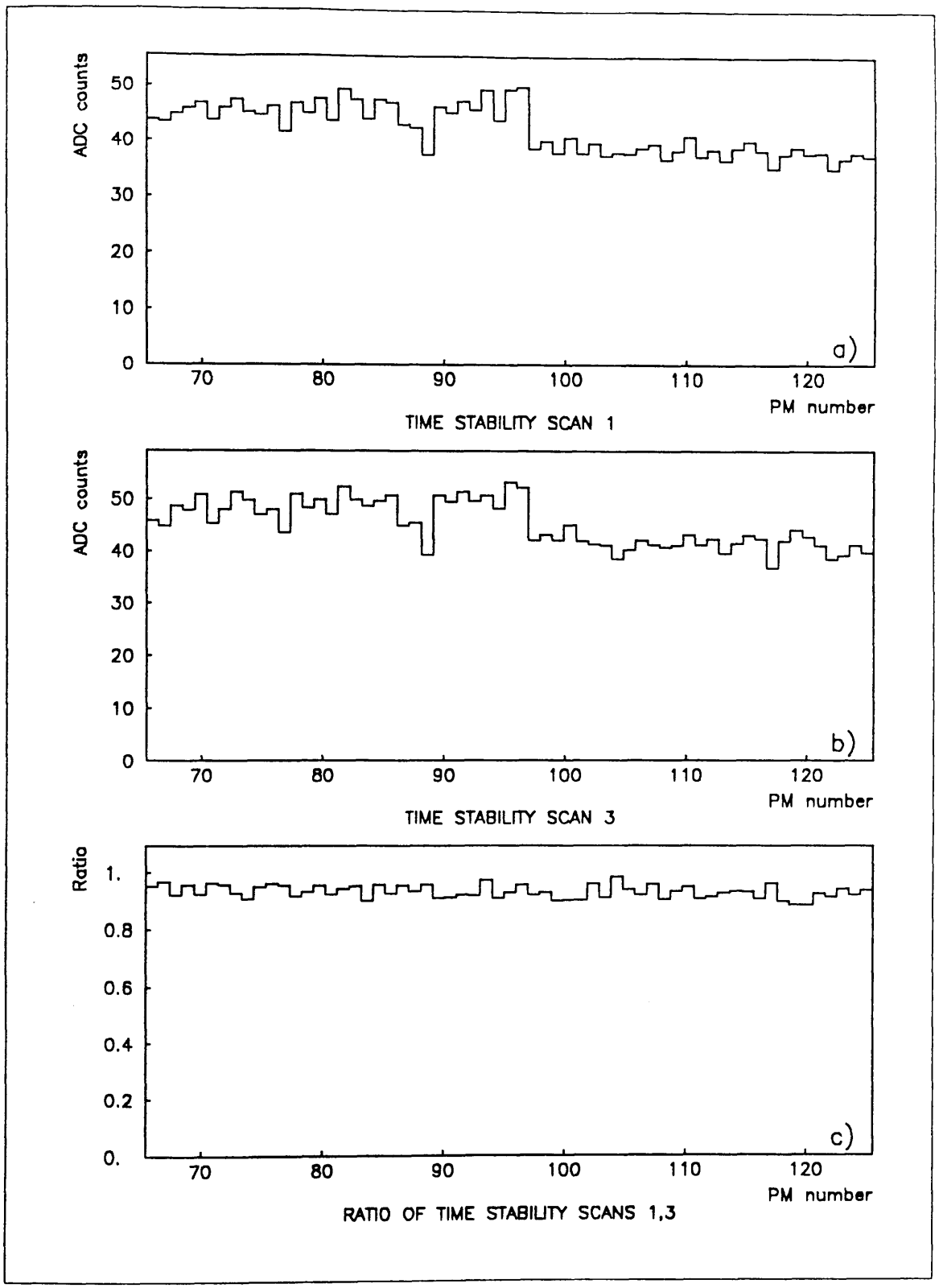

Figure 15: Successive source scans, separated by 40 days

4.3.2 Possible Errors due to Hardware Configuration

Because of the relatively low strength of the radioactive sources (5 mCi each), the source system does not use the ADCs in the configuration used by the data acquisition system. The ADCs are normally used with a 110 ns gate (that is, the current from the PMs is integrated over this period of time), and an output signal of a few thousand counts is produced. The source system runs with a 10 μs gate, and the output signal is between 5 and 80 counts, depending on the width of the channel and the position of the source (whether it is on level 1 or level 2, and whether it is the back or the front source). Since this is near the gate specification limits of the ADC units used, it was necessary to test whether the ADCs were giving inaccurate readings. Two separate tests were made.

The first test carried out was to decrease the gate time from 10 μs to 2 μs; the standard section was scanned, and the results compared with previous scans. Figure 16 a), b) and c) show plots of the source data with 10 μs gate, with 2 μs gate, and their ratio. The RMS on plot c) is 1.2%, again within the expected statistical errors. It should be noted that this does not prove that the ADC output varies linearly with the gate period, but simply that all the ADC channels vary by the same factor. Since the source was not designed to calibrate on an absolute energy scale, this does not matter.

The second test made was to exchange two adjacent ADC cards, scan the appropriate section, and compare with data from normal scans of that section. The purpose of this was to check that all ADC channels gave the same output count for a given input signal. The section scanned was quadrant 1, segment 1-Y, using the front source on PMs 2 to 96. The results are shown in figures 17 a), b) and c); the RMS contribution from each data set here is 3%. This is high compared with the 0.7% expected, but is considerably less than the 25% error that would be expected if the fluctuations in the raw data were in fact due to the ADC cards. (It is known that this test scan was made under poor conditions).

The above results show that the source measurements are reproducible over a period of weeks, and that any errors introduced by the changed configuration of the hardware are too small to be the cause of the known effects in the data.

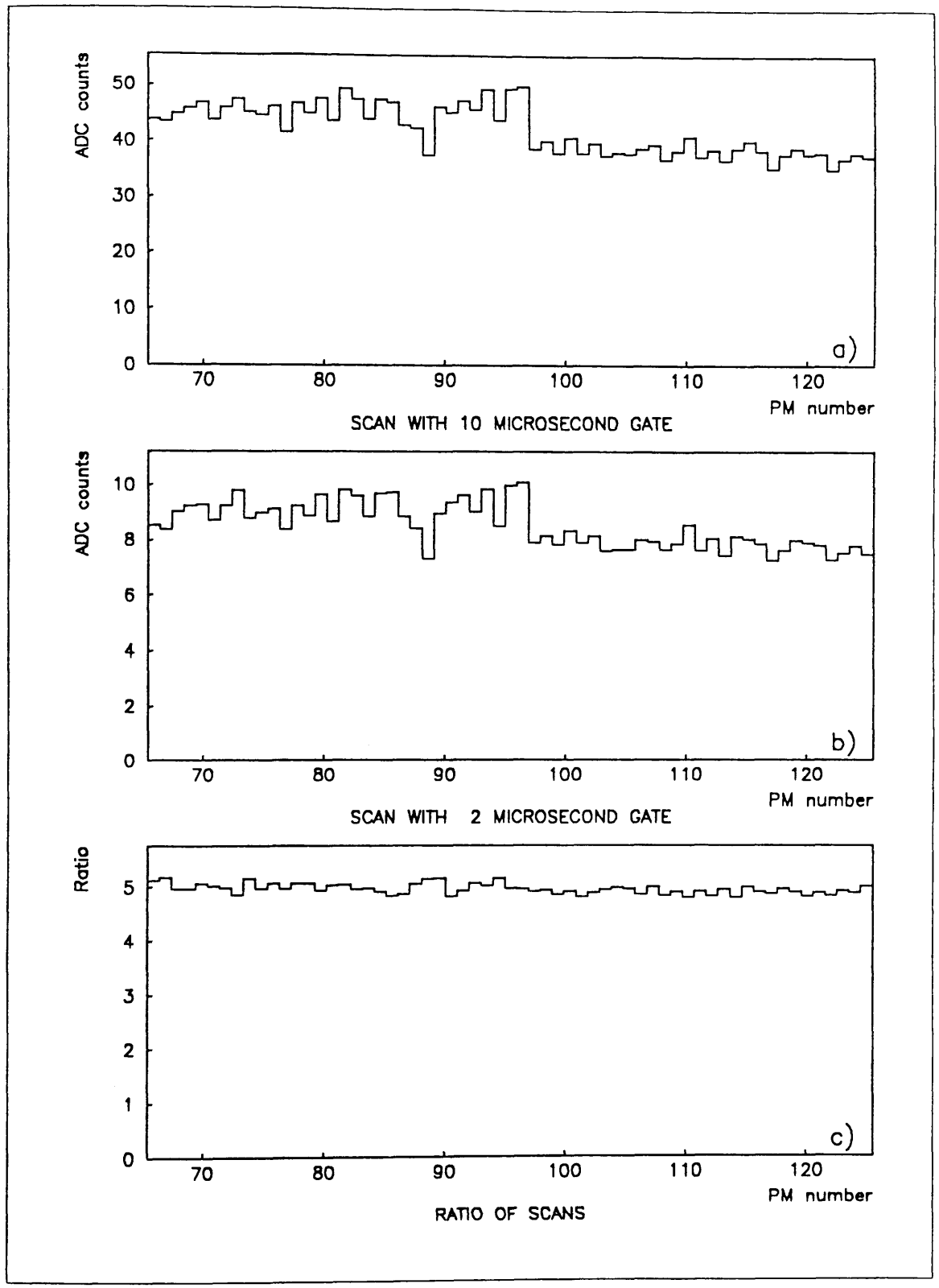

Figure 16: Source scans with gate lengths of 10 μs and 2 μs

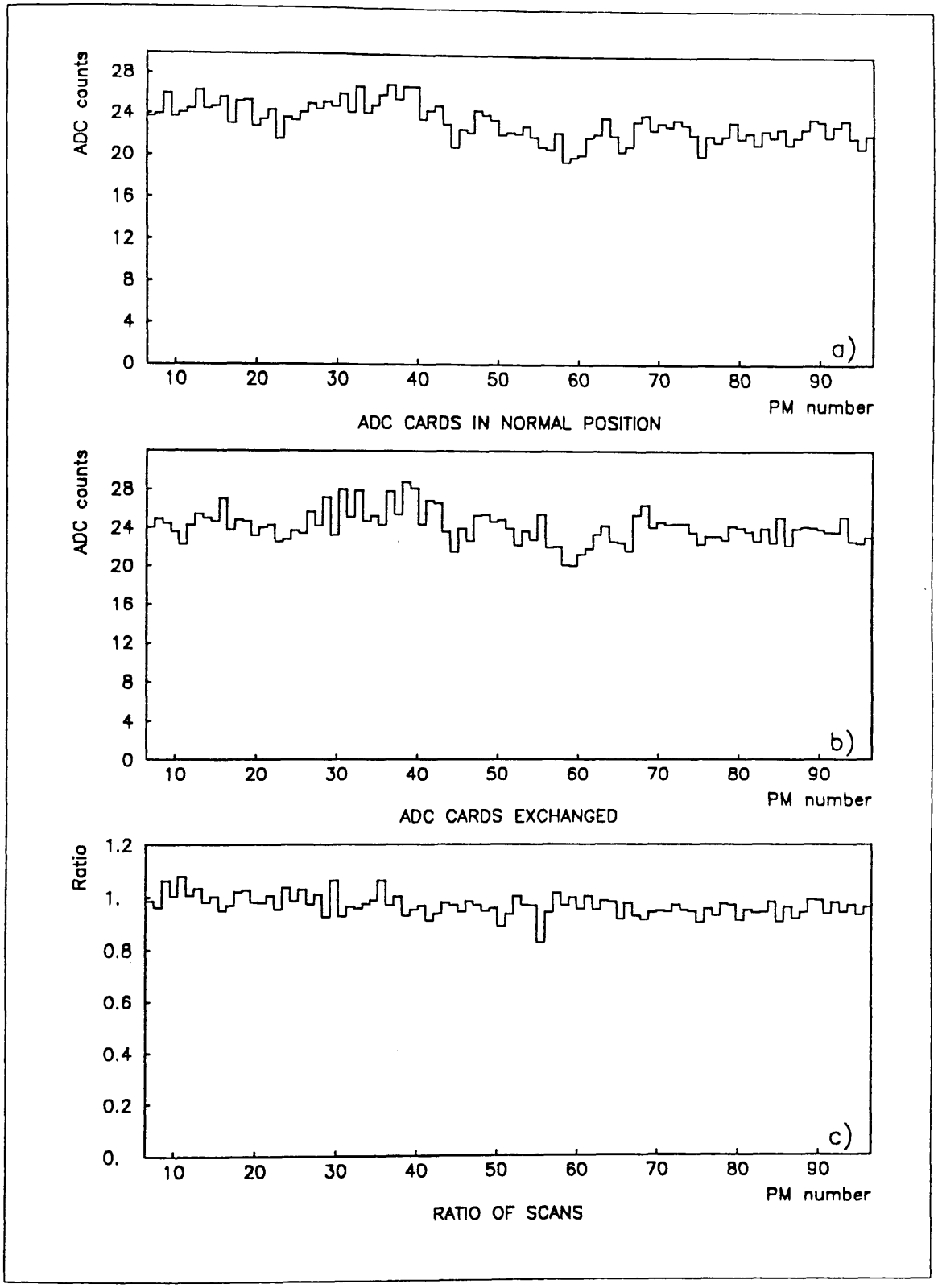

Figure 17: Source scans with ADC cards exchanged

4.3.3 A Test on the Possibility of 'Sagging' in the PM tubes

One of the features noted in the data was the systematic decrease in the source signal with increasing PM number. One hypothesis was that this was due to 'sagging' in the PMs. Sagging occurs when the PM is subject to a continuous light signal, and thus a continuous current exists in the dynode chain. This causes the potentials applied to the dynodes to vary from their normal values, and hence changes the gain of the PMs (In normal use, the light signal seen by the PMs comes in short pulses, and the dynode potentials do not have time to alter). In addition, the PMs were arranged so that those that required the highest voltages for a given gain were placed nearest the beam-hole, and those requiring the lowest voltage were placed away from the beam-hole. Thus changes in gain due to sagging would be systematic across the calorimeter. Attempts were made to test this by making a global change in the PM gains across one segment, thus altering the PM current, and the amount of sagging (if any). The scans were made on quadrant 2 segment 1, using the back source to measure three sections of the segment. Three sets of measurements were made – with the PMs at the normal gain, with the gains increased by 30%, and finally with the gains decreased by 30%. (The gain changes were made using the laser system, and the results were not checked afterwards.) The raw data is shown in figures 18 a), b) and c). Figures d) and e) show the ratio of b) to a), and c) to a) respectively. There is no measurable slope in either of the last two plots, implying that the increase in gains did not result in any subsequent (systematic) increase in the sagging. The RMS on the plots is 1.3% – within statistical errors.

The fact that there is no slope, and that the RMS is within the expected errors also implies that the laser system can make changes in the PM gains of at least 30% in a controlled fashion. However, from figures 18 d) and e) it can be seen that the average ratios are 0.77 and 1.51 respectively, corresponding to gain changes of +30% and −34%. Thus the laser cannot be relied upon to make accurate changes – it must be used 'iteratively'.

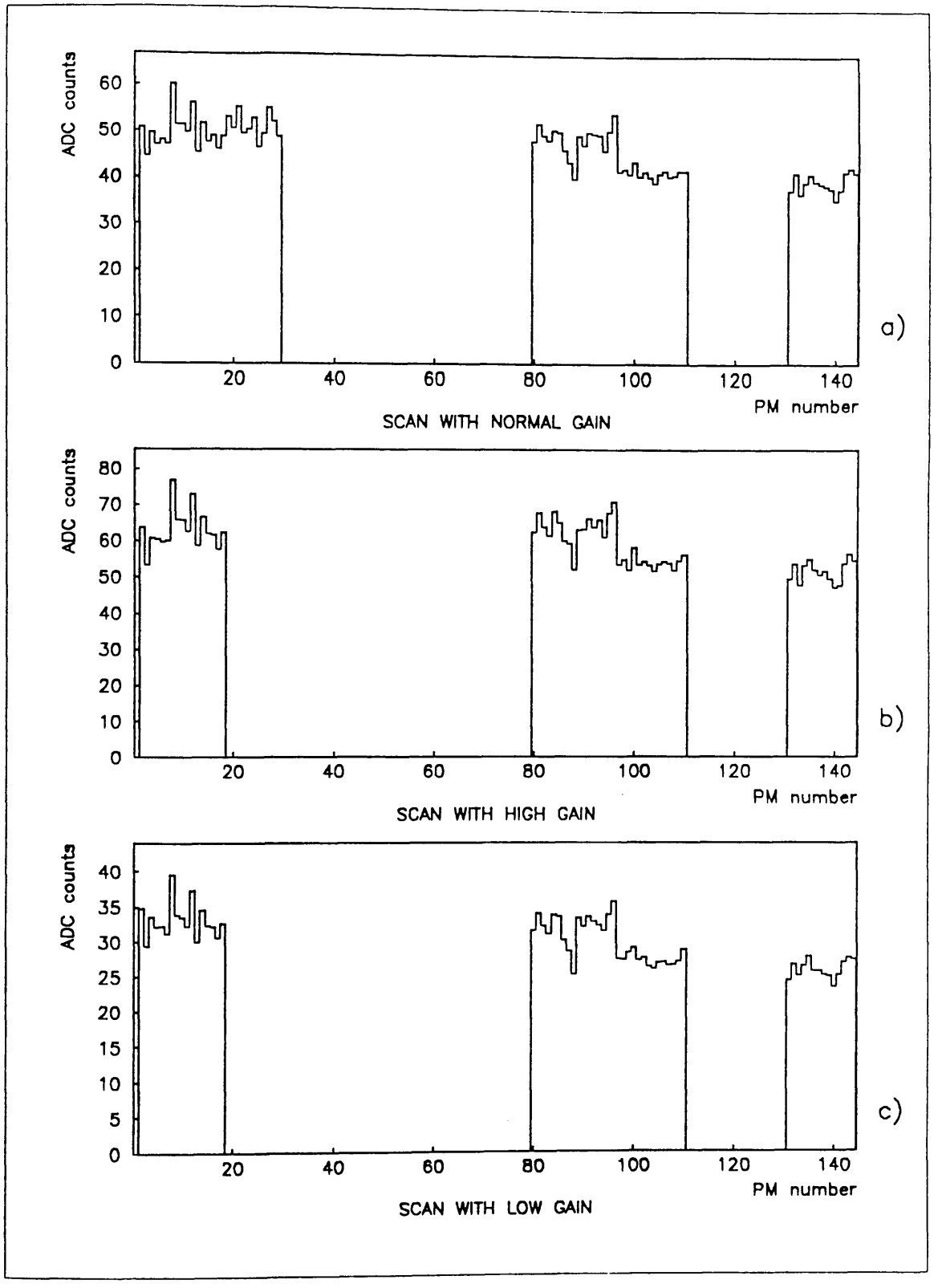

Figure 18: a), b), c): Source scans with gains changes of ± 30%

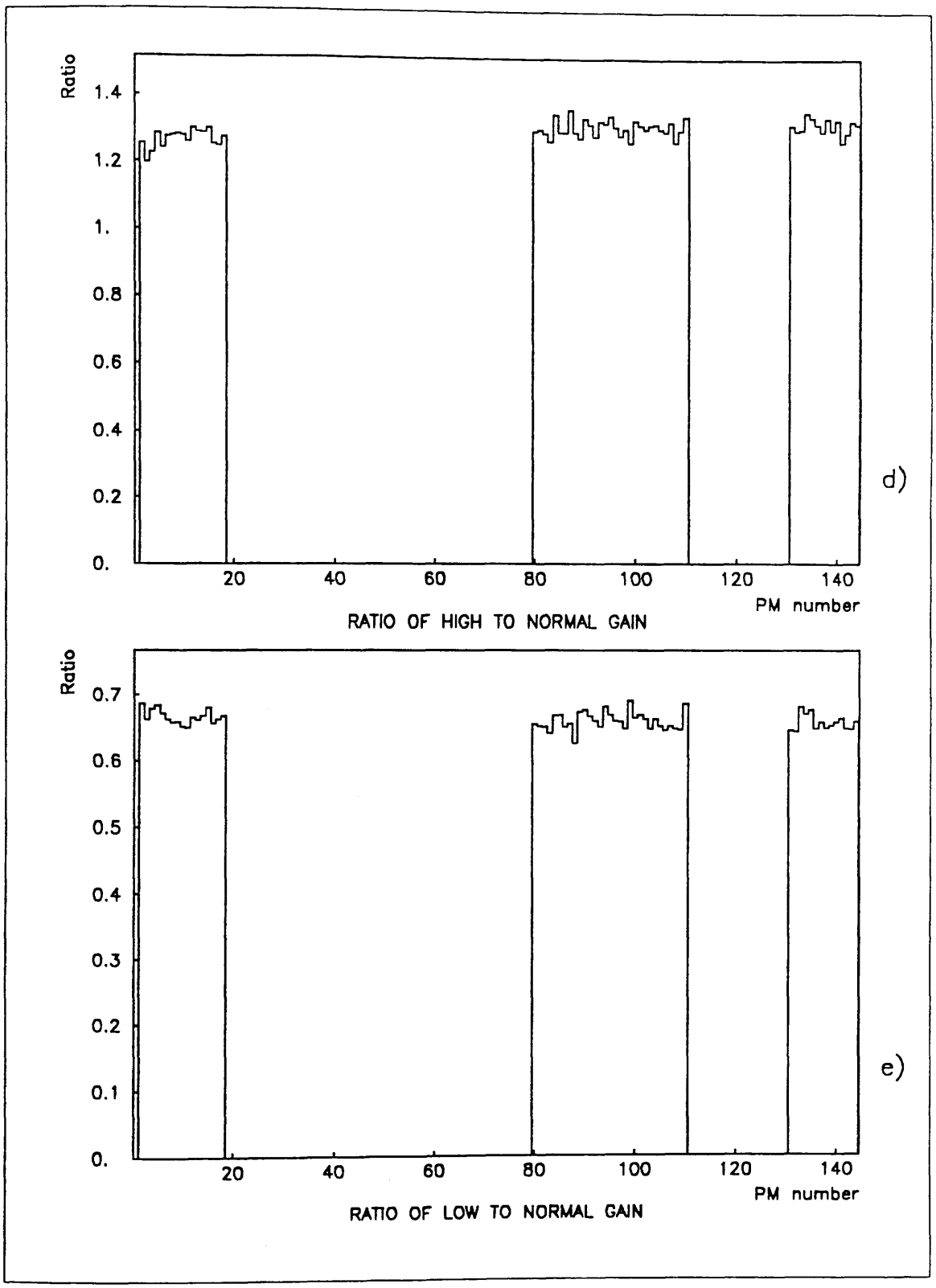

Figure 18: d), e): Ratio of gain-change scans

4.3.4 The Ratio of Signals from Wide and Narrow Channels

The output signal from the wide detector channels is approximately twice that from the narrow channels, as would be expected. Precise values were calculated from the source data, and are given in table 1.

Y (Front)	Z (Front)	Y (Back)	Z(Back)
2.00 ± 1.0%	1.90 ± 1.4%	1.82 ± 2.0%	1.96 ± 2.0%

Table 1: Ratio of output signals from wide and narrow channels (from scan data)

It is possible to measure the expected value indirectly, by placing a source mid-way between two narrow channels, and measuring their outputs, and then comparing their sum with the output from a wide channel in the same segment. Several such measurements were made, and their average taken. The results are shown in table 2.

Y (Front)	Z (Front)	Y (Back)	Z(Back)
1.76 ± 1.5%	1.75 ± 1.2%	1.68 ± 1.4%	1.77 ± 1.5%

Table 2: Source measurement of wide to narrow ratio (indirect measurement technique)

A comparison of tables 1 and 2 shows that there is a larger step between wide and narrow channels in the source-scan data than would be expected from the test measurements.

The steps may be attributable to the difference between the optical coupling of narrow and wide channels to the PMs.

4.4 Tests on the Laser System

The Geneva and Neuchatel groups carried out a series of tests on the laser system to try to find causes of the problems mentioned in the source data discussed above. The following conclusions were reached.

i) Using the laser system to set the gains of the PMs could result in the gains changing systematically across the calorimeter – ie could produce slopes.

The method of equalisation used by the laser system has been described in detail in the previous chapter. Briefly, the gain of a given PM is set on the assumption that an equal amount of light is injected into each detector channel; then, if the PM output is higher than the average for the segment, the gain will be decreased proportionately. In practice, it was found that because the laser light had to traverse longer lengths of light-fibre to reach the more distant PMs, the light input varied systematically across the segment, and PMs closer to the beam-hole (further from the laser) were set at too high a gain.

From the measurements made, it was calculated that this effect could cause a slope across the calorimeter of about 12%.

ii) The light emitted from the light fibres is collimated, and travels along the scintillator tubes with little angular divergence. The result is that only a small section of the photocathode is illuminated by the laser, whereas light from an e.m. shower in the calorimeter would illuminate the whole cathode. Since the photocathode response

varies over its surface, the gain set by the laser may vary from channel to channel, depending on the characteristics of the PM and on the angle at which the laser light enters the teflon tube.

iii) The light transmitted to the light fibre, and the proportion passed by the light fibre, can vary with injection angle, and the amount by which the fibre is bent, with the result that the amount of light reaching the relevant detector channel may vary from channel to channel. It is known that the bending of the light-fibres does vary systematically across the calorimeter, due to the way in which the light-fibres are installed.

4.5 Homogeneity of the Calorimeter and Source System

Using the source system, a given PM can be measured from four positions – from level 1 or level 2 using either the back or the front source. The strengths of the sources are known to within 2%, allowing all readings to be compared directly, in principle. In practice, as described in the previous chapter, there are several other factors which must also be taken into account:

i) the attenuation of the signal between levels 1 and 2 (2.04 $\pm$3% over 138 cm);

ii) the different way that back and front sources 'see' the detector segment (section 3.4);

iii) the higher signal from wide tubes, compared with narrow ones (discussed above in this chapter);

All of these factors should be constant over a given segment, provided that the calorimeter is homogeneous. Thus the ratio of level 1 to level 2 signals should be constant, as should the ratio of back to front signals. Figures 19 a) to d) show the ratio of

a) Level 2:Level 1 (Back)

b) Level 2:Level 1 (Front)

c) Front:Back (Level 1)

d) Front:Back (Level 2)

for the data data previously shown in figure 13. The RMSs on these ratios are better than would be expected if there were no correlation between the contributing data sets, but are certainly too high to be attributed simply to statistical errors on the measurements. In addition, the plots of the ratios show slopes of a few percent.

The conclusion is that the source measurements are affected by structure within the calorimeter. Three of the more obvious candidates for the cause(s) of these effects are discussed below. (It should be remembered that the segments are designed to be completely homogeneous throughout their active volume, although the coupling of the scintillator tubes to the PMs is not – they may be coupled to either the wide-channel or narrow-channel type.)

i) Hydrostatic Pressure

The segments are filled with liquid scintillator, which is not confined to the teflon tubes but permeates the whole of the segment. The pressure would cause the segments to bulge if it were not for the compression modules, and it is possible that there is a residual bulge in some segments. Over distances of 10 cm or more, this could cause significant differences (a few millimetres) in the source/segment separation; it is unlikely to have any effect over smaller distances.

ii) Epoxy Bags

During construction, epoxy was poured into polythene bags inserted between the segemnts, to take up any irregularities in the segment surfaces. The bags separate the 'front source' plates from the segment that they measure, while 'back source' plates are in direct contact with the segment concerned. Irregularities in the epoxy bag may cause the source/segment separation to change with position; again, this

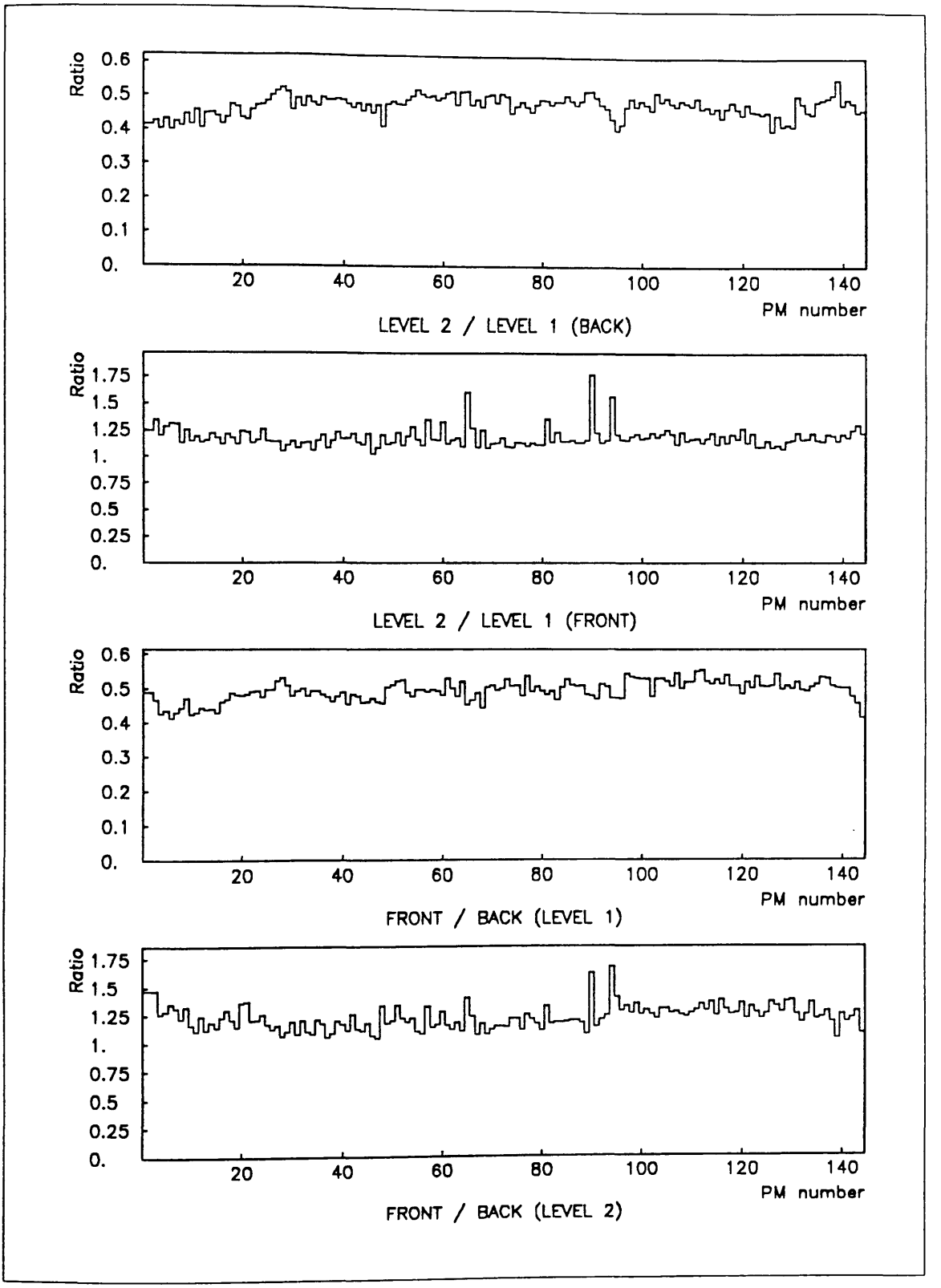

Figure 19: Ratios for measurements of Segment 2, Quadrant 3 from different positions

would be unlikely to cause changes over source scan distances of less than 10 centimetres.

iii) The Scintillator Attenuation Length

Local fluctuations in the quality of the scintillator (due to radiation damage or dissolved gases) would cause inhomogeneities in the attenuation length, and would lead to discrepancies in the ratio of level 1 to level 2 readings, and in front to back readings.

In addition to causing differences in the level 1, level 2, front and back readings, the three effects discussed above would also cause fluctuations in the apparent relative gains of the PMs

4.6 Use of the Source Data

From the preceding two sections, it can be seen that the effects seen in the source data (slopes and fluctuations) could have been imposed by the laser system, or could be the result of inhomogeneities in the calorimeter. In the first case, the correct way to set the gains of the PMs would be to use the source data rather than the laser data. If, on the other hand, the problems are due to the bulges in the calorimeter, or due to varying thickness of the epoxy bags, then there would be little or no effect on the physics data (the showering in the calorimeter is not affected by the source/calorimeter distance !). Variations in the scintillator attenuation length, however, would have to be removed (for instance, by replacing the scintillator) or at the least, 'mapped', and later corrected for in the software.

At the time of the physics run in April 1984, there was no firm evidence that the laser system was the cause of the problems, and the gains of the PMs were set up using the laser data. In principle (and with one proviso) this does not matter, since a correction file can be used in the off-line software, correcting each ADC signal in an event before the event recon-

struction begins. The exception mentioned is that the trigger is dependent on the calibration at the time of data taking. If the calibration is set such that it is believed that showers at a Pt of 3 GeV/c or greater will cause a trigger, whereas in fact the threshold is actually at 4 GeV/c, the final data set will contain no showers between 3 and 4 GeV/c in Pt, no matter what corrections are later applied offline.

The source data from the scans made at the end of the physics run, in June 1984, were used to create a correction file for the event reconstruction programs. The file contained a correction factor for each PM in the calorimeter, based solely on the data from the source scans. That is, it was assumed that the effects seen in the source data were all imposed by the laser system, and that by correcting with the source data, a 'perfect' calibration would be attained.

It should be noted that if the source data were incorrect, this procedure would impose slopes on the calibration (15% on average), and the effects could be easily seen in the physics analysis – for instance, by plotting the π^0 mass as a function of Y, for a fixed Z value. However, if the source data are correct, no such effects would be caused.

4.6.1 Normalisation Between the Different Scan Sections

It has already been pointed out that there are factors of approximately 2 between level 1 and level 2 signals, narrow and wide signals, etc, and the average values have been given previously. These factors are available because they are measurements on the same PM from different positions. This is not the case for measurements of Y and Z tubes, even where they are measured by the same source. There are thus two unknown factors involved in relating measurements on the calibration of the calorimeter. One of these can be ignored since the absolute scale of the calibration system is not required. The correction file produced is then, in effect, two sets of numbers normalised to 1.0, one set relating to the Y tubes, and one set to the Z tubes. When using this file, it is assumed that there are enough sets of separate Y and Z sections (24 of each) that they average out to the 'correct' normalisation. This as-

sumption is justified by the fact that the PM gains were initially set to the gains calculated during the parametrisation of the tubes (chapter 2) and there is thus no reason for there to be any systematic differences between the Y and Z sections. In addition, when analysing data corrected by the source file, no difference is seen between the energy a shower deposits in the Y PMs and in the Z PMs (See below).

4.6.2 Tests of the Source Correction using Physics Data.

To investigate the value of the source correction file, and the source measurements in general, a subset of the 1984 physics data was examined, both with and without the source corrections applied to the data. The results were compared to try and understand the effects of the source data on the calibration. Some of the results are discussed below.

4.6.3 Normalisation Between the Quadrants.

The π^0 signal in the 1984 data was examined to find the apparent π^0 mass in each quadrant (In this section, π^0 signal refers to the peak at 135 MeV seen in the gamma-gamma invariant mass spectrum). The values obtained, relative to the mass of the π^0 in quadrant 1, are given in table 3, together with the average source signal (again, relative to the average signal from quadrant 1). The signals were corrected for source strength and channel-type (Front, Back, Y, Z, etc). The values are the same, within errors, implying that source data can provide the correct (relative) normalisation of the four quadrants.

4.6.4 The ratio $(E_y - E_z)/(E_y + E_z)$

A shower developing through a segment deposits the same energy in the scintillator tubes measuring the Y co-ordinate as it does in those measuring the Z co-ordinate. A useful way to examine the accuracy of the equalisation, then, is to examine the proportional difference between the energy measured in the Y PMs (E_y) and the energy measured in the Z PMs (E_z). The quantities being measured are dependent; the gain of the PMs carrying out

	Quadrant 1	Quadrant 2	Quadrant 3	Quadrant 4
π^0	1.000 ± 0.00	0.94 ± 0.02	0.97 ± 0.02	0.93 ± 0.02
Source	1.000 ± 0.00	0.93 ± 0.02	0.95 ± 0.05	0.94 ± 0.02

Table 3: *Relative masses for the π^0 signal, and relative source signals, in each quadrant.*

the measurements are independent. Moreover, the Y co-ordinate and the Z co-ordinate of the shower are independent, so by examining the ratio

$$R_{energy} = (E_y - E_z)/(E_y + E_z)$$

as a function of Y, with Z fixed, (or vice versa), it will be possible to determine whether the source is imposing a slope or correcting for one. Figure 20 shows R_{energy} as a function of Y for a fixed region in Z, with both corrected and uncorrected data. The uncorrected data clearly shows a slope, while the corrected data shows virtually no change with Y; in addition, the average value of the ratio is much closer to zero (as it should be if $E_y = E_z$).

4.6.5 Electron-Beam Scan of the Calorimeter.

Figure 21 shows the results of two successive electron-beam scans of quadrant 2, segment 1, Y, made after the 1984 physics run. The PMs were equalised using the source data. Although there is structure in the data (the RMS is 5%), the signal does not vary systematically with position, again implying that the source system is removing, rather than imposing, a slope.

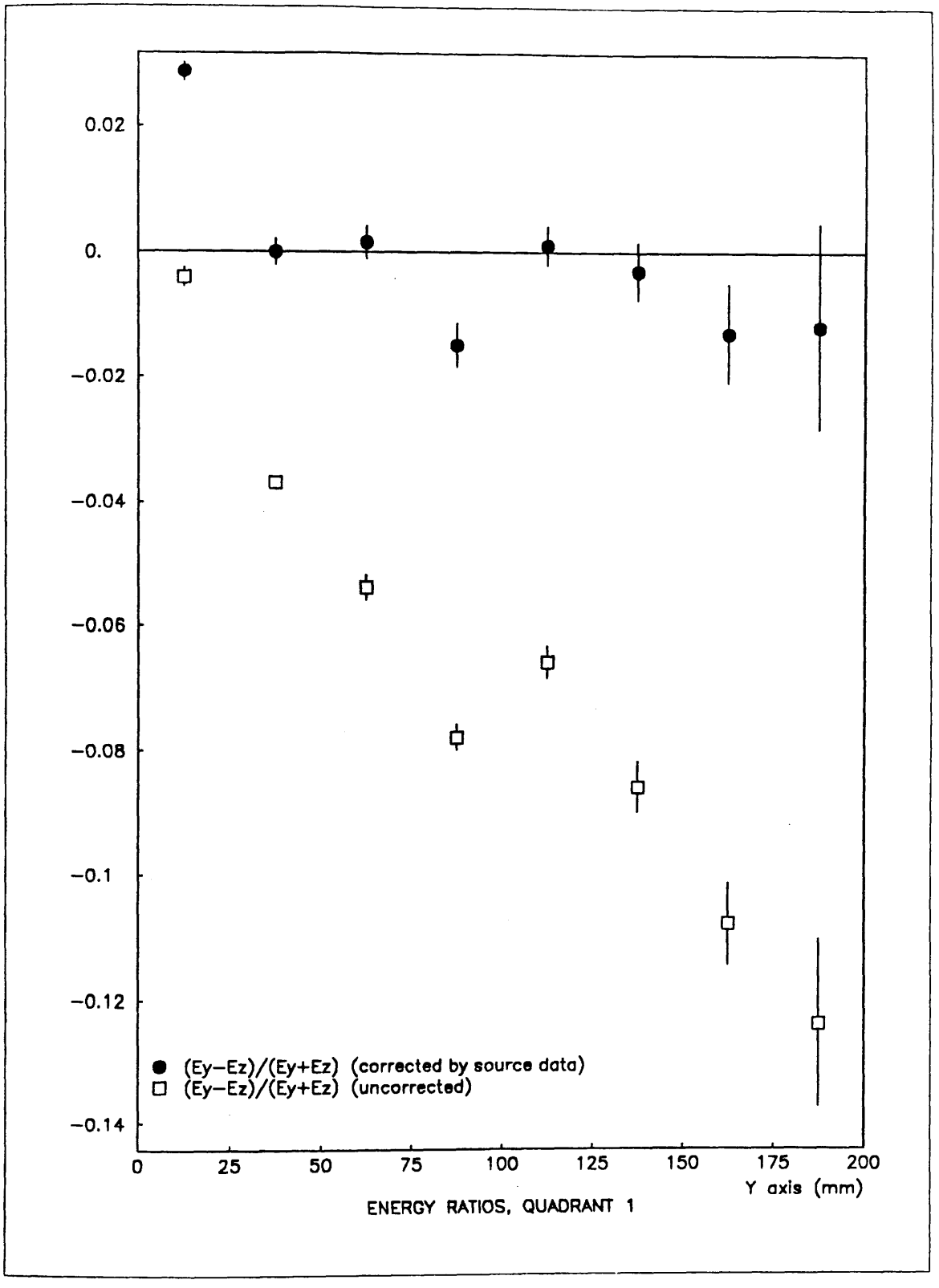

Figure 20: R_{energy} calculated over a fixed region in Z

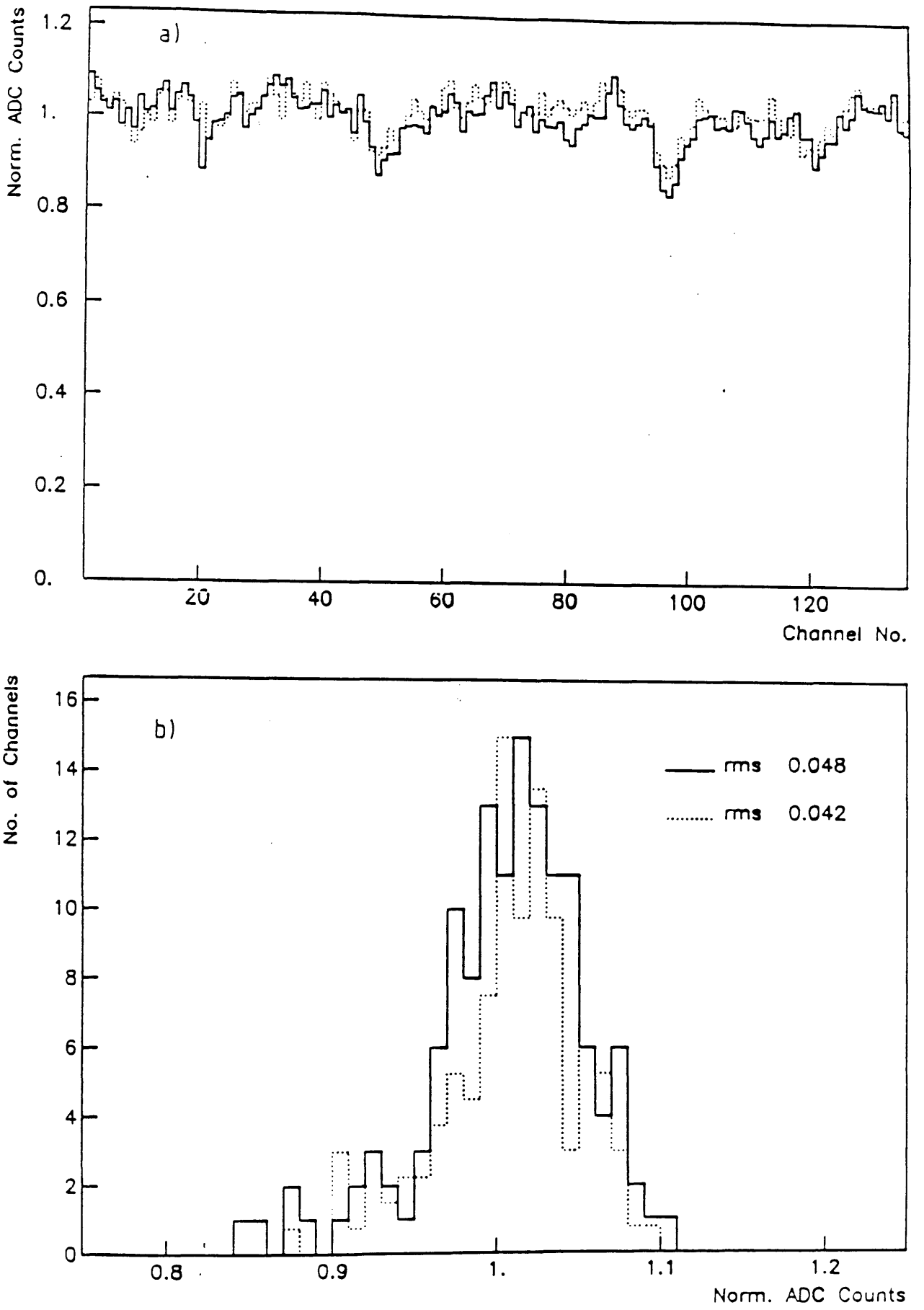

Figure 21: Electron-Beam scan of calorimeter quadrant 2

4.7 Conclusions

Source scans of the calorimeter, when the PMs have been equalised by the laser system, show fluctuations in the gains of between 5% and 10%, and systematic changes in the gains of up to 25%. In addition, the quadrant to quadrant normalisation factors vary by up to 10%. If the source data is used to correct for these, either off-line in the data analysis, or in the equalisation of the calorimeter, the quality of the data is improved. For this reason, it was decided to use the source data to correct the 1984 physics data during analysis.

5. THE PATTERN RECOGNITION PROGRAM

5.1 Introduction

The WA70 pattern recognition program (PATREC) has the job of reconstructing the form of the original showers detected in the calorimeter. Before trying to understand how PATREC works, it is necessary to understand the way in which the calorimeter records a shower that occurs within it – that is, the way in which the information obtained from the calorimeter is related to the physical shower.

As a shower develops through a segment, it deposits energy into the detector channels. The number of Y channels producing a signal depends on the shower's lateral development along the Y axis; the relative strengths of those signals give the profile of the shower in that view (its projection onto the Y axis). The same is true of the Z channels. The Y-Z position of the shower can therefore be calculated from these signals. The three segments in a quadrant together provide information on the shower's longitudinal development

The information derived from the calorimeter therefore represents a set of 1-dimensional shower projections which are themselves subdivided along the axis of projection; the number of showers originally present is not simply related to the number of shower projections, since showers need not deposit energy in all three segments, and may partially or completely overlap one another.

Therefore, before an event can be studied, PATREC must reconstruct the shower projections from the recorded ADC signals; it must then match them in the X, Y and Z co-ordinates.

PATREC can be considered in three logically separate sections. The first deals with the 'housekeeping' involved in reading an event from tape and decoding it. This will not be dis-

cussed since it has no physics content. The second part of PATREC deals with the initial checks and corrections on the data, and with some cuts on the TOF. The final section contains the 'intelligence' of the program – it is here that the ADC signals are reconstructed into showers.

5.2 Checks, Corrections and Cuts

5.2.1 Pedestal Drift

The data read in from tape contains a file of the ADC and TDC pedestals measured at the beginning of each run (section 2.5.1). Since is possible for the pedestals to drift significantly during a single run, PATREC checks them after every two hundred events. If pedestal drift is found, the program will be aborted.

5.2.2 Bad PM Channels

There are a number of channels where either the PM or the ADC are known to be faulty. Such channels cannot be simply ignored, or set to zero, since this may split a shower, causing it to appear as two separate showers. The solution adopted is to discard the ADC signal, and replace it with the geometric mean of the two neighbouring channels.

5.2.3 PM Gain Corrections

Two correction files are applied to the ADC data. The first is the source file, discussed in the chapter 4. The second is derived from laser scans of the calorimeter, made every few days. The scans measure the drift in the PM gains relative to their values at the start of the run. The drift is less than five percent over the whole of the data taking period.

5.2.4 'MICE' Cuts

The corrected data is passed to the MICE filter. This is a routine which emulates the third-level trigger selection applied during data taking (chapter 2). There are two reasons for including this routine in PATREC:

i) During data taking, the MICE trigger was run in either flagging mode or in rejection mode. In the latter mode, only events which met the MICE trigger criteria would be passed to the data acquisition. In flagging mode, however, all events reaching the MICE trigger were passed to the data acquisition, although those which would have been rejected on the MICE criteria were flagged. Running MICE in PATREC allows such events to be either examined or rejected.

ii) The software version of MICE can identify up to 10 different trigger cells, whereas the hardware version could only deal with 2.

5.2.5 TOF Cuts

The remaining work carried out by this section of the program is concerned with rejecting events that are actually two interactions recorded as one. These occur when an event causes a trigger, and a second event then occurs within the ADC gate-period of 100ns. The following calculations and rejections are made:

i) The S2 value is calculated.

The use of the S2 beam counter as a stop signal for the TOF has been described in chapter 2. Since there can be large uncertainties in the measured timing for this signal, a value for the S2 is reconstructed from the data. This is done by making rough matches of Y and Z TDC signals; for each PM pair this gives the values

$$Y,\quad Z,\quad Y+S2,\quad Z+S2,$$

from which S2 can be calculated. For most events the calculated S2 values cluster around an average value; in some cases, however, two or more distinct values of S2 are found. This is the result of a second event occurring while the first is still being recorded (event pile-up).

ii) If there are 2 or more values of S2, the event is rejected, since it probably consists of two overlapping events.

iii) A cut is made on the number of showers with no TOF values. Again, these are due to overlapped events. In this case the second event occurred after the stop signal from the S2 counter had reached the timers, and therefore generated no TOF signals.

iv) If the calculated value for the S2 signal is equivalent to a distance of less than -50 cm or greater than 200 cm the event is rejected. The purpose of this cut is to reject triggers caused by showers in the scintillator tubes outside of the lead sheets, or in light guides (the light guides couple the scintillator tubes to the PMs).

v) The trigger shower is examined, and the quantity

$$|(Y - T_y) - (Z - T_z)|$$

is calculated. Y and Z are the positions of the PMs being considered; Ty and Tz are the positions coresponding to the Time-Of-Flight values for the shower, derived from the Z and Y PMs respectively. If the value is less than 40 cm, then the event is accepted. If not, and either Ty or Tz are greater than 200 cm, the event is rejected.

An event surviving these cuts is then passed to the reconstruction routines.

5.3 Event Reconstruction

This section describes how the ADC signals are reconstructed into showers. The reconstruction is carried out in three steps:

i) The ADCs in a single segment are grouped into clusters.

ii) The clusters are matched in depth – that is, the clusters in segment 3 are matched with those in segment 2 and then with those in segment 1, producing 1-dimensional shower projections.

iii) Finally, the Y and Z shower projections are matched to form 2-dimensional showers.

Each quadrant is dealt with separately; in the following descriptions it is assumed that only a single quadrant is being considered.

5.3.1 Grouping ADCs into Clusters.

An algorithm finds the largest ADC in the quadrant, and then searches for a minimum on each side of its position. The two minima then define a cluster; the ADCs within this cluster are removed from the search, and the algorithm is repeated until all of the ADC signals are grouped into clusters.

The definition of a minimum used by the algorithm is important, since there are a number of different ways in which the signal may show a minimum. The two cases that the algorithm must recognise as minima are those where the cluster is isolated from any other shower, and those where two showers overlap. In the latter case, the algorithm must distinguish between genuine minima and those caused by fluctuations in the shower profile (caused by the statistical nature of the shower's development). It does this by only accepting as genuine those increases that are greater than a certain percentage of the cluster's maximum ADC signal.

5.3.2 Adding Clusters in Depth

The clusters in each segment are now matched to produce 1-dimensional showers. The matching is done on the basis of position only.

A segment 3 cluster is chosen, and a line projected back from it to the target. Segment 2 is then searched for the cluster that is both closest to this line, and within position cuts. If such a cluster is found, segment 1 is searched in the same fashion. This is repeated for all segment 3 clusters, and the result is a set of showers in segment 3 only, in segments 3 and 2, or in all three segments. A similar algorithm is then applied to the clusters remaining in segments 2 and 1, producing showers in either segment 2 only, or in segments 2 and 1. The remaining segment 1 clusters are then classed as showers that developed in segment 1 only.

5.3.3 Overlapping Showers

Having added the showers in depth to produce 1-dimensional shower projections, the results are examined for overlapping showers. Where these are found, the energy is shared between the two showers in a fashion dependent on their profiles. The accuracy of this process depends on the degree to which the showers overlap. As an example, showers overlapping in segment 3 only may be separated by considering the relative sizes of the profiles in segments 1 and 2, allowing the calculation to be made with reasonable accuracy, especially if the energy in segment 3 is only a small proportion of the overall energy. If the showers overlap in both segments 2 *and* 3, however, they must be separated only on the basis of the segment 1 signals, and consequently the result is much less accurate, and effects a much larger proportion of the signal. Showers that are overlapped in all three segments will not be corrected by this routine since they will appear as just one shower.

Showers do not have to be physically close in the calorimeter to overlap; generally it is only their projections onto the Y or Z axes that merge. Because of this, showers that fully overlap in one projection may still be 'rescued' if they can be correctly matched with their projections on the other axis.

Showers that do not overlap with any other showers are referred to in this and later chapters as 'clean' showers, while those that do overlap in one or both projections are referred to as 'dirty' showers. The reason why the distinction needs to be made is discussed in the final section of this chapter.

5.3.4 Matching in Y and Z

At this point, the ADC signals have been allocated to a set of 1-dimensional showers characterised by a position (in Y or Z), a TOF value (position in Y or Z), a barycentre (which is essentially a measure of the longitudinal development of the shower) and an integrated ADC value. The integrated value cannot yet be converted to the energy of the shower, since it must first be corrected for the attenuation of the light-signal in the scintillator. This cannot be done before the shower co-ordinates are known.

A tentative match of two shower projections is made by using the TOF as a rough guide of each projection's 'missing' co-ordinate. On the assumption that the two showers do match, the energy for both projections can then be calculated accurately.

For simple cases, the best match can be found by examining each possible combination individually. When there are more than two showers in each projection, this becomes time consuming; for these cases the choice is made by calculating the chi-square for each fit-hypothesis, and selecting the smallest. In both cases the criteria is the degree to which the energies, TOFs, and barycentres of the two shower projections match each other.

5.4 The Output from PATREC

The end result of PATREC is a set of showers labelled by their energies and co-ordinates. In addition PATREC decides, on the basis of the shower development, whether a given shower was due to a hadron or to an electromagnetic particle (gamma or electron), and labels it as such. Other information calculated during the reconstruction is

also available. This includes the 1-dimensional shower descriptions, the segments in which the shower produced signals, etc.

5.4.1 Accuracy of the PATREC Output

The two most important quantities calculated by PATREC are the energy and the co-ordinates of the showers. The accuracy with which these are found depends on whether the shower concerned was 'clean' or 'dirty'. The energy calculated for the 'dirty' showers is less accurate than for 'clean' ones for the reasons discussed above. The calculation of the co-ordinates of a shower is based on the profile of the shower (its development through the three segments), so that this too is less accurate for 'dirty' showers than for 'clean' ones.

The overall accuracy of the shower position is $\pm$ 2.5 mm in either co-ordinate. The energy resolution is given by

$$(\sigma(E)/E)^2 = C_1^2/E + C_2^2$$

where E is the energy of the shower. The values of the parameters are

$$C_1 = 0.126 \pm 0.004 \qquad C_2 = 0.032 \pm 0.0005$$

Both the calorimeter and the PATREC program contribute to these errors.

The pattern recognition program described above was used to reconstruct the whole of the data from June 1984. The analysis described in this thesis was made on those reconstructed events.

6. DETERMINATION OF THE π^0 AND η PRODUCTION CROSS SECTIONS

6.1 Introduction

This chapter presents the analysis of the data from the WA70 experiment. It will describe the data on which the analysis was made, the stages of the analysis itself, and the sources of error in the experiment. The following chapters will then present the results and conclusions.

6.2 The Data Used in the Analysis

The data collected by the experiment had the following components:

- Data from the calorimeter. This was the raw ADC signals, together with the associated time of flight information (chapter 2).

- Data from the OMEGA wire chambers. This data was in the form of 'wire hits', representing the tracks of any charged particles that passed through the chambers during an event. At the time of analysis, the program for reconstructing the tracks [31] was not yet optimised for use with the OMEGA configuration used in the experiment. The wire chamber data could not therefore be used. Since the π^0 and η mesons are neutral particles, this did not directly affect the analysis of the calorimeter data. However, the position of the interaction vertex could not be calculated.

- Data from the trigger system. The information from the trigger (type of trigger, trigger cell position, etc) was written to tape for each event. It was used by PATREC during the reconstruction of the event.

- Scaler Information. The scalers connected to the beam counters (chapter 2) were written to tape at the end of each beam burst. They recorded the total number of particles detected by each counter during the burst, and were required to calculate absolute cross sections from the data.

The data came from 268 data taking runs, of which 199 were taken with a positive beam, and 69 with a negative beam. A run typically held 30000 events.

6.3 Outline of the Analysis Steps

The analysis was made in five logically separate stages; these were:

i) Processing of the raw data using PATREC. For each event, the position and energy of each shower in the calorimeter was reconstructed.

ii) Corrections and cuts on individual showers. This stage of the analysis rejected those showers that were considered to be 'unreliable' reconstructions, or that were unwanted for some other reason. In addition, corrections were applied that could not be applied before the PATREC processing.

iii) The main analysis of the data, based on the data produced by the previous stage. The P_t and X_f ranges were divided into bins and a $\gamma\gamma$ invariant mass spectrum was produced for each bin.

iv) Fitting the data. A fit was made to each mass spectrum, to determine the number of π^0 particles in that P_t-X_f bin.

v) Calculation of the correction factors, to correct for losses during data taking and analysis.

vi) The calculation of the production cross section.

The first stage has already been described in chapter 5, and will not be discussed again here. The subsequent stages are described in detail in the following sections. Since the method was the same for both π^0 and η, for simplicity, only the π^0 will be referred to, unless the η case differs in some way.

6.4 Corrections and Cuts on Showers

For each event, correction factors were applied to the energy of every shower reconstructed by PATREC. A set of cuts were then applied to the showers. The event was then passed to the next stage (the main analysis).

6.4.1 Shower Correction Factors

i) Correction for Energy Scale Drift

It was found that the energy scale of the ADC outputs varied gradually with time, and consequently a time dependent correction factor had to be applied to the shower energies given by PATREC. It was decided to make the correction on a run to run basis.

ii) Quadrant normalisation

It was found that each quadrant had a slightly different energy scale. A set of normalisation factors are used to correct for this. The correction factors are applied to the shower energies given by PATREC.

iii) Beam Alignment correction

It was found that the incident beam was not aligned precisely along the x-axis. This had the effect that any momenta calculated (for individual showers) had to be corrected; there was no effect on the total energy of the shower. The correction was in the form of an algorithm rather than a simple correction factor.

6.4.2 Shower Cuts

i) The guard region cut.

A guard region was defined to exclude areas of the calorimeter that were too close to either the inner or outer edges. The purpose of this was to reject showers that might have lost energy outside of the calorimeter. The guard regions were 4 cm wide around the inner edges, and 8 cm around the outer (for both Y and Z co-ordinates). The region around the outer edge was wider than that around the inner edge since showers incident in the outer areas develop at a more oblique angle (with respect to the plane of the calorimeter) and are therefore more likely to deposit energy outside of the calorimeter.

ii) The 'overlapped showers' cut.

Chapter 5 discussed the way in which showers that overlap in one or both projections can be separated by PATREC. It was decided that those showers that overlapped in both projections would be rejected, as their reconstruction was considered too unreliable.

iii) The hadronic cut.

The pattern recognition program flags showers as either hadronic or non-hadronic, based on the development of the shower through the calorimeter. Those flagged as hadronic were rejected.

iv) Cut on non-contiguous showers.

Some showers in the reconstruction were not contiguous through the calorimeter – energy was detected in segments 1 and 3 but not segment 2. These showers were rejected.

v) Cut on 'deep' showers.

Those showers that started developing only in the third segment were rejected. The reasoning behind this cut was that, since segments are each eight radiation lengths deep, it was considered unlikely that a photon or electron would not start showering before this point. Such showers were therefore considered to be hadrons, and rejected.

6.5 Details of the Main Analysis

6.5.1 Method of Analysis

The aim of this part of the analysis was to count the total number of high P_t π^0s recorded in the data; however, the apparatus was not capable of detecting the π^0 directly, since they decay almost immediately (within about 10^{-6}m of the interaction point. The η decays about 100 times faster than this). The main decay mode of the π^0 is to two gammas – other modes account for only 1.2% of π^0 decays (61.1% in the case of the η). It was therefore only the decay products, the two gammas, that were detected in the calorimeter.

The mass and 4-momentum of a 'parent' π^0 can be calculated from the energy and decay trajectory of its daughter gammas:

$$M_p^2 = 2 E_1 E_2 (1 - \cos\theta)$$

$$E_p = E_1 + E_2$$

$$\vec{p}_p = \vec{p}_1 + \vec{p}_2$$

where E_i are the energies of the particles involved, $\vec{p}_i$ are the 3-momenta, M_p is the mass of the parent particle, and θ is the angle between the trajectories of the gammas. The angle θ can be calculated from the position of the gammas in the calorimeter and the position of the decay vertex. The P_t and X_f of the parent particle can then be calculated from the 4-momentum.

Since the showers due to the two decay gammas are indistinguishable from those due to gammas from other sources (mainly low P_t π^0) and to electrons, the number of π^0 in the data must be determined in a statistical, rather than an absolute, fashion.

The analysis for this stage was therefore made in the following manner:

i) All possible shower-pairs were examined, and a set of cuts applied to each (section 6.5.2). The purpose of these cuts was to reduce the background in the final mass spectra.

ii) The mass, P_t, and X_f of the parent π^0 were calculated from the showers' energies and trajectories. Calculating the trajectory required both the position of the showers and the position of the decay vertex. Since it was not possible to derive the latter from the data, it was assumed that the vertex was at the mid-point of the target in all cases. This assumption affects the θ term in the mass calculation, causing a 5% spread in the mass peaks. It also causes a 5% error in the calculated P_t of the particle, but has less than 0.05% effect on the X_f.

iii) The mass, P_t, and X_f ranges were divided into bins, and the number of entries recorded for each bin. The result was a set of mass spectra, one for each P_t-X_f bin. Those gammas correctly paired formed a mass peak at the π^0 mass, whilst incorrect pairings only contributed to the background.

6.5.2 Cuts on Shower Pairs

Two cuts were applied to the shower pairs.

i) Cut on shower quadrant.

No pairs were accepted unless both gammas were in the same quadrant. The average separation of the gammas in those π^0 candidates whose invariant mass fell into the region $0.09 < M_p < 0.18$ GeV/c^2 was 6.5 cm, and 95% were within 13 cm (for η

particles, the corresponding values are 30.7 cm and 63 cm, for the mass range $0.5 < M_p < 0.6$ GeV/c^2). The width of a quadrant is 2 metres. This cut therefore reduces the background considerably, whilst rejecting few genuine π^0 candidates. Figure 22 shows the separation of the gammas for $\gamma\gamma$ pairs in the mass ranges given above.

ii) Cut on asymmetry.

The asymmetry of the decay is a measure of the difference in energy of the two decay gammas. It is defined as

$$\text{Asymmetry} = |E_1 - E_2| / |E_1 + E_2|$$

where the E_i are the energies of the gammas. When the parent particles have large kinetic energy (with respect to the rest mass) the asymmetry of the decays will be fairly uniform, from zero (symmetric decay, where the gammas have the same energy) to almost one (asymmetric decay, where one gamma has almost all the energy). If the paired gammas did not come from the same decay, they are unlikely to match in energy, and will have a high asymmetry. By cutting on this parameter, a large amount of background can be removed, at the cost of losing a small proportion of genuine π^0s. All shower pairs with an asymmetry greater than 0.9 were rejected. This rejects 80% of the background with a loss of 10% of the events. Figure 23 shows the asymmetry before the cut.

6.6 Fitting to the $\gamma\gamma$ Invariant Mass Spectra

Figure 24 a) shows an example of the mass plots produced by the previous stage. The plot has three components – a peak at the π^0 mass, a peak at the η mass, and a fairly flat, low level background. Figure 24 b) shows the same plot, with the scale enlarged to show the η peak more clearly.

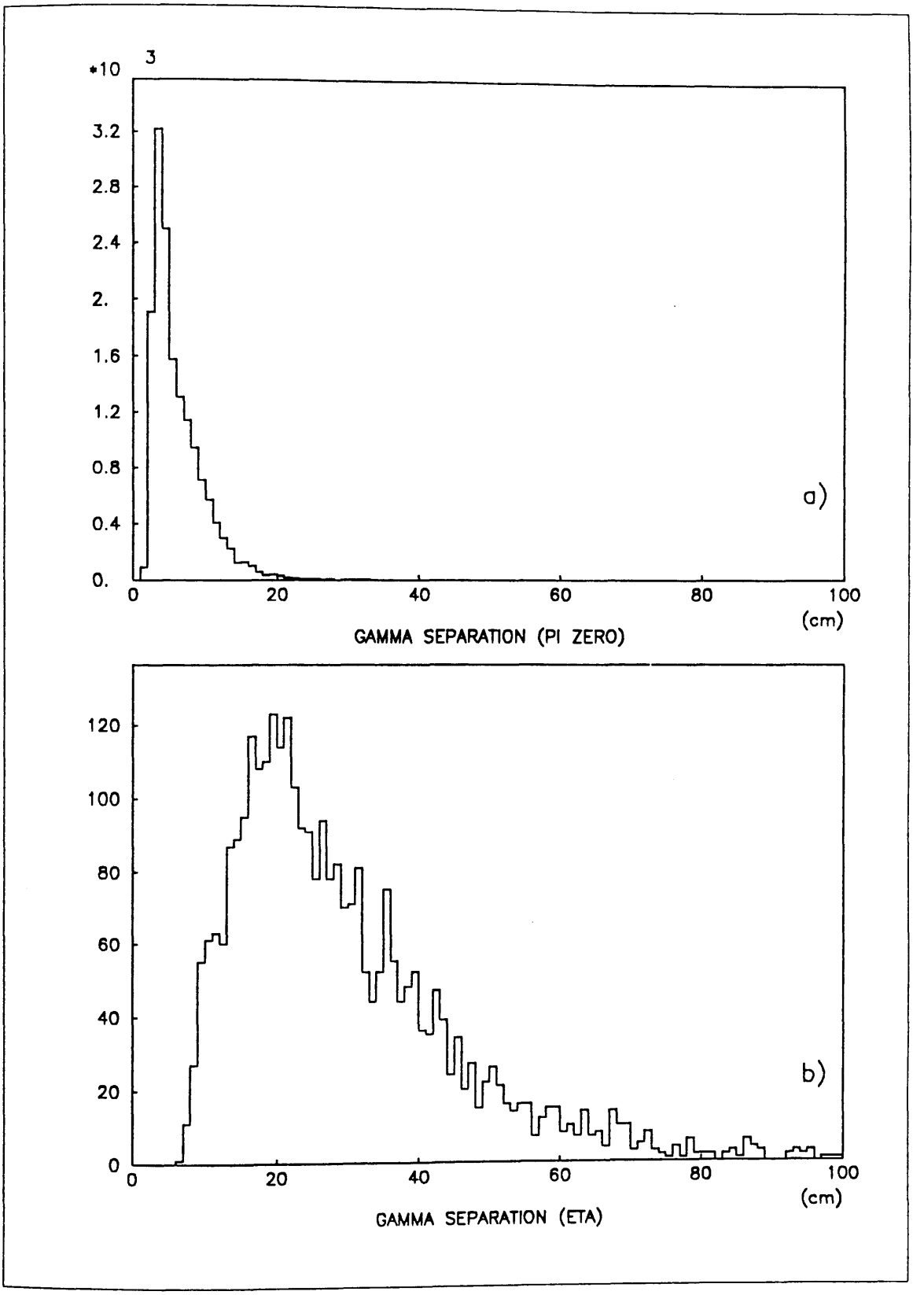

Figure 22: Separation of gammas in $\gamma\gamma$ pairs

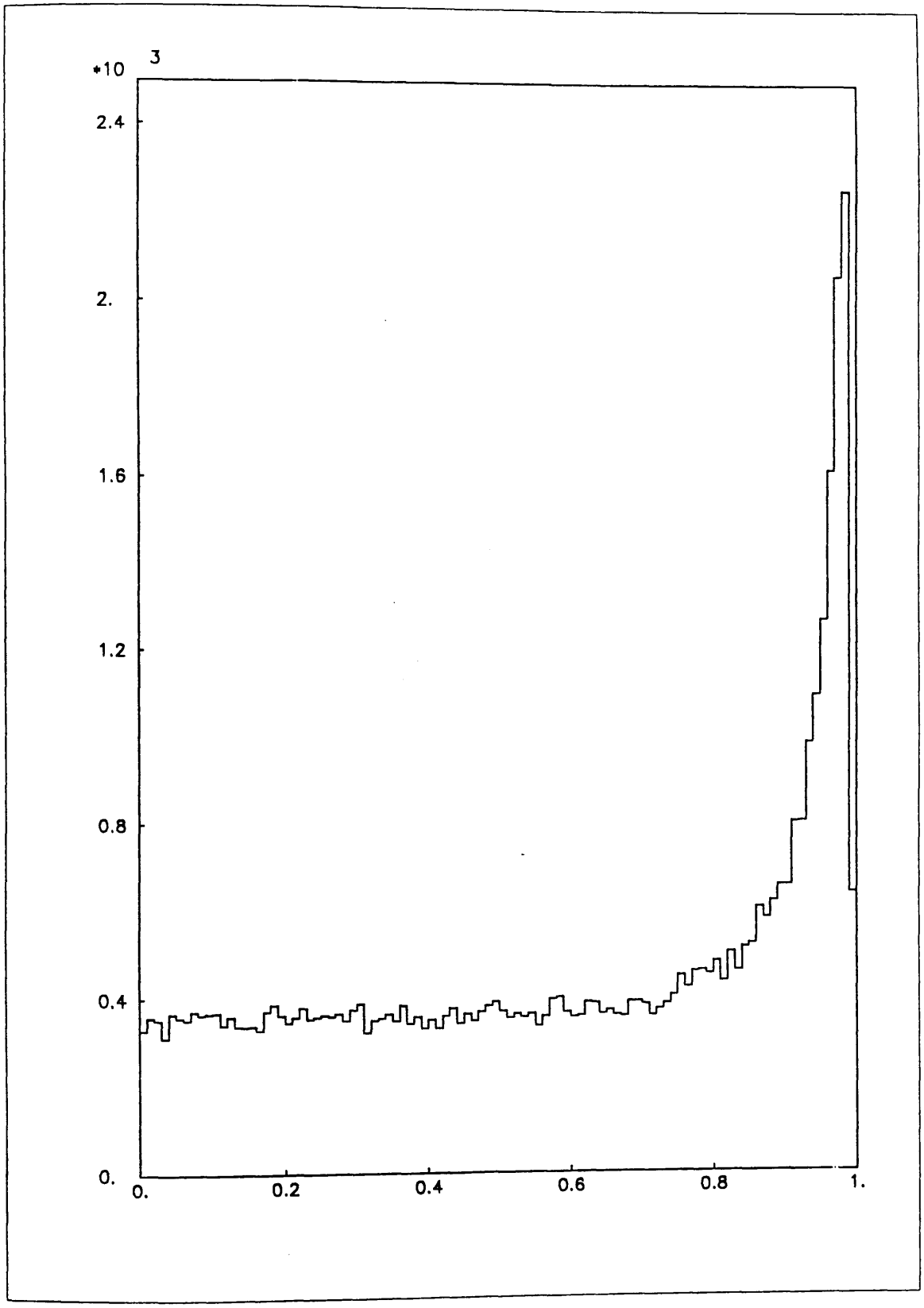

Figure 23: Histogram of γγ pair energy asymmetry

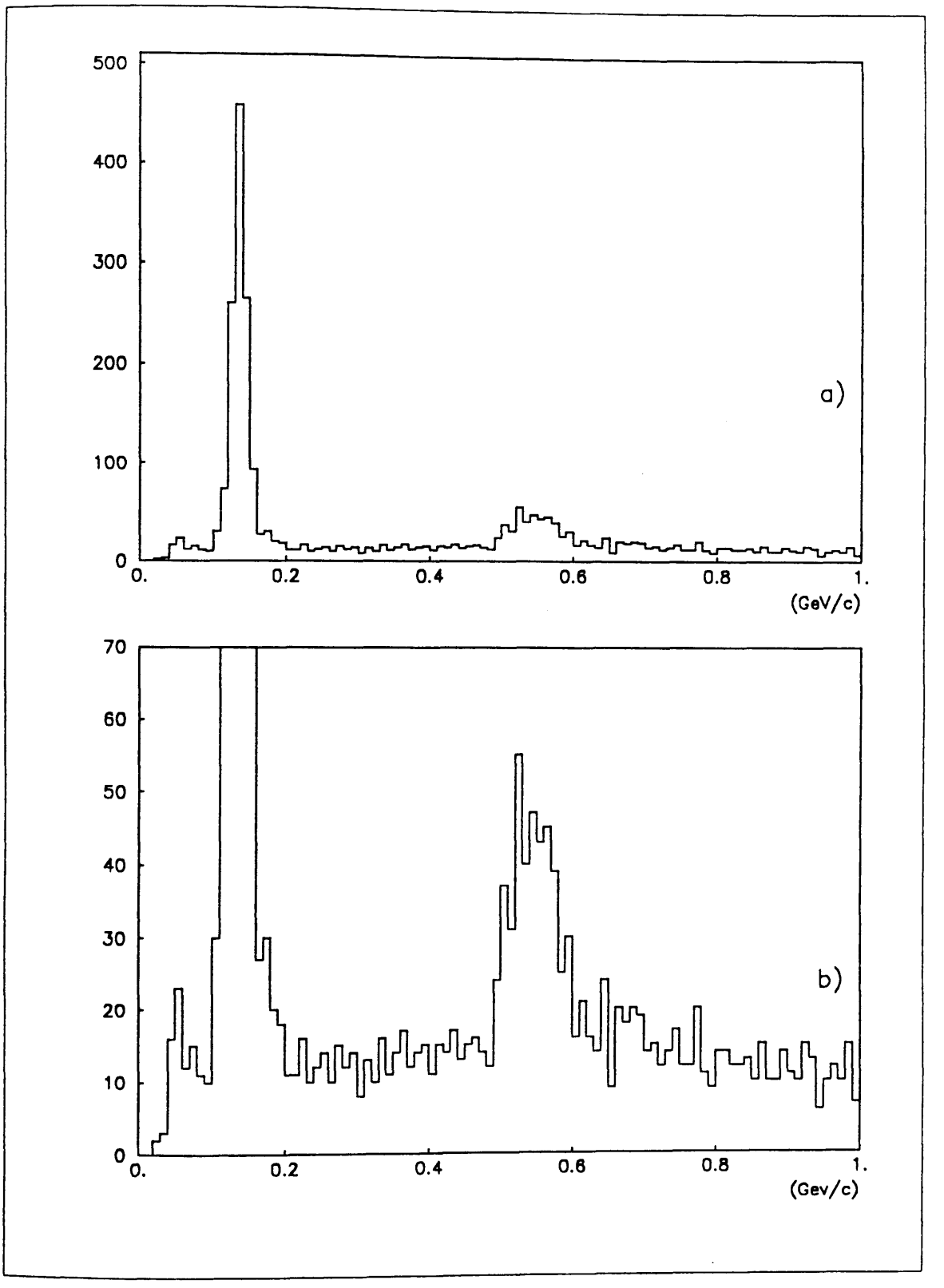

Figure 24: $\gamma\gamma$ invariant mass spectrum

The peaks have a width of a few MeV in both cases, due to the smearing of the mass by the experimental errors. The curves used to fit these components are described below.

i) The π^0 peak.

It was decided to use a combination of a gaussian and a Breit-Wigner curve to fit the π^0 peak, since it was found that neither, on their own, were suitable. This requires 5 parameters – the height and width of each of the contributing curves, and the centre point of the peak (π^0 mass).

ii) The η peak.

A Breit-Wigner curve was fitted, requiring 3 parameters – the height of the peak, its width, and the η mass.

iii) The curve used to fit to the background was:

$$P_1 (x + P_2)^{P_3} e^{-(P_4 x + P_5 x^2)} \quad , \quad x + P_2 > 0$$

where x is the variable on which the fit is being made.

The fitting program did not fit to the parameters described above directly. Instead, they were redefined in terms of more useful parameters. In the case of the curves fitting the π^0 peak, these parameters measured the number of entries under the fitted peak, the fractional contribution of each curve, their widths, and the π^0 mass. The parameters fitting the η peak were redefined in terms of the number of entries under the peak, the width of the peak and the η mass. The background parameters were left as described above. These redefinitions are made so that the fitting program outputs directly both the number of entries under each peak, and the errors on those quantities, these being the two numbers required from the fit.

The result of this stage of the analysis was a table giving the number of π^0 found as a function of P_t and X_f.

6.7 Calculation of the Experimental and Analysis Losses

The number of π^0 found by the analysis program differs from the numbered generated in the target. The causes of the losses are:

- Geometrical losses, for instance, in an event where one or both of the decay gammas from a π^0 misses the calorimeter.
- Trigger losses, where a genuine high P_t π^0 does not cause a trigger.
- The failure of PATREC to correctly reconstruct one or more showers.
- Lack of information on the interaction vertex. Since this is not known, P_t and invariant mass calculations have errors of about 5%.
- Analysis losses, due to genuine π^0 or η particles being rejected by a cut.
- The loss or gain of π^0 at the edges of a P_t or X_f bin, due to errors in the values of those quantities for the reconstructed particle.

The method adopted to find these factors was to repeat the analysis chain with computer generated events for which the high P_t π^0 content was known. The correction factor for each P_t-X_f bin was was then calculated by comparing the number of π^0 found at the end of the chain with the number generated at the beginning.

The steps involved in the Monte Carlo calculation are described below.

i) Monte Carlo generation and decay of the high P_t π^0 :

The P_t and X_f of the π^0 were generated using a distribution parametrisation derived from experimental data [35].

Once generated, the decay of the π^0 was simulated in its own rest frame, and the 4-momenta of the resulting gammas transformed to the laboratory frame.

The number of π^0 generated in each P_t-X_f bin, G_m, was recorded.

ii) Geometrical losses:

The two gammas were tracked to the calorimeter plane. They were both required to land in the same quadrant for their progress to be followed further.

iii) Real event superimposition:

The parameters (energy, hit position, and trajectory) of the Monte Carlo gammas were input into a shower generation routine. This routine simulated a shower developing through the calorimeter, and produced, as output, a set of ADC and TDC signals. (Chapter 2 describes the way in which incident particles generate showers, and how the calorimeter converts these to electronic signals). The shower simulation is made by combining the experimental data with a shower parametrisation [32].

The showers derived from the generated π^0 were suitable for input to the PATREC program. However, for the simulation to be useful, lower energy showers had to be present in the calorimeter, as in real events. This was achieved by superimposing the generated showers onto a real event, read from tape. This was acceptable, since the event did not not need to satisfy principles such as energy or charge conservation, but had only look like a real event in terms of hit distributions, energy distributions, and multiplicities. There was, however, one restriction – the quadrant onto which the decay gammas were superimposed could not already contain a (real) high P_t π^0. There were two reasons for this restriction; the first was that in real events, the high P_t π^0 takes much of the energy of the interaction, and any background showers should therefore have, in general, lower energies than the generated showers. The second point is that the number of high P_t π^0 at the input of the analysis chain had to be known. Since, without the correction factors, the number of real π^0 input cannot be known, all such π^0 must be eliminated from the events used.

This criterion was achieved by only superimposing the generated π^0 on those quadrants where no type 1 or type 2 triggers had occurred (chapter 2). A simple analysis with loose cuts showed that there were no high P_t π^0 in these quadrants.

iv) Trigger cut:

A routine emulating the experiment's trigger was used to decide whether the simulated event would have caused a trigger. If not, it was rejected.

v) PATREC and Analysis:

At this stage, the simulation had emulated the chain of events up to the point where a trigger had occurred, and an event had been written to tape. This event was now fed into the pattern recognition and analysis programs used in the analysis of the real data. The end result, as with the analysis of the real data, was a set of values, F_m, representing the number of high P_t π^0 found in each P_t-X_f bin. Each number had an error, σ_{F_m} associated with it.

vi) Calculation of efficiency factors.

The efficiency factor for a given P_t-X_f bin, E_m, was calculated by dividing the number of π^0 found by the number generated in that bin. The fractional error on this quantity, Δ_{E_m}, is the fractional error on the number found:

$$E_m = F_m/G_m$$

$$\Delta_{E_m} = \sigma_{F_m}/F_m$$

6.8 Calculation of the π^0 and η Production Cross Sections

Sections 6.5 and 6.6 described the method of calculating the number of π^0 found in each P_t-X_f bin. Section 6.7 described the calculation of the efficiency factors in the experimental chain. These factors were used to correct the number of π^0 found, producing a table giving the corrected number of π^0 produced as a function of P_t and X_f. The next step was to convert this to a table of absolute cross sections. The formula used for this calculation was

$$\sigma = \frac{N_f \cdot m_h \cdot I_t \cdot C_l}{CB \quad \rho_h}$$

where N_f is the number of π^0 measured in that bin, CB is the number of beam particles incident on the target, L_t is the length of the target, and C_l is a correction factor (1.07%) for the reduction in beam luminosity through the target, due to other nuclear interactions. ρ_h and m_h are the density of liquid hydrogen, and the mass of the hydrogen atom respectively.

The beam trigger logic has already been described in chapter 2. The trigger logic diagram (figure 5) shows how the quantity CB (clean beam) was derived from the beam counters. The clean beam is the number of beam particles which *could* have caused a trigger during the experiment.

The cross section obtained had to have a three corrections applied:

i) In some cases, events had to be rejected because they overlapped with a second event. The correction factor for this was 1.080 for the positive beam, and 1.065 for the negative beam.

ii) The combined efficiency of the CEDAR counters for pion identification was 75%. The cross sections relating to data from the positive beam were corrected for this loss.

iii) Not all the generated particles (π^0 or η) decay through the $\gamma\gamma$ channel. The cross section calculated must be increased to account for this. These factors are 1.20% in the case of the π^0 and 61.1% in the case of the η [33].

The final step was the calculation of the invariant differential cross section. This is defined as

$$A = E\frac{d^3\sigma}{dp^3}$$

which is equivalent to

$$A = \frac{2E}{\pi E_{cm}} \cdot \frac{1}{P_t} \cdot \frac{d^2\sigma}{dX_f\, dP_t}$$

where E is the energy of a particle in the bin and E_{cm} is the total energy calculated in the centre- of-mass frame. The calculation required an 'average' value of P_t and X_f for each bin. The values used were the weighted averages for each bin, rather than the centre points for the bins. This was necessary since the shape of the P_t and X_f distributions are non-linear. The calculation of the differential term was made as a numeric approximation.

7. RESULTS OF THE π^0 AND η CROSS SECTION DETERMINATION

This chapter presents the results of the analysis described in the previous chapter, and the errors associated with them. It also describes the results of a phenomenological fit to the π^0 and η cross sections.

7.1 Results

Table 4 shows the efficiency factors for the production of π^0. The systematic and statistical errors are given with the table. Table 5 shows the equivalent figures for the η.

Tables 6 and 7 show the invariant cross sections for π^0 production by π^- on p, and for π^+ on p respectively. The tables include the weighted centre points of each bin (section 6.8). Tables 8 and 9 show the same information for the production of η mesons. Figures 25 to 32 show plots of the data as a function of X_f and of P_t. The curves superimposed on these figures are the the results of a phenomenological fit (section 7.3). Figures 33 to 36 show ratios of the absolute cross sections as functions of X_f and of P_t. The ratios of the absolute cross sections summed in P_t and X_f are given in table 10.

7.2 Errors

The tables show the error limits on each cell, with the systematic and statistical contributions given separately (in the upper and lower positions respectively). The sources and magnitudes of the error contributions are:

i) Uncertainties in the results of the efficiency Monte Carlo.

The error contributions from the simulation include both statistical and systematic contributions. The statistical part varies from 2% to to 15%. The systematic part is 5%.

ii) Uncertainties in the number of particles found.

There are two contributions to these errors. The first is the statistical error on the number of π^0 found by the analysis chain; the second is the statistical part of the uncertainty in the Monte Carlo calculation. The two are combined in quadrature and given in the cross section tables.

iii) Uncertainties in the energy calibration.

The systematic errors in the energy calibration of the calorimeter have been calculated [34]. There are two components. The error on the absolute energy scale is 0.6%. This has a large effect on the cross sections, since they vary non-linearly with P_t and X_f (ie with energy). A fit to the data was used to calculate the changes in bin contents due to a change in energy scale. For the π^0, the errors vary between 5.5% at low P_t and X_f, to 11.0% at high P_t and X_f. For the η, the corresponding values are 5.5% and 12.5%.

The second component is due to variations in the calibration error across the calorimeter. For kinematical reasons, different P_t and X_f regions are related to different areas of the calorimeter. The result is that contributions of these errors vary with P_t and X_f, and range between 6.0% and 8.5%.

iv) Uncertainties in the normalisation.

These errors are due to the following:

a) The uncertainty in particle identification by the CEDARs. The error contribution is 2%.

b) The uncertainty in normalisation due to the rejection of overlapping events (section 6.8) contributes 3% to the normalisation error.

7.3 Parametrisation of the Cross Sections

A fit to the data has been made, using the same parametrisation used to generate data in the Monte Carlo simulation (chapter 6). The equation used was

$$E\frac{d^3\sigma}{dp^3} = \frac{A(1 - X_d)^F}{P_t^{2n}}$$

where

$$X_d = \sqrt{[X_t^2 + (X_f - X_0)^2]}$$

and

$$X_t = P_t/\sqrt{s}$$

The results of the fit are given in table 11, and are shown superimposed on plots of the data.

X_f \ P_t	4.00 4.25 4.50	4.50 4.75 5.00	5.00 5.25 5.50	5.50 5.75 6.00	6.00 6.25 6.50
−0.40 −0.30 −0.20	0.014 0.273 0.010	0.015 0.309 0.014	0.017 0.332 0.019	0.019 0.377 0.028	0.016 0.318 0.049
−0.20 −0.15 −0.10	0.019 0.388 0.013	0.020 0.397 0.013	0.018 0.364 0.016	0.018 0.370 0.030	0.018 0.364 0.048
−0.10 −0.05 0.00	0.018 0.367 0.011	0.018 0.359 0.012	0.017 0.346 0.011	0.018 0.351 0.024	0.016 0.313 0.035
0.00 0.05 0.10	0.017 0.339 0.008	0.017 0.332 0.009	0.016 0.326 0.011	0.020 0.408 0.022	0.021 0.422 0.038
0.10 0.15 0.20	0.022 0.440 0.010	0.023 0.464 0.012	0.025 0.502 0.014	0.024 0.485 0.025	0.027 0.548 0.049
0.20 0.25 0.30	0.026 0.525 0.012	0.028 0.552 0.015	0.028 0.565 0.012	0.031 0.627 0.029	0.033 0.670 0.054
0.30 0.35 0.40	0.028 0.569 0.012	0.031 0.622 0.014	0.029 0.586 0.018	0.029 0.580 0.031	0.039 0.770 0.077
0.40 0.50 0.60	0.023 0.461 0.017	0.024 0.475 0.019	0.025 0.508 0.019	0.025 0.490 0.027	0.027 0.539 0.042

The outer cells show the lower bin limit, the bin centre, and the upper bin limit.

The inner cells show the systematic error, the cell value, and the statistical error.

Table 4: Efficiency Factors for π^0 Measurement

X_f \ P_t	4.00 4.25 4.50	4.50 4.75 5.00	5.00 5.25 5.50	5.50 5.75 6.00
−0.40 −0.30 −0.20	0.011 0.212 0.012	0.015 0.304 0.027	0.015 0.300 0.021	0.018 0.359 0.036
−0.20 −0.15 −0.10	0.016 0.321 0.013	0.020 0.394 0.031	0.019 0.378 0.020	0.023 0.455 0.022
−0.10 −0.05 0.00	0.019 0.375 0.007	0.021 0.410 0.026	0.022 0.437 0.021	0.024 0.489 0.034
0.00 0.05 0.10	0.020 0.395 0.012	0.021 0.413 0.021	0.023 0.450 0.017	0.021 0.418 0.031
0.10 0.15 0.20	0.019 0.390 0.013	0.021 0.429 0.031	0.023 0.462 0.016	0.021 0.414 0.035
0.20 0.25 0.30	0.016 0.328 0.020	0.020 0.391 0.023	0.020 0.406 0.016	0.020 0.409 0.033
0.30 0.35 0.40	0.019 0.379 0.017	0.021 0.425 0.026	0.021 0.414 0.022	0.019 0.387 0.037
0.40 0.50 0.60	0.012 0.242 0.013	0.014 0.272 0.029	0.017 0.332 0.019	0.021 0.422 0.041

The outer cells show the lower bin limit, the bin centre, and the upper bin limit.

The inner cells show the systematic error, the cell value, and the statistical error.

Table 5: Efficiency Factors for η Measurement

X_f \ P_t	4.00 – 4.20 – 4.50	4.50 – 4.70 – 5.00	5.00 – 5.19 – 5.50	5.50 – 5.70 – 6.00	6.00 – 6.22 – 6.50
−0.40 – −0.261 – −0.20	21.2 / 198.2 / 12.1	9.9 / 78.9 / 7.1	2.7 / 20.6 / 2.1	0.9 / 6.9 / 1.7	0.2 / 1.4 / 0.8
−0.20 – −0.145 – −0.10	45.6 / 447.0 / 19.4	16.5 / 135.3 / 10.1	4.1 / 33.3 / 5.1	1.8 / 14.4 / 2.5	0.5 / 3.5 / 1.5
−0.10 – −0.050 – 0.00	72.3 / 715.7 / 28.8	22.5 / 187.6 / 14.2	7.2 / 58.8 / 6.7	2.1 / 17.2 / 3.5	0.7 / 5.3 / 2.0
0.00 – 0.051 – 0.10	80.3 / 795.0 / 30.6	30.9 / 257.5 / 15.1	8.5 / 69.5 / 7.3	1.9 / 15.4 / 3.9	0.6 / 4.4 / 1.5
0.10 – 0.150 – 0.20	80.1 / 793.4 / 28.4	27.1 / 226.2 / 12.0	6.7 / 54.1 / 5.3	1.8 / 14.1 / 3.2	0.7 / 5.5 / 1.6
0.20 – 0.246 – 0.30	56.7 / 550.4 / 20.6	21.5 / 176.5 / 10.1	5.7 / 45.8 / 4.9	1.7 / 13.6 / 2.9	0.5 / 3.7 / 1.2
0.30 – 0.345 – 0.40	38.4 / 358.8 / 15.2	11.7 / 92.6 / 6.9	3.1 / 23.9 / 3.5	1.1 / 8.2 / 2.6	0.4 / 3.2 / 1.2
0.40 – 0.460 – 0.60	19.2 / 168.5 / 9.6	5.7 / 43.0 / 6.0	1.5 / 11.2 / 2.7	0.6 / 3.9 / 1.6	0.1 / 0.5 / 0.5

The outer cells show the lower bin limit, the weighted bin centre, and the upper bin limit.

The inner cells show the systematic error, the cell value, and the statistical error.

Table 6: $Ed^3\sigma/dp^3$ (π^- p − > π^0 X) (pbarn GeV^{-2})

X_f \ P_t	4.00 4.20 4.50	4.50 4.70 5.00	5.00 5.19 5.50	5.50 5.70 6.00	6.00 6.22 6.50
−0.40	19.8	8.8	1.8	0.3	0.1
−0.261	182.0	68.6	13.8	2.4	0.7
−0.20	16.9	8.6	3.4	1.2	1.4
−0.20	45.7	14.7	3.3	1.3	0.5
−0.145	439.2	119.6	26.2	10.3	3.5
−0.10	23.1	14.4	7.9	3.5	2.4
−0.10	60.5	17.2	5.4	1.5	0.2
−0.050	587.2	140.6	43.2	11.6	1.3
0.00	31.5	13.5	8.2	4.1	2.6
0.00	77.4	25.3	5.8	2.5	0.3
0.051	758.7	209.2	46.6	20.0	1.9
0.10	35.8	17.6	8.9	4.6	1.9
0.10	67.2	24.9	5.7	2.3	0.5
0.150	652.5	204.4	45.8	18.4	3.9
0.20	54.6	15.5	7.2	4.0	1.6
0.20	55.3	18.8	4.9	1.3	0.1
0.246	526.9	151.3	38.4	10.1	0.7
0.30	26.6	12.4	3.9	2.9	1.3
0.30	33.0	12.2	2.8	0.8	0.1
0.345	302.4	95.4	21.2	6.0	0.6
0.40	18.6	9.0	5.5	2.6	1.3
0.40	15.7	4.0	1.4	0.2	0.1
0.460	133.9	29.5	10.3	1.7	0.5
0.60	11.9	4.6	2.3	1.1	1.0

The outer cells show the lower bin limit, the weighted bin centre, and the upper bin limit.

The inner cells show the systematic error, the cell value, and the statistical error.

Table 7: $Ed^3\sigma/dp^3$ ($\pi^+ p -> \pi^0 X$) (pbarn GeV^{-2})

X_f \ P_t	4.00 4.20 4.50	4.50 4.70 5.00	5.00 5.19 5.50	5.50 5.70 6.00
−0.40	3.9	1.5	1.0	0.4
−0.267	35.7	11.4	7.1	2.5
−0.20	13.1	7.7	2.7	1.7
−0.20	39.7	5.2	1.9	1.0
−0.146	385.0	41.7	14.7	7.2
−0.10	64.4	11.5	6.0	2.9
−0.10	34.6	6.2	4.4	1.3
−0.048	342.5	51.3	35.1	9.7
0.00	32.6	15.3	11.8	3.3
0.00	43.9	11.8	4.0	1.6
0.050	439.0	97.9	32.0	12.7
0.10	55.0	24.6	11.0	4.5
0.10	52.0	14.6	4.9	1.7
0.147	510.1	119.7	39.6	13.3
0.20	59.2	19.0	11.9	4.6
0.20	26.4	5.9	2.3	1.2
0.245	251.9	46.8	17.7	8.6
0.30	48.4	13.9	10.6	3.5
0.30	17.8	3.7	0.9	0.2
0.347	161.9	28.4	6.4	1.6
0.40	37.2	12.6	6.4	3.3
0.40	4.6	2.6	0.2	0.1
0.457	38.0	18.6	1.1	0.9
0.60	17.0	9.7	2.3	1.7

The outer cells show the lower bin limit, the weighted bin centre, and the upper bin limit.

The inner cells show the systematic error, the cell value, and the statistical error.

Table 8: $Ed^3\sigma/dp^3$ ($\pi^- p -> \eta X$) (pbarn GeV^{-2})

X_f \ P_t	4.00 4.20 4.50	4.50 4.70 5.00	5.00 5.19 5.50	5.50 5.70 6.00
−0.40 −0.267 −0.20	12.1 112.3 40.4	4.5 35.5 18.1	1.5 12.0 5.0	0.7 4.9 3.3
−0.20 −0.146 −0.10	29.5 283.8 29.9	8.6 69.8 16.2	3.2 25.9 8.7	0.6 4.7 4.7
−0.10 −0.048 0.00	37.7 369.7 44.7	9.2 76.4 20.0	2.9 23.8 7.2	0.3 2.1 4.2
0.00 0.050 0.10	39.5 387.0 58.2	14.3 118.5 25.6	4.3 34.7 8.9	1.6 12.4 5.1
0.10 0.147 0.20	33.4 324.3 50.8	16.1 132.2 27.2	2.9 23.5 5.0	1.0 7.8 5.2
0.20 0.245 0.30	22.1 210.7 43.9	9.0 72.8 21.4	2.6 20.3 5.9	0.4 2.8 5.7
0.30 0.347 0.40	19.6 180.2 47.1	2.4 19.1 9.7	0.4 3.2 6.3	0.4 3.2 6.5
0.40 0.457 0.60	10.3 86.9 31.6	3.5 25.7 13.1	0.6 4.4 4.4	0.2 1.7 3.3

The outer cells show the lower bin limit, the weighted bin centre, and the upper bin limit.

The inner cells show the systematic error, the cell value, and the statistical error.

Table 9: $Ed^3\sigma/dp^3$ $(\pi^+ p -> \eta X)$ (pbarn GeV^{-2})

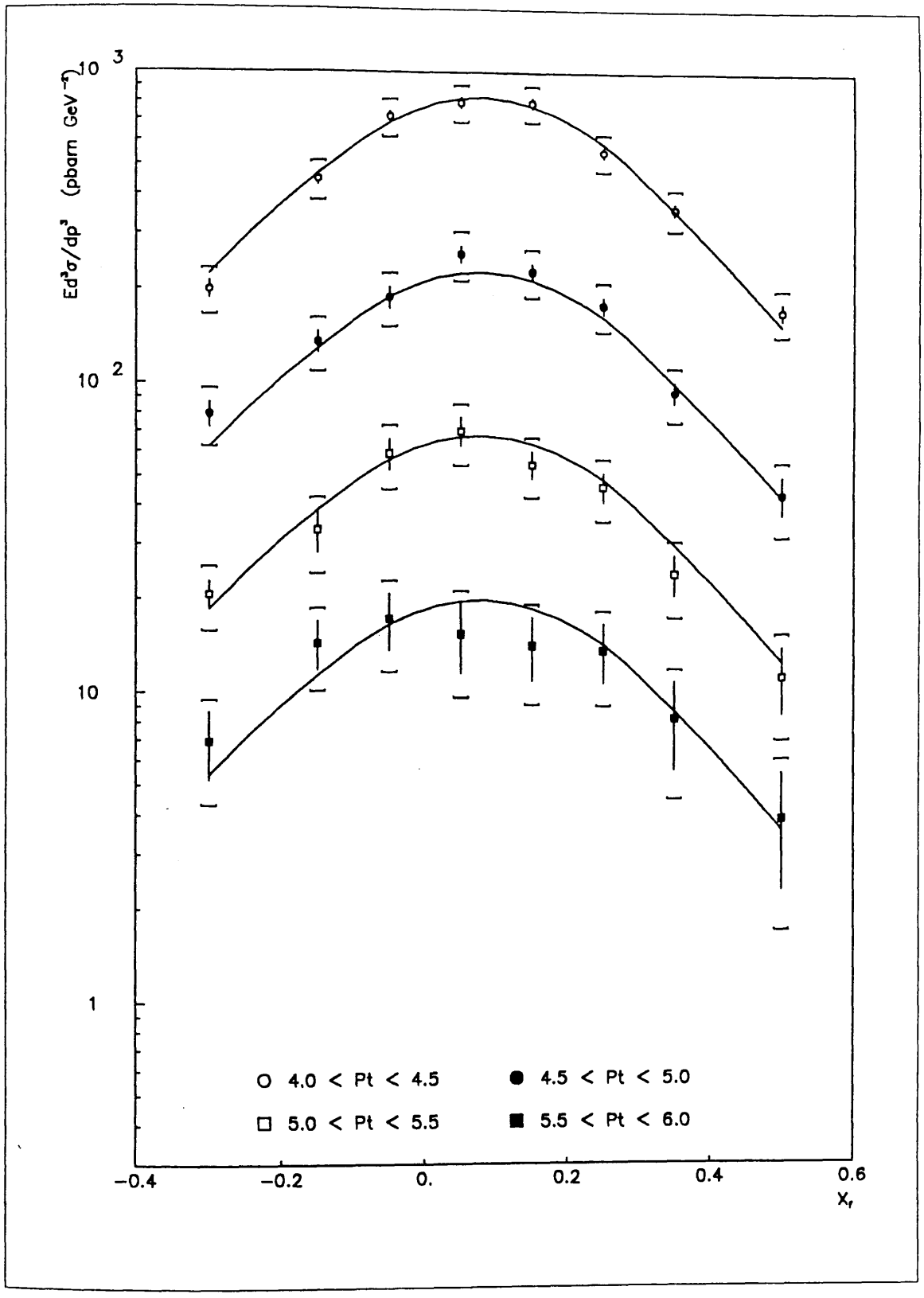

Figure 25: $Ed^3\sigma/dp^3$ $(\pi^- p -> \pi^0 X)$ as a function of X_f

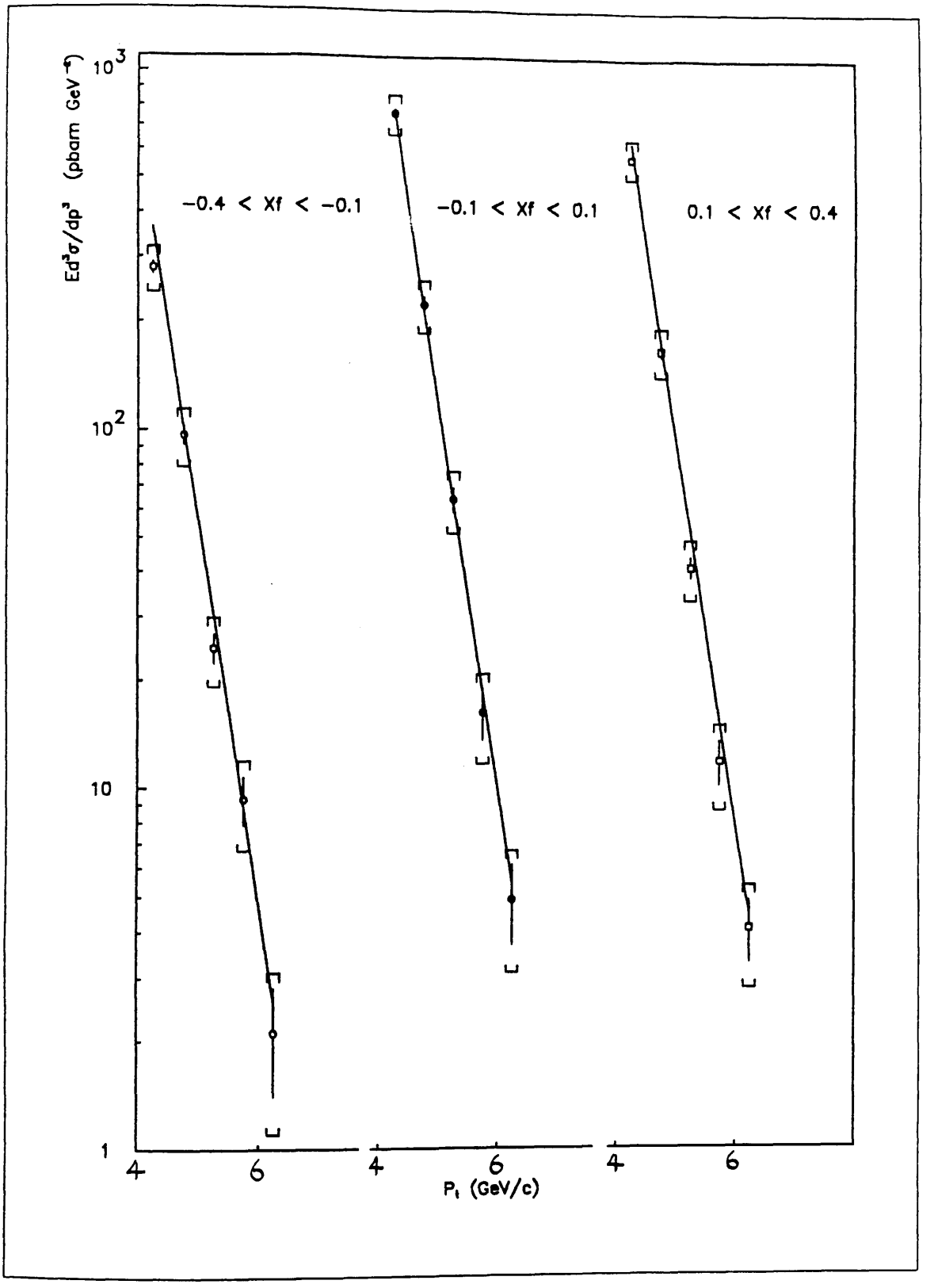

Figure 26: $Ed^3\sigma/dp^3$ ($\pi^- p -> \pi^0 X$) as a function of P_t

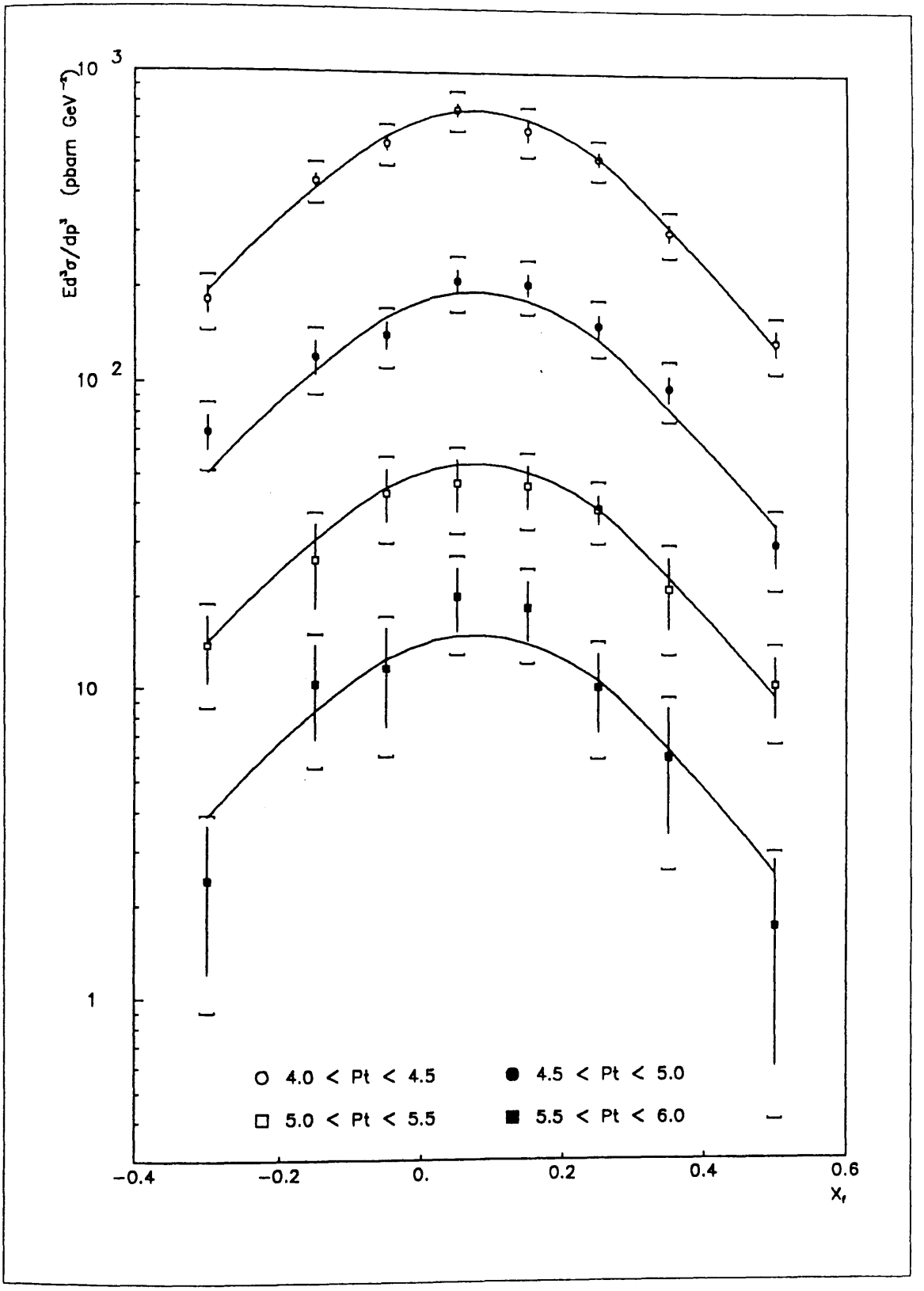

Figure 27: $Ed^3\sigma/dp^3$ $(\pi^+ p -> \pi^0 X)$ as a function of X_f

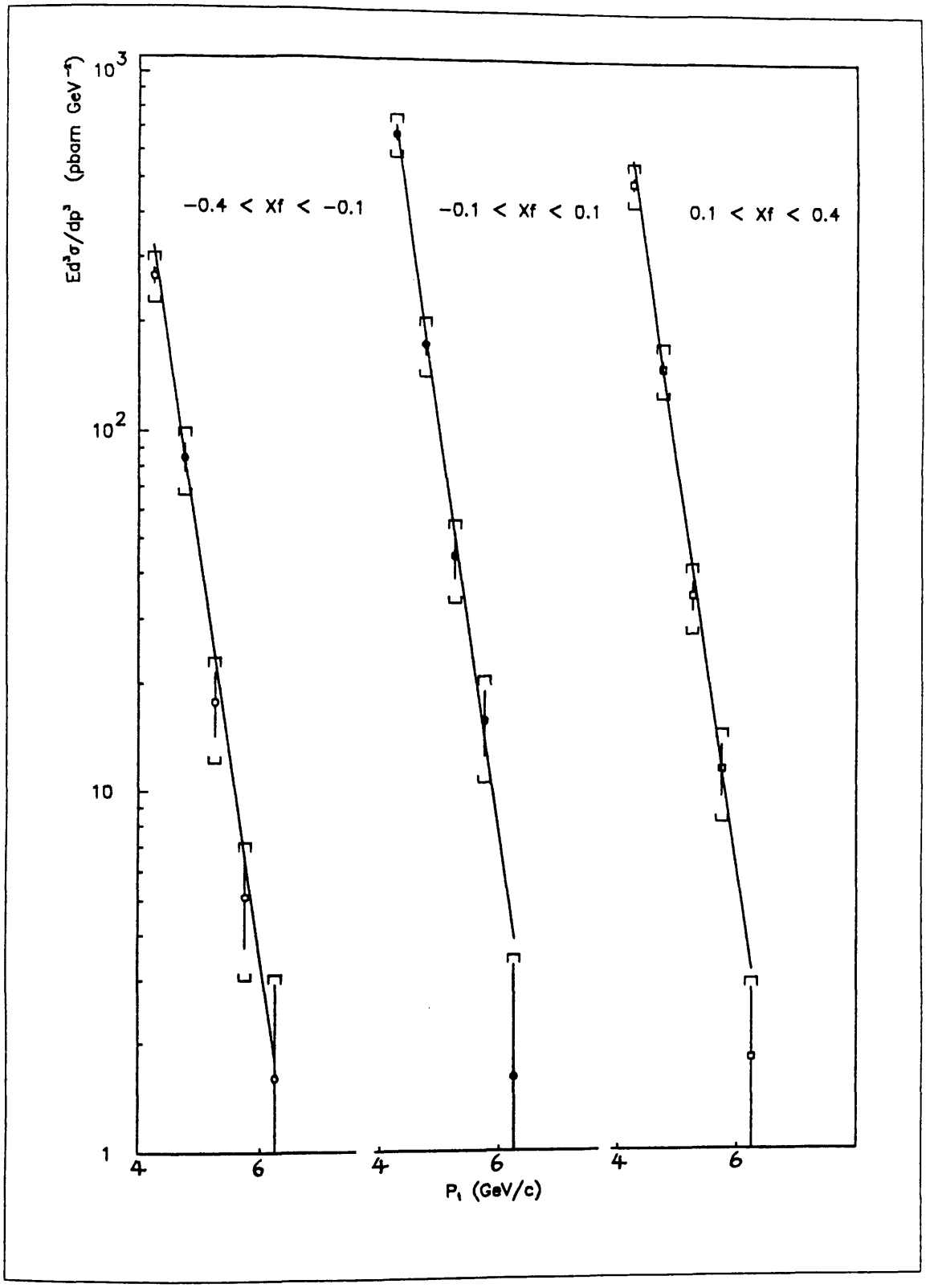

Figure 28: $Ed^3\sigma/dp^3$ $(\pi^+ p -> \pi^0 X)$ as a function of P_t

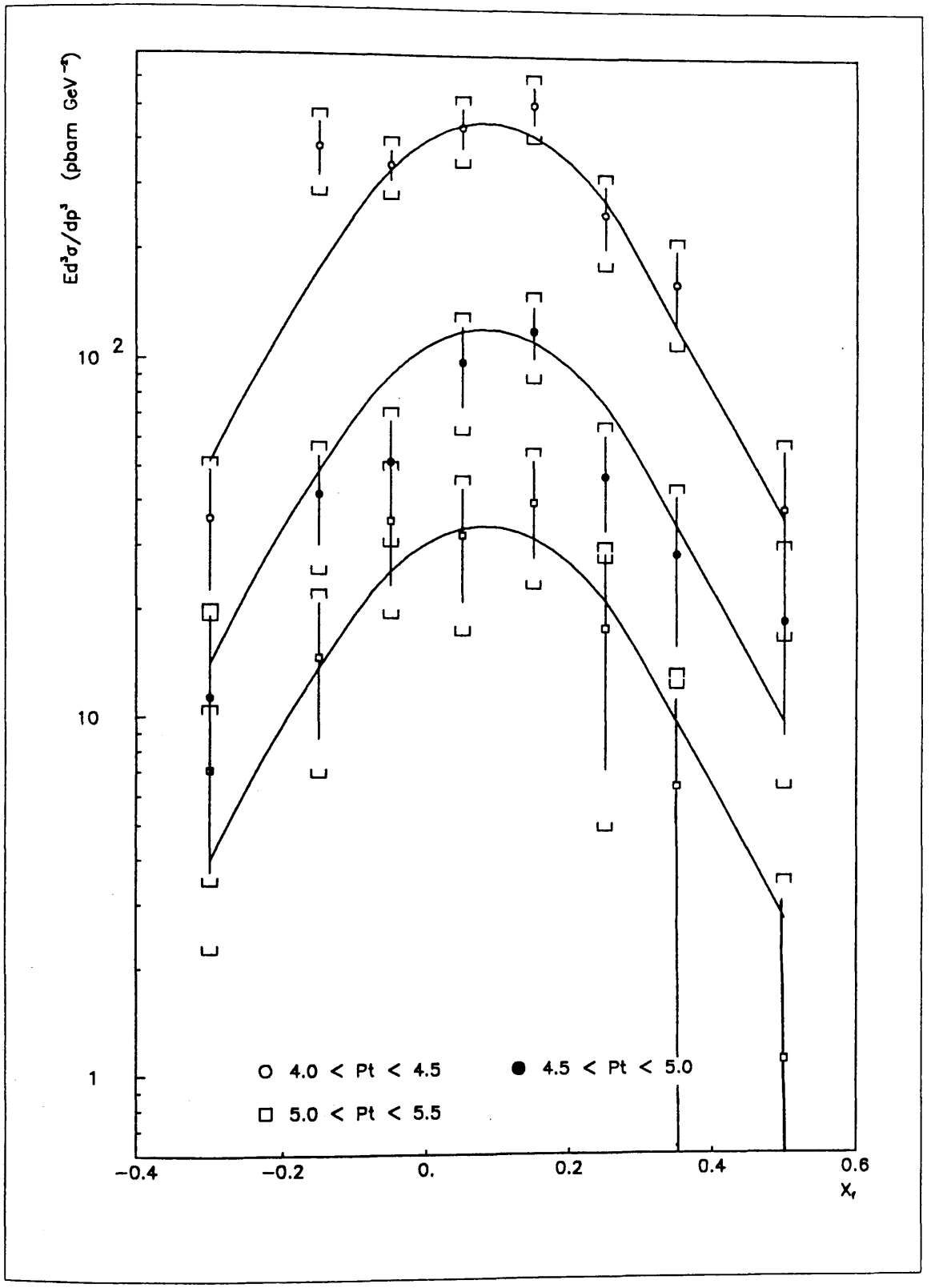

Figure 29: $Ed^3\sigma/dp^3$ $(\pi^- p -> \eta X)$ as a function of X_f

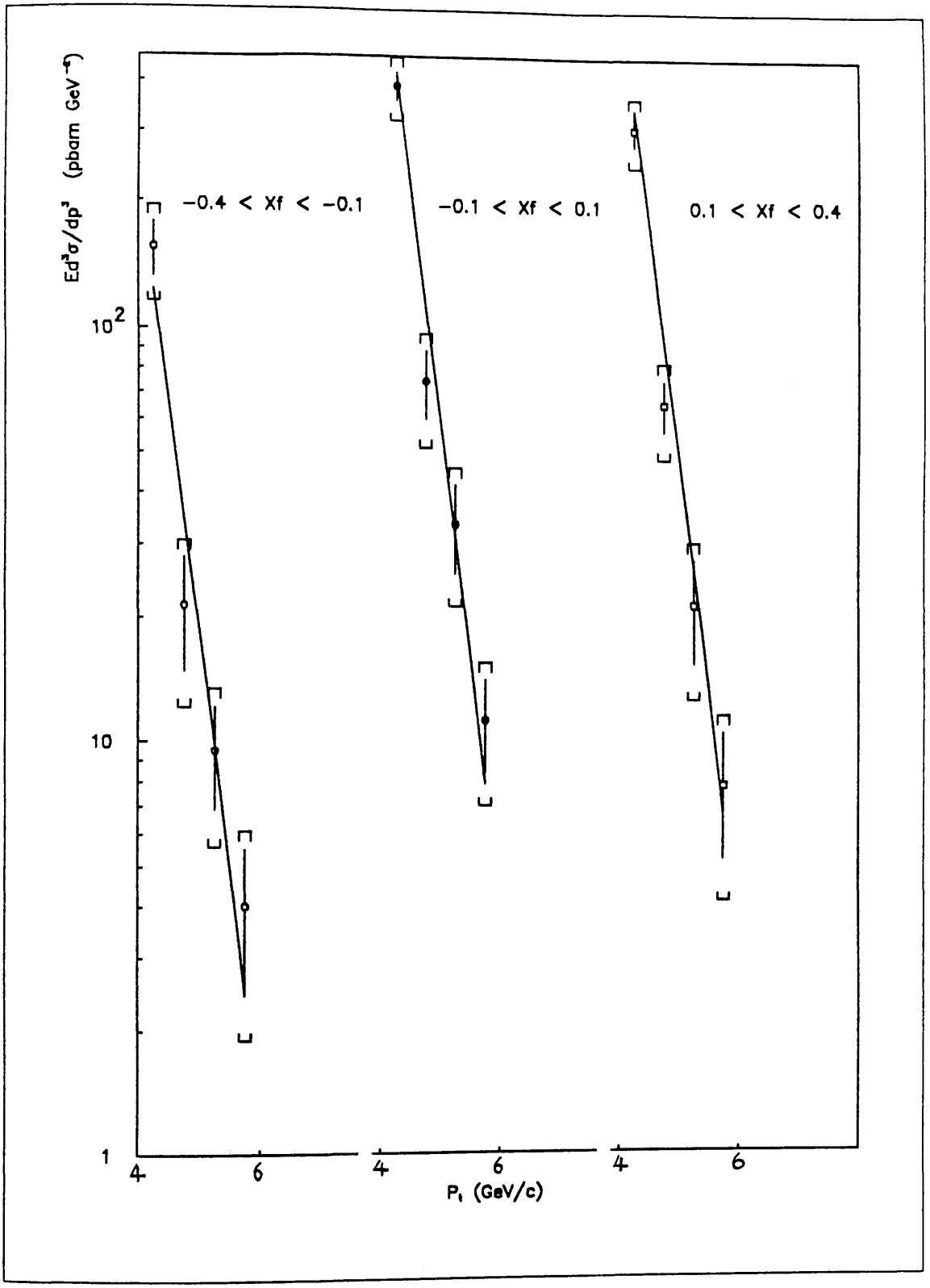

Figure 30: $Ed^3\sigma/dp^3$ $(\pi^- p -> \eta X)$ as a function of P_t

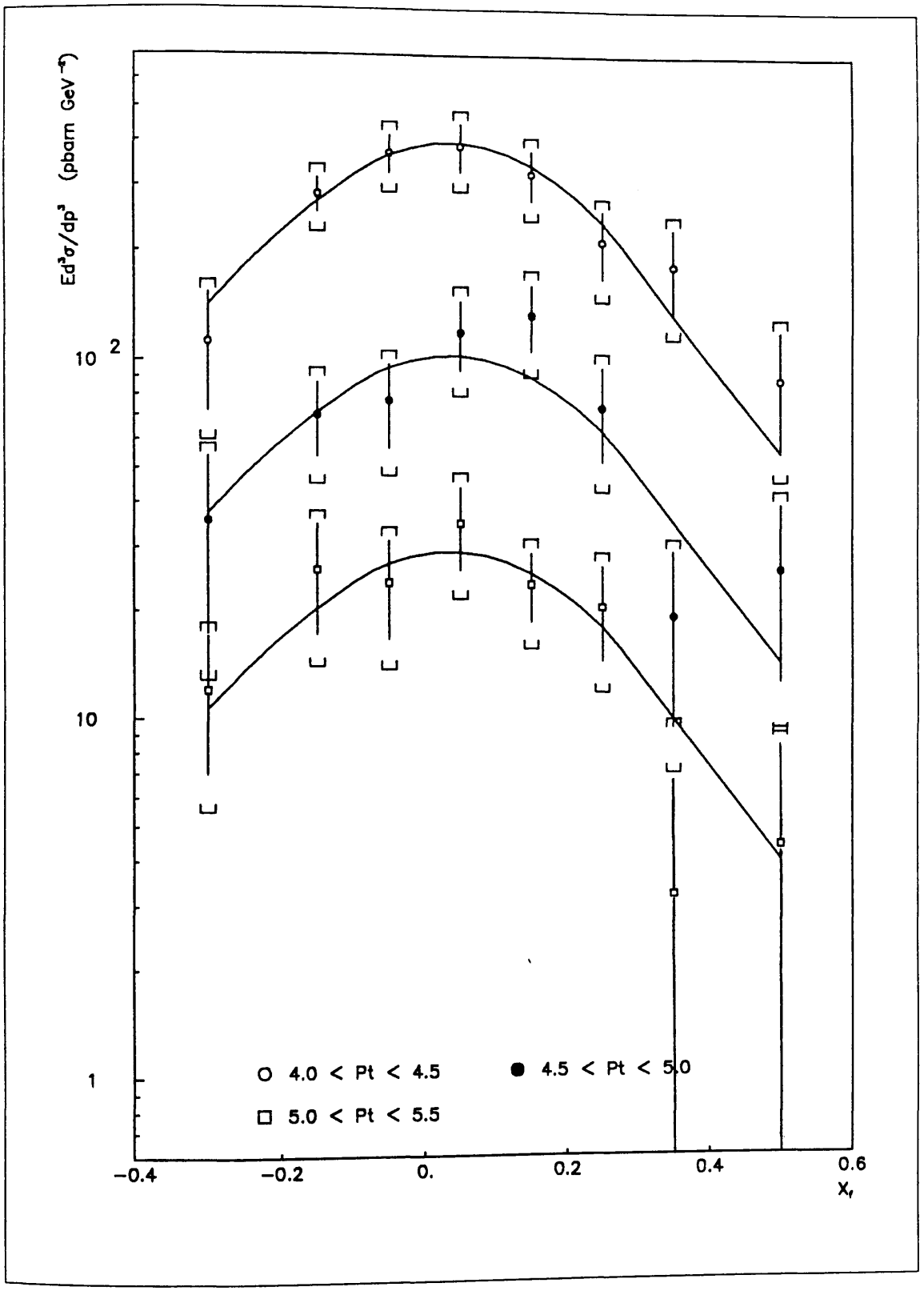

Figure 31: $Ed^3\sigma/dp^3$ $(\pi^+ p -> \eta X)$ as a function of X_f

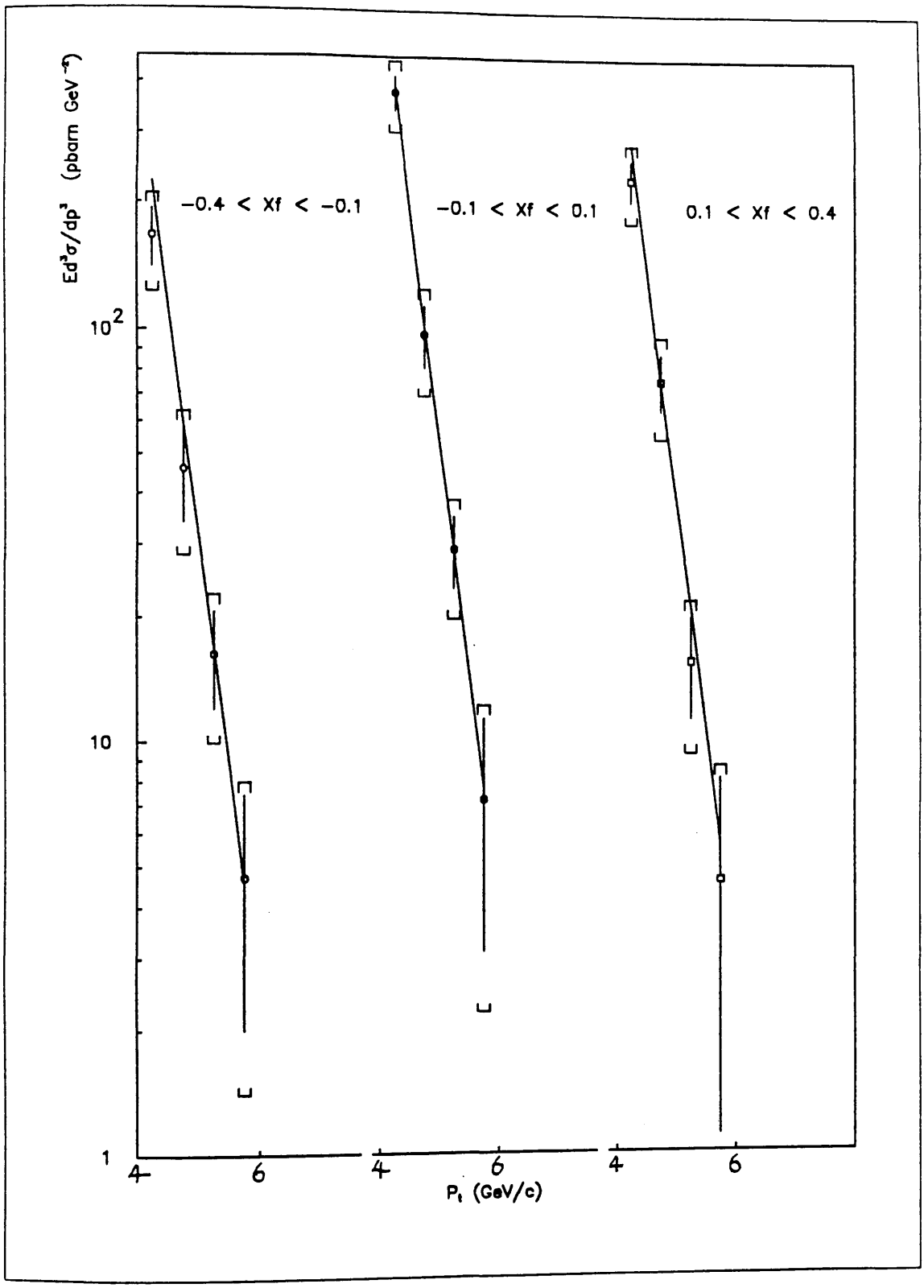

Figure 32: $Ed^3\sigma/dp^3$ $(\pi^+ p -> \eta X)$ as a function of P_t

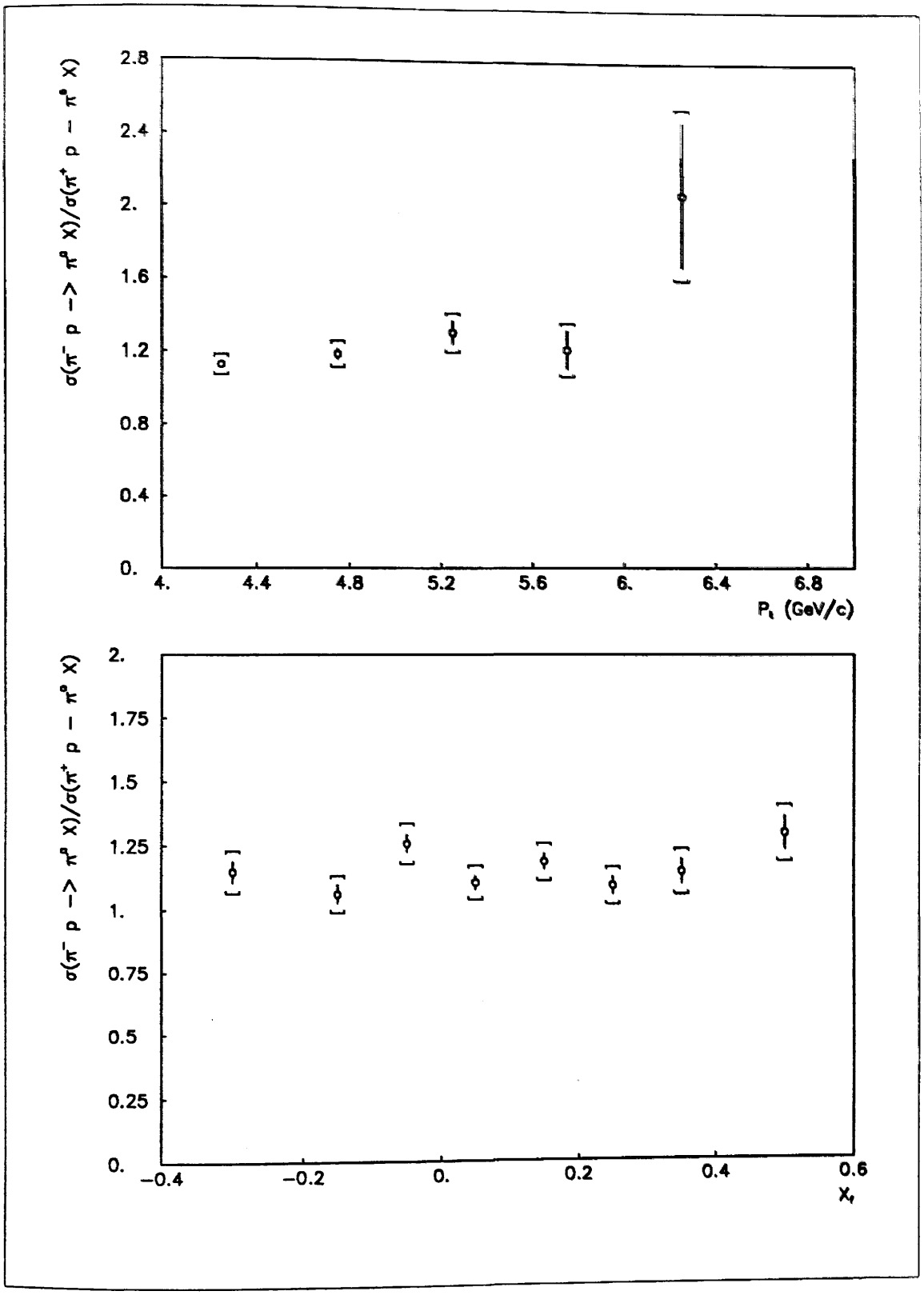

Figure 33: $\sigma(\pi^- p -> \pi^0 X)/\sigma(\pi^+ p -> \pi^0 X)$ *as a function of (a)* P_t *(b)* X_f

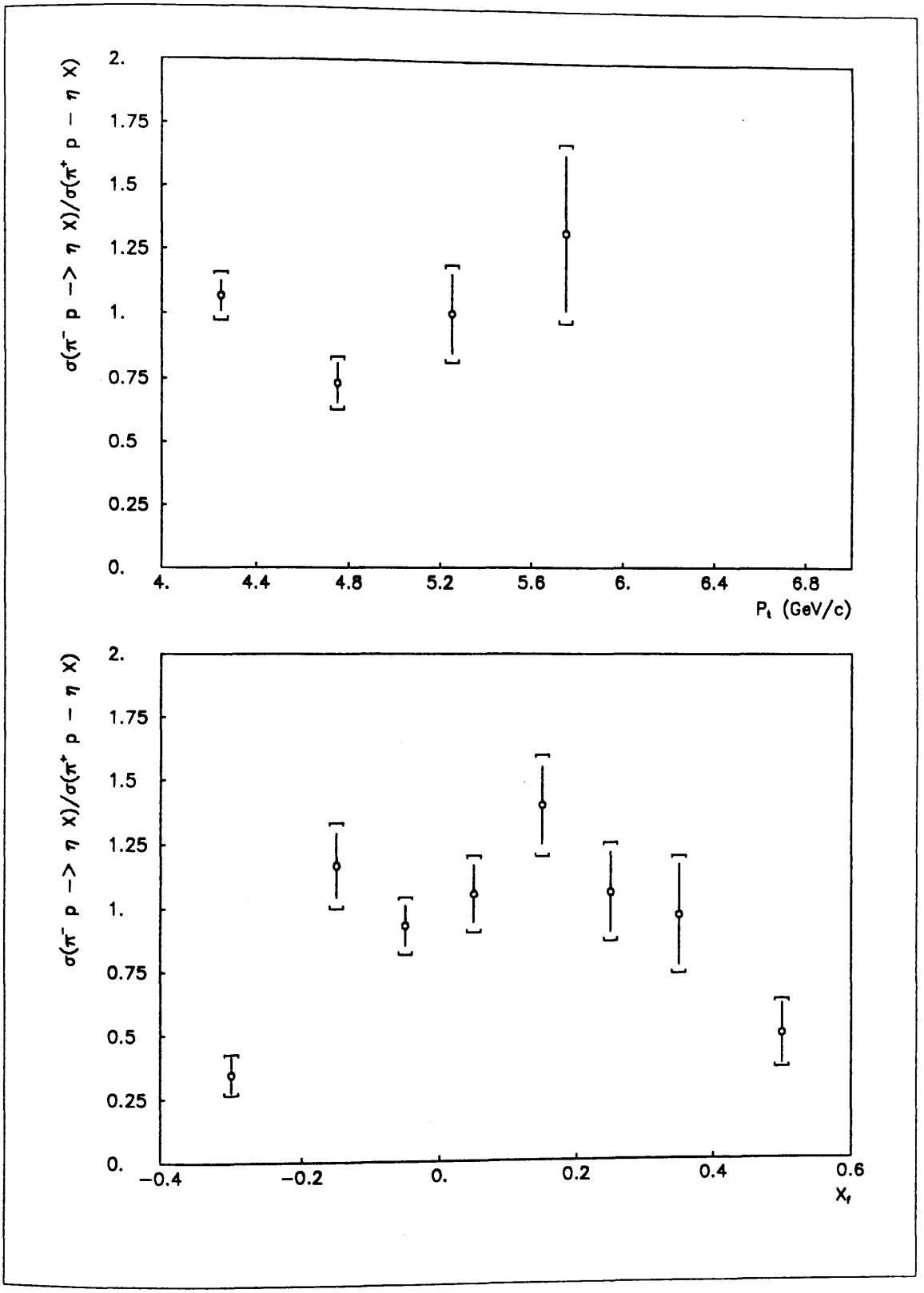

Figure 34: $\sigma(\pi^- p -> \eta X)/\sigma(\pi^+ p -> \eta X)$ as a function of (a) P_t (b) X_f

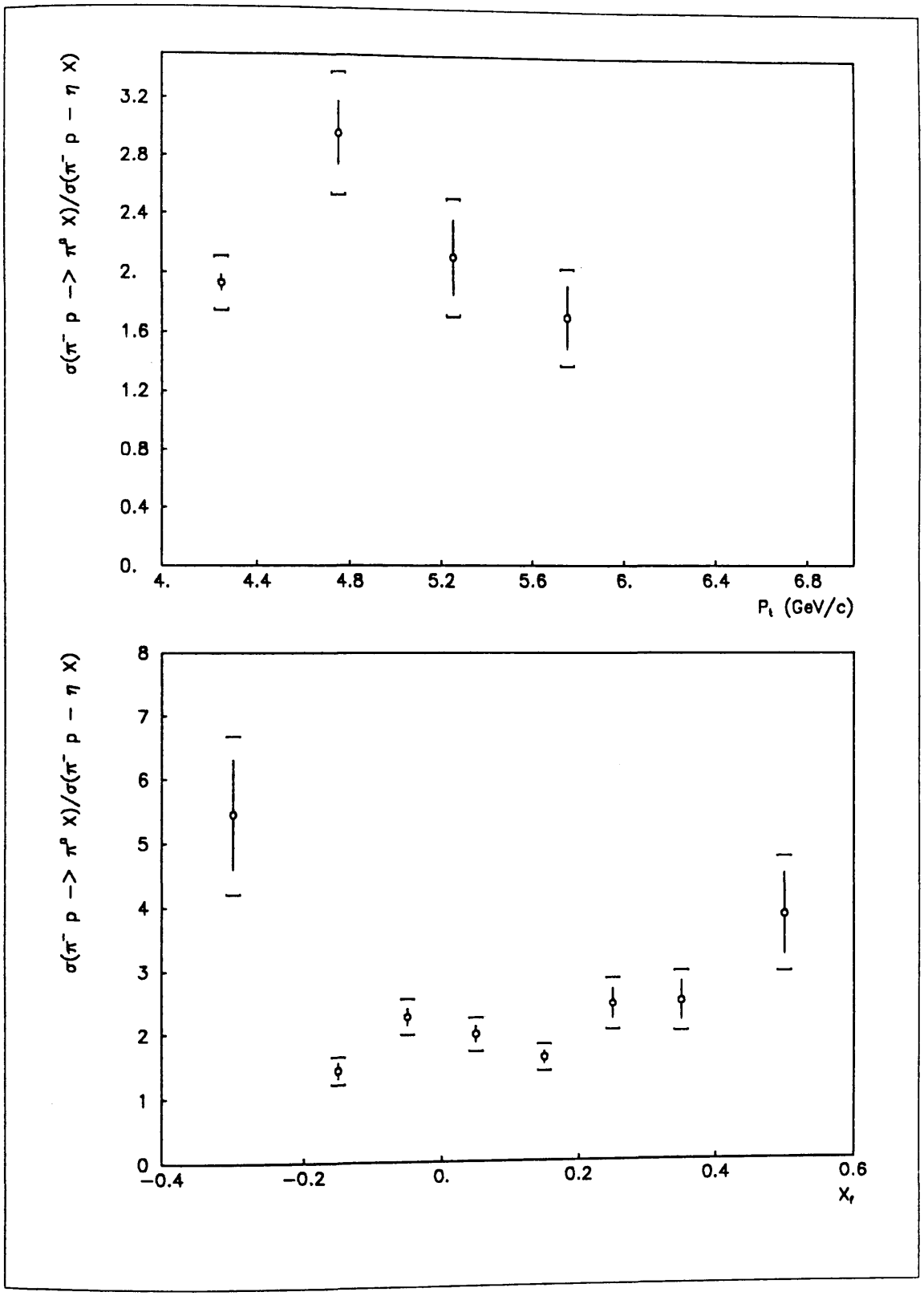

Figure 35: $\sigma(\pi^- p -> \pi^0 X)/\sigma(\pi^- p -> \eta X)$ as a function of (a) P_t (b) X_f

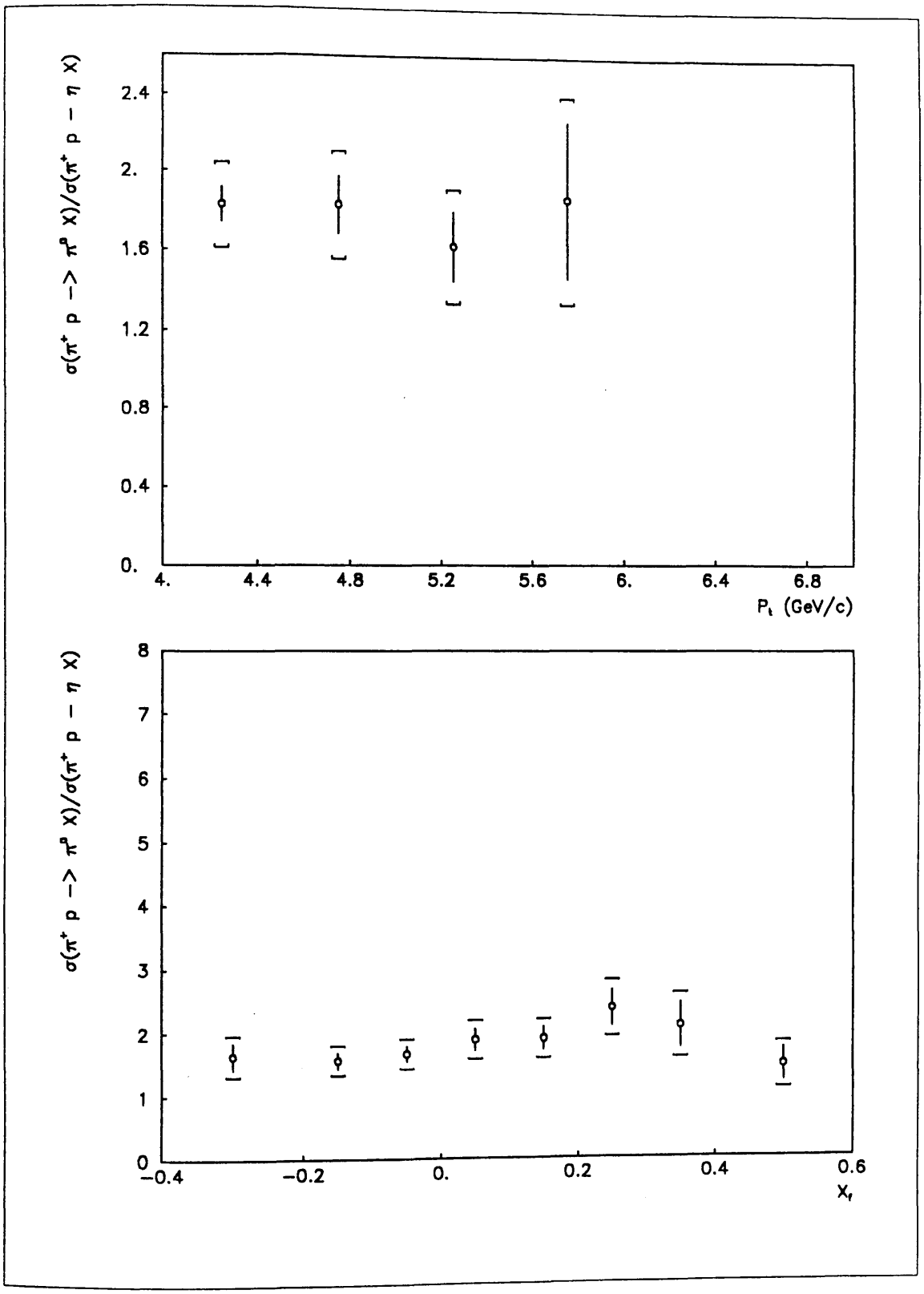

Figure 36: $\sigma(\pi^+ p -> \pi^0 X)/\sigma(\pi^+ p -> \eta X)$ *as a function of (a)* P_t *(b)* X_f

$\sigma(\pi^- p -> \pi^0 X)/\sigma(\pi^+ p -> \pi^0 X)$	$1.15 \pm 0.013 \pm 0.041$
$\sigma(\pi^- p -> \eta X)/\sigma(\pi^+ p -> \eta X)$	$1.00 \pm 0.024 \pm 0.036$
$\sigma(\pi^- p -> \pi^0 X)/\sigma(\pi^- p -> \eta X)$	$2.09 \pm 0.049 \pm 0.148$
$\sigma(\pi^+ p -> \pi^0 X)/\sigma(\pi^+ p -> \eta X)$	$1.82 \pm 0.077 \pm 0.129$

Table 10: Ratio of total cross sections

Process	A (mb GeV^{-2})	F	n	X_0
$\pi^- p -> \pi^0 X$:	0.99 ± 0.12	5.65 ± 0.11	3.98 ± 0.039	0.076 ± 0.0023
$\pi^+ p -> \pi^0 X$:	1.91 ± 0.33	5.88 ± 0.14	4.20 ± 0.091	0.076 ± 0.0053
$\pi^- p -> \eta X$:	0.17 ± 0.042	8.81 ± 0.37	3.07 ± 0.032	0.08 ± 0.008
$\pi^+ p -> \eta X$:	1.04 ± 0.27	5.48 ± 0.33	4.28 ± 0.052	0.035 ± 0.015

Table 11: Results of phenomenological fit

8. CONCLUSIONS

Measurements have been made on the cross section for the inclusive production of π^0 and η mesons from π^- and π^+ beams incident on a hydrogen target, at an energy of 280 GeV. The measurements cover the ranges -0.4 to 0.6 in X_f, and 4.0 to 6.5 GeV/c in P_t.

The production ratios

$$\sigma(\pi^- p -> \pi^0 X)/\sigma(\pi^+ p -> \pi^0 X)$$

$$\sigma(\pi^- p -> \eta X)/\sigma(\pi^+ p -> \eta X)$$

$$\sigma(\pi^- p -> \pi^0 X)/\sigma(\pi^- p -> \eta X)$$

$$\sigma(\pi^+ p -> \pi^0 X)/\sigma(\pi^+ p -> \eta X)$$

are consistent (within the error limits) with flat distributions over the P_t range measured, and over the central X_f region. That is, the shape of the production cross sections appears to be consistent in all cases, and only the absolute scales differ (table 10 gives the relative scales). There is, however, an indication that the production of ηs by π^+ falls of at high $|X_f|$, relative to η production by π^-.

The production of π^0s from π^- is higher than from π^+ (by 15%), whilst each produce the same number of ηs. The ratio for the production of π^0s to ηs is again higher for π^- than for π^+, although within the errors they are consistent. Previous experiments ([16] [21] [24]), all at P_t of less than 4 GeV/c, obtain similar results for the ratio of π^0 to η production. The ratios given in references 16 and 21 are consistent with the data presented here, although they are at higher energy (centre of mass energies of 53 GeV and 63 GeV, compared with 23 GeV in WA70) and for pp and $\bar{p}p$ interactions respectively. The data in reference 24 is consistent at the two standard deviation level only (0.35 ± 0.6).

The equation used to fit the data is similar to that used in a previous experiments ([35] [20]). The equation for the fit is consistent with the data, in that a good χ^2 can be obtained with the fit.

The cross sections have been compared with three previous experiments ([35] [20] [23]) although only the last of these is in a similar kinematic region to WA70. The data in reference 35 was taken at a beam energies of 100 and 200 GeV, in the range 1 GeV/c < P_t < 5 GeV/c, whilst the data from reference 20 was taken at 200 GeV, using hadrons incident on a carbon target. The results of the *fits* to the data for these experiments, extrapolated to the WA70 kinematic region, are not consistent with the cross section derived here, even allowing for the errors in both. In particular, for π^0 production, the overall normalisation is higher for the data from the two references. In addition, the cross sections given by the fits behave differently as a function of P_t and X_f. Figure 37 shows these fits, as functions of X_f and P_t, superimposed on the cross section for π^- p $->$ π^0 X derived here.

When comparing the P_t and X_f regions in which the data from these two experiments overlap the WA70 data, it is found that the data points are consistent within the errors. It must be stressed, however, that for each experiment, only three data points fall within this overlap region.

The NA24 experiment at CERN [23] took data for π^- and π^+ incident on protons at a beam energy of 300 GeV, over the same P_t region as the data presented here. The cross sections are compatible, within the errors, for both π^- and π^+ data. Figure 38 shows the data from NA24 and WA70, as a function of P_t.

In summary, the π^0 cross sections derived here are consistent with previous experiments. The overall ratio of η to π^0 production also agrees with previously measured values. The η production cross sections themselves are new.

The WA70 source calibration system has been used to correct the data taken with the calorimeter. The data initially had systematic effects of up to 25% across the width of the calorimeter, with local fluctuations of up to 10%. Analysis of both hadron-hadron interaction data, and electron beam scan data, have shown that the source corrections reduce these systematic errors to less than 2%, and the local fluctuations to 5%.

The major drawback of the system is the time taken to make a complete calibration (approximately 36 hours). This limited its use to the start and end of the experiment, and to the three day intervals between beam periods. However, it has been shown that calibration runs made weeks apart are consistent. The laser system has been shown to be capable of performing quick scans (20 minutes) to record short term variations in the calibration. The source system, combined with this secondary system, therefore provides an effective method of calibrating the calorimeter.

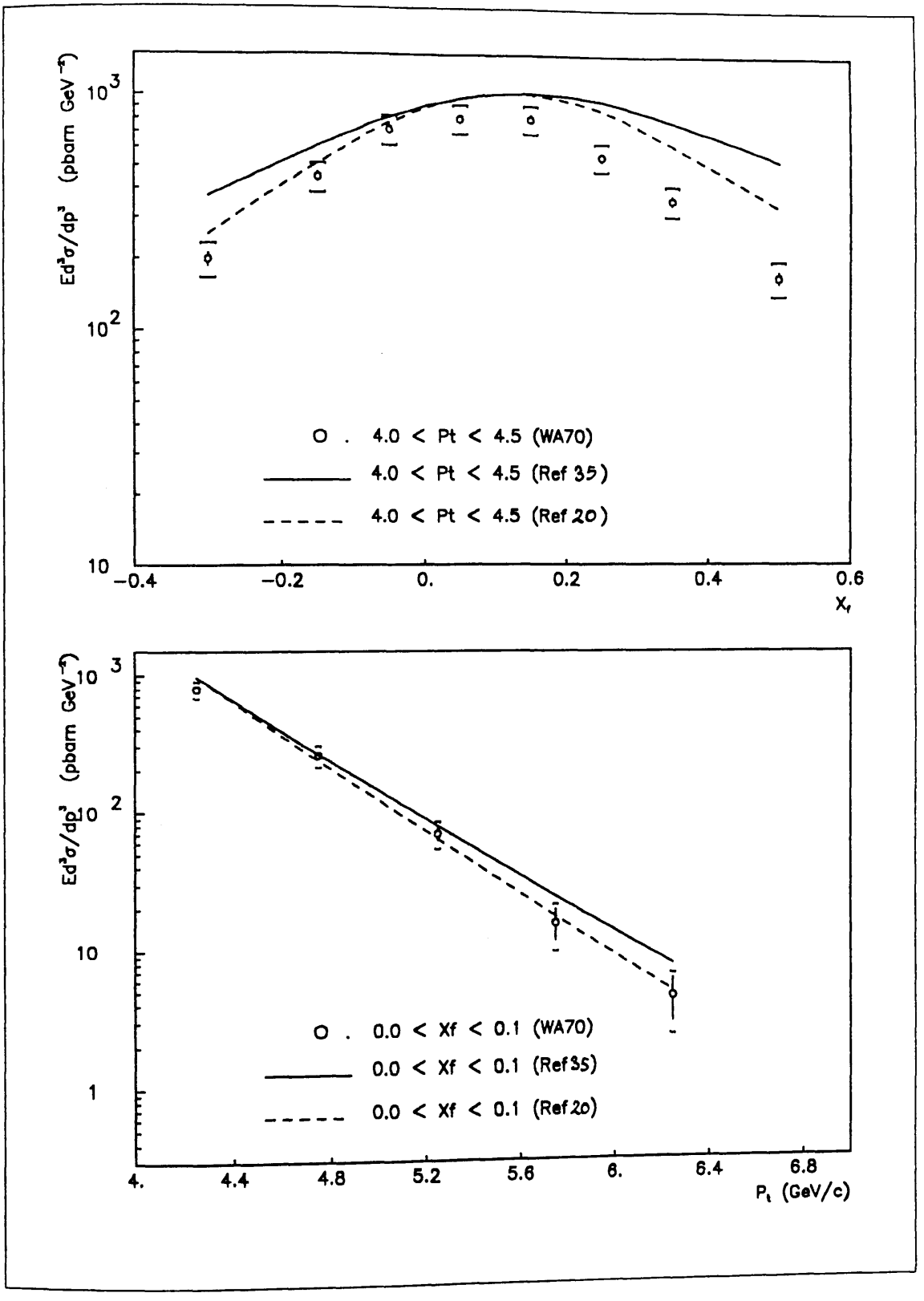

Figure 37: $Ed^3\sigma/dp^3$ ($\pi^- p -> \pi^0 X$) with fits from Refs. 35 and 20 superimposed

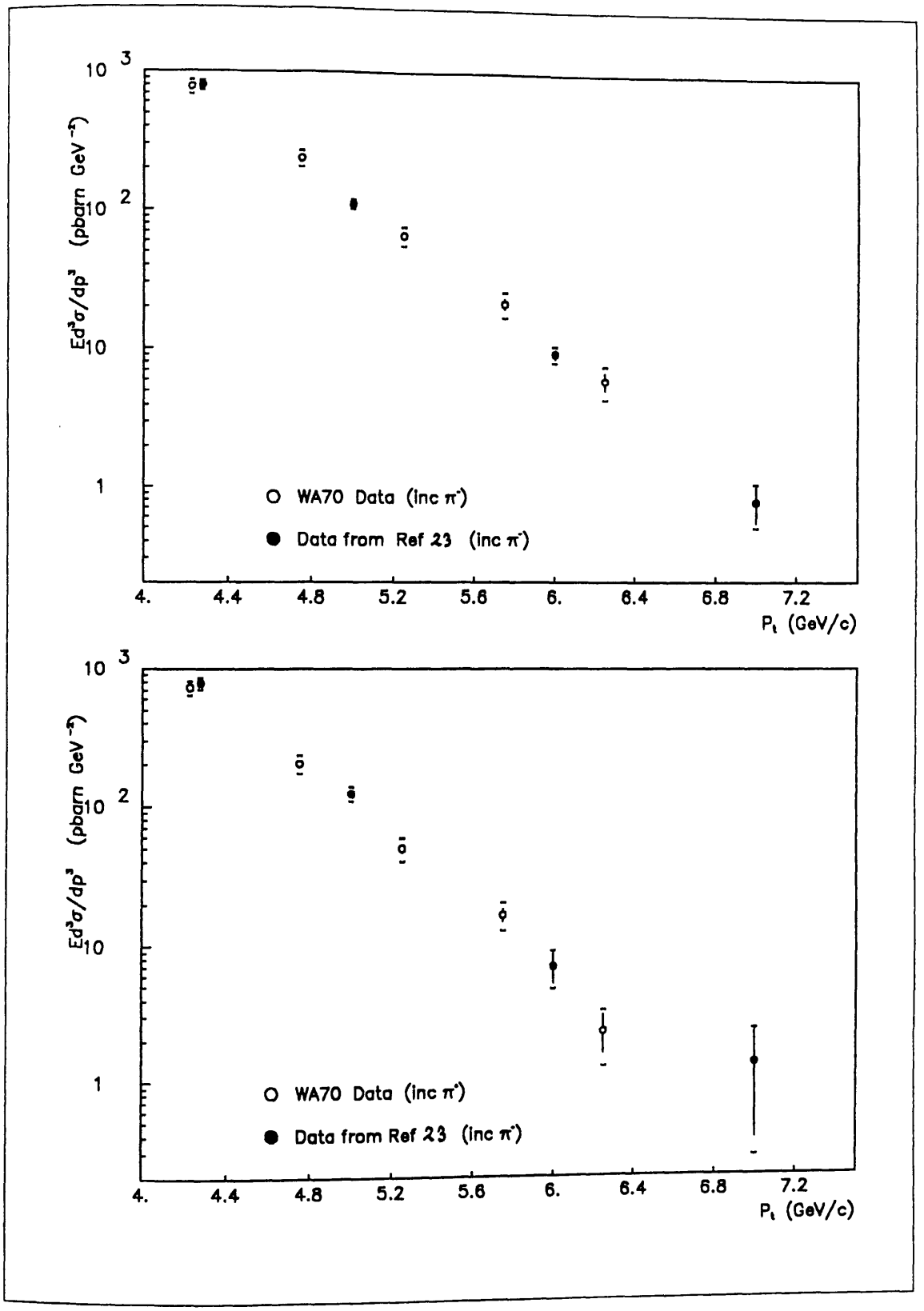

Figure 38: $Ed^3\sigma/dp^3$ ($\pi^- p -> \pi^0 X$) as a function of P_t, for both WA70 and NA24 data

REFERENCES

[1] M. Bonesini et al. , A Lead – Liquid Scintillator Electromagnetic Calorimeter for Direct Photon Physics; Nuclear Instrumentation and Methods A261 (1987) 471 – 480

[2] M. Bonesini et al. , Prompt Photon Production by π^- and π^+ on protons at 280 GeV/c; presented at XXII Conference on HEP, Bari, 1985

[3] M. Bonesini et al. , Preliminary Results on High Transverse Momentum Prompt Photon and π^0 production by π^- and π^+ on protons at 280 GeV; presented at the XXIII International Conference on HEP, Berkeley, 1986

[4] M. Bonesini et al. , High Transverse Momentum Prompt Photon Production by π^- and π^+ on protons at 280 GeV/c; Zeitschrift fur Physik C 37, p535 1988

[5] M. Bonesini et al. , Production of High Transverse Momentum Prompt photons and neutral pions in proton-proton interactions at 280 GeV/c; CERN – EP/87 – 222, December 8th, 1987 (submitted to Z. Physik C)

[6] A. Maxwell , Ph.D Thesis, University of Glasgow

[7] M. Diakonou et al.; Physics Letters 87B (1979) p372

[8] M. Diakonou et al.; Physics Letters 91B (1980) p296

[9] M. Diakonou et al.; Physics Letters 91B (1980) p301

[10] R.M. Baltrusaitis et al.; Physics Letters 88B (1979) p372

[11] M. McLaughlin et al.; Physics Review Letters 51, p971 (1983)

[12] J. Badier et al.; Zeitschrift fur Physik C 31, p341 (1986)

[13] C. De Marzo et al.; Physics Review D 36, p8 (1987)

[14] R.M. Turnbull Journal of Physics G 14, p135 (1988)

[15] LLoydowen et al.; Physics Review Letters 45, p89 1980

[16] T. Akesson et al.; Zeitschrift fur Physik C 18, p5 1983

[17] Bailly et al.; Zeitschrift fur Physik C 22, p119 1984

[18] Ajinenko et al.; Zeitschrift fur Physik C 35, p7 1987

[19] Bailly et al.; Zeitschrift fur Physik C 35, p295 1987

[20] J. Badier et al.; Zeitschrift fur Physik C 30, p45 1986

[21] T. Akesson et al.; Physics Letters 158 B, p282 1985

[22] A.L.S. Angelis et al.; Physics Letters 185 B, p213 1987

[23] C. De Marzo et al; Physics Review D 36 (1987) p16

[24] M. Aguilar – Benitez et al.; Zeitschrift fur Physik C 34, p419 1987

[25] W. Beusch ; CERN/SPSC/77 – 70, SPSC/T – 17 (1st August 1977)

[26] C. Bovet et al. ; CERN yellow report 82 – 13

[27] M. Bonesini et al. , Study of the Performance of a Large Sample of Phillips Photomultipliers type XP2972; Nuclear Instrumentation and Methods A264 (1988) 205 – 212

[28] M. Bonesini et al. , A 1152 Channel Timing System for an Electromagnetic Calorimeter Readout; Nuclear Instrumentation and Methods A263 (1988) 325 – 332

[29] P. Bene et al. , High P_t Trigger Electronics for a Large Orthogonal Readout Electromagnetic Calorimeter; CERN – EP/87 – 200, November 3rd, 1987 (submitted to Nucl. Instrum. Methods)

[30] J. Anthonioz – Blanc et al. ; CERN – DD/81/9

[31] J.C Lassalle et al. , TRIDENT: A Track and Vertex Identification Program for the CERN OMEGA Particle Detector System; Nuclear Instrumentation and Methods 176 371 (1980)

[32] R.K. Bock et al. , Parametrization of the Longitudinal Development of Hadronic Showers in a Sampling Calorimeter; Nuclear Instrumentation and Methods 186 533 (1981)

[33] Review of Particle Properties; Physics Letters, vol. 111B, April 1982

[34] M. Bonesini et al. , Calibration of an Electromagnetic Calorimeter for Direct Photon Physics; CERN – EP/87 – 227 November 3rd, 1987 (submitted to Nucl. Instrum. Methods)

[35] G. Donaldson et al. (Phy. Let. 73B; 375, 1978)

APPENDIX A
THEORETICAL BACKGROUND

A.1 Introduction

It is nowadays generally accepted that the interactions between hadrons can be described in terms of Quantum Chromodynamics (QCD) [1]. Hadrons are considered to be made up of quarks, which interact with one another via gluons, the massless propagators of the strong force. Both quarks *and* gluons carry a strong charge, so that gluons not only couple to quarks, but also to each other. In addition to a strong charge, quarks carry an electric charge, and can therefore interact with other charged objects via the electromagnetic force.

Currently five different types (flavours) of quark, together with the corresponding antiquarks, are known to exist. They all have the same amount of strong charge, but differ in the quantity of electric charge that they carry – either 2/3e or −1/3e, where e is the electron charge (the antiquarks carry the opposite charge to their quark counterparts).

An important aspect of the theory is that the strong coupling constant α_S (which determines the strength of the interaction), varies with the energy of the interaction according to the formula

$$\alpha_S(Q) = 12\,\pi/(33-2f)\ln(Q^2/\Lambda^2)$$

where Q^2 is the momentum transfer between the interacting particles, Λ is a parameter of the theory, and f is the number of quark flavours. At high values of Q^2, α_s may become small enough (less than 1) that perturbation techniques can be used to make calculations within the framework of QCD (this is known as asymptotic freedom).

The theoretical situation relating to the scale parameter Λ, and the energy scale Q^2, is complex; if QCD calculations could be made exactly, to all orders of α_s, there would be no problem, since the results would be independent of the choice of scales. Where calculations are only made to first or second order, the way in which the Q^2 and Λ are treated affects the results. As a consequence, it is difficult to derive a value for Λ from experimental results. Estimates are generally around 100 to 400 MeV, but this allows for large variations in subsequent QCD calculations.

A second important aspect of QCD is quark confinement. To date, it appears that quarks and gluons cannot be produced in the free state, but exist only in combination with other quarks. This is explained by the theory in terms of the form of the strong interaction. As two quarks (for instance) move away from each other, the force of interaction between them increases. This implies that the bond between them becomes more energetic with increasing separation. When there is sufficient energy, a new quark anti-quark pair can be created. One of the original quarks may then combine with one of the new quarks to form a hadron. Depending on the energy taken by the newly created hadron system, the two remaining quarks may have enough momentum to continue separating, in which case the process can repeat itself, creating more hadrons. The process stops when there is no longer sufficient energy to create new quark-antiquark pairs.

The same theory applies whether the partons involved are quarks or gluons, and is known as fragmentation [2] [3]. The likelihood of a parton p , with energy E, producing a hadron h, with energy E′, is given by the function $D_p^h(z)$, where $z = E'/E$ is the fraction of the parton's energy taken by the hadron. The fragmentation functions cannot currently be calculated from the QCD, but must be derived in some other fashion.

A.2 Hard Scattering Interactions

Hadron-hadron interactions resulting in the production of a high transverse momentum (high P_t) particles can be explained in terms of hard scattering, where the basic interaction is between two strongly charged partons, one from each hadron [2] [4]. The remaining quarks play no real role, and are referred to as spectator quarks.

The process produces two partons, emerging back to back from the interaction region. The partons are generally quarks or gluons, since the probabilities for electromagnetic interactions (eg direct photon production, or lepton pair production) are suppressed by the weakness of the electromagnetic coupling compared to the strong coupling. Any strongly charged parton produced will fragment into a jet of hadrons, the total P_t of which will be the same as the P_t of the parent parton. The spectator quarks fragment into hadrons with much lower average P_t. Figure A1 a) shows this process diagrammatically. The central bubble represents the hard scattering interaction. Figure A1 b) shows some of the Feynman diagrams for the simplest hard scattering interactions that can contribute (in these, quarks are represented by straight lines, while gluons are represented by lines with loops).

The cross section for the inclusive production of high P_t particle C from incident particles A and B is given by the expression [4]

$$E_c \frac{d^3\sigma}{dp_c^3} = \sum_{abcd} \int dx_a\, dx_b \frac{dz_c}{z_c^2}\, G_a^A(x_a)\, G_b^B(x_b)\, D_c^C(z_c)\, \delta(s'+t'+u')\, \frac{s'}{\pi}\, \frac{d\sigma'}{dt'}$$

where the D_p^h are the fragmentation functions discussed in the section A.1. The functions $G_p^h(z)$ give the probability of a parton p inside a hadron h having a fraction z of the hadron's total momentum (these functions cannot yet be calculated, but some have been measured experimentally – for instance, in deep inelastic scattering) [4]. The variables s', t' and u' are the Mandelstam variables for the hard scattering process. The expression $d\sigma'/dt'$ is the cross section for the hard scattering process, and can be derived from QCD. As an example, the first order expression for the scattering of two quarks by a gluon, $q_1q_2 \rightarrow q_1q_2$ is [5]

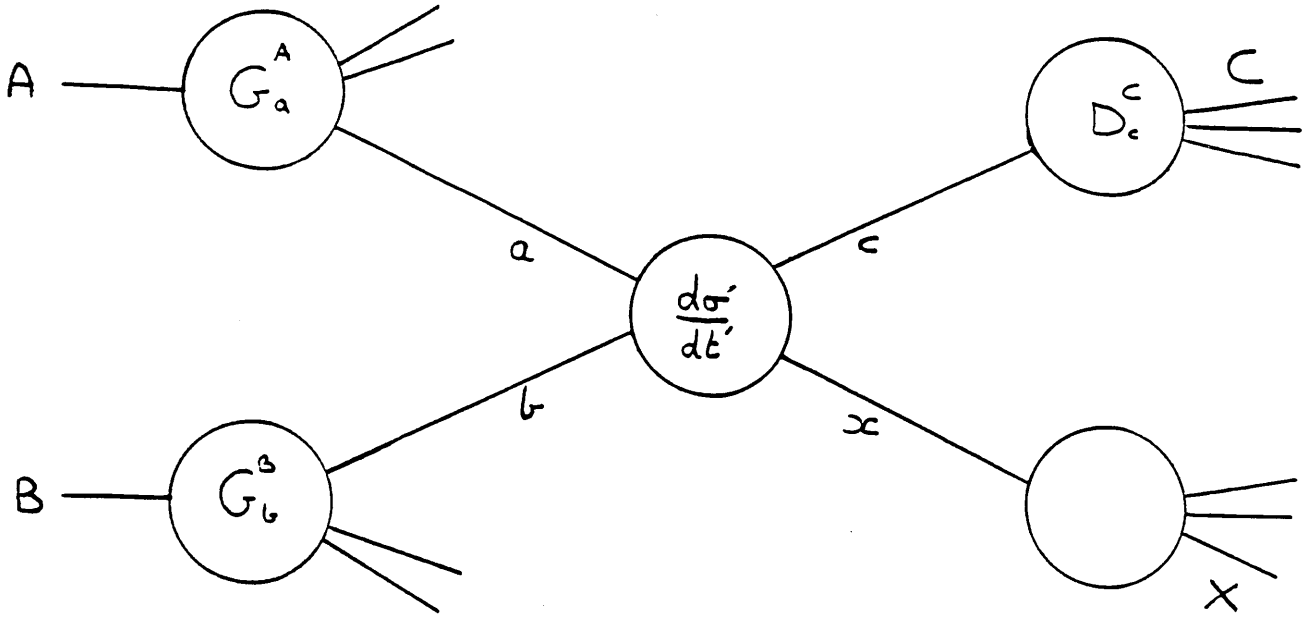

a)

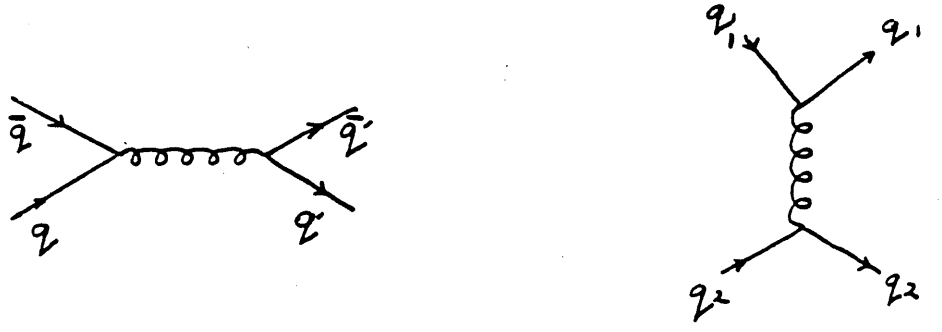

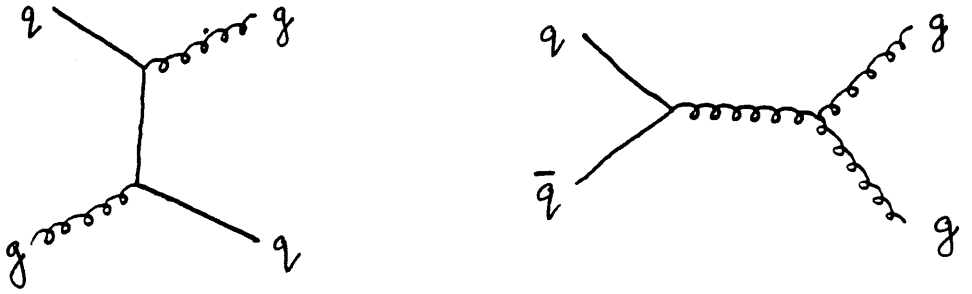

b)

Figure A1: Hadron-hadron hard scattering interaction

$$\frac{d\sigma'}{dt'} = \frac{\pi \alpha_s^2}{s'^2} \cdot \frac{4}{9} \frac{s'^2 + u'^2}{t'^2}$$

In principle $d\sigma'/dt'$ should be calculated by considering the contributions from all possible Feynman diagrams. However, calculating the contributions of higher order diagrams is difficult in QCD, and in general approximations are made by only taking into account those orders which make a significant contribution to the cross section.

At the energies and P_t currently reachable, the value of the coupling constant α_s is around 0.2 . This is large enough that second order corrections (at least) are important. Figure A2 a) shows a few of them.

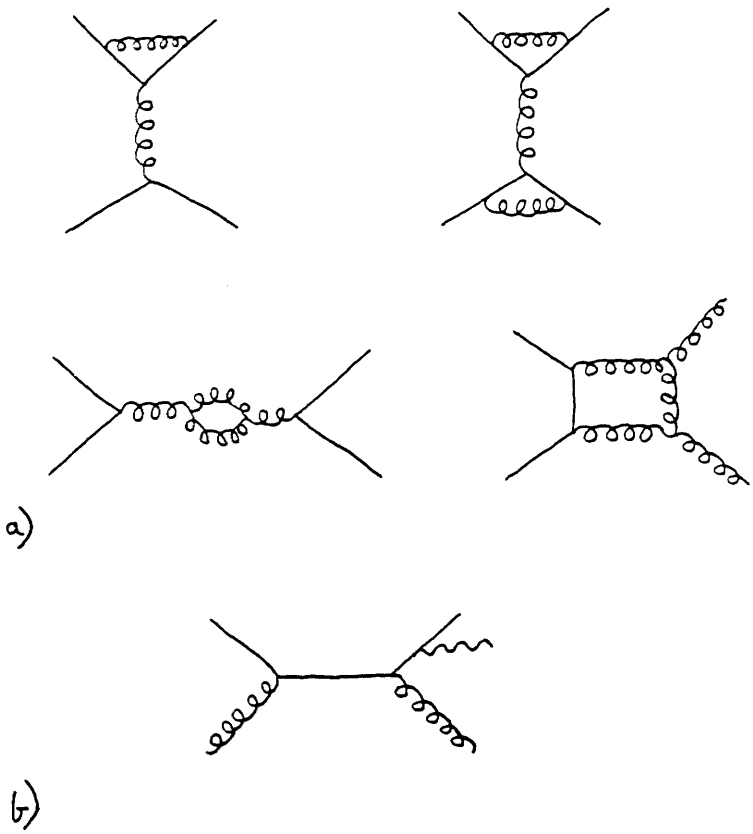

Figure A2: Some higher interactions

A.3 Direct Photons

Two further possible (first order) diagrams contributing to the hard scattering process discussed in the previous section are given in figure A3. In these processes a photon is produced, via the electromagnetic interaction. The coupling constant relevant to the second vertex in the diagrams is α (the electromagnetic coupling constant), rather than α_s, and the charge involved is the quark's electric charge, e_q, rather than its strong charge, g.

The cross section for the inclusive production of direct photons from the incident particles A and B at an angle θ (center of mass frame) is given by the expression [6]

$$E\frac{d^3\sigma}{dp^3} = \int_{x_a^{min}}^{1} dx_a \, G_a^A(x_a) \, G_b^B(x_b) \frac{x_b^2}{\pi x_2} \frac{d\sigma'}{dt'}$$

where

$$x_1 = \tfrac{1}{2} x_T \cot\left(\tfrac{\theta_{cm}}{2}\right) \quad , \quad x_2 = \tfrac{1}{2} x_T \tan\left(\tfrac{\theta_{cm}}{2}\right)$$

$$x_a^{min} = \frac{x_1}{(1-x_2)} \quad , \quad x_T = \frac{2P_T}{\sqrt{s'}}$$

(it is assumed that the quarks have no mass, and that the incoming partons have no momentum transverse to their parent's trajectories).

The expresion for $d\sigma'/dt'$ can again be derived from theory (QCD and QED) and for the first order quark annihilation process $q\bar{q} \rightarrow g\gamma$ (figure A3), it is [7]

$$\frac{d\sigma'}{dt'} = e_q^2 \frac{8}{9} \frac{\pi \alpha \alpha_s}{s'^2} \cdot \frac{t'^2 + u'^2}{t'u'}$$

It can be seen by comparing theexpressionsfor the cross sections for the production of high P_t hadrons, and for the production of high P_t photons, that the calculations for the lat-

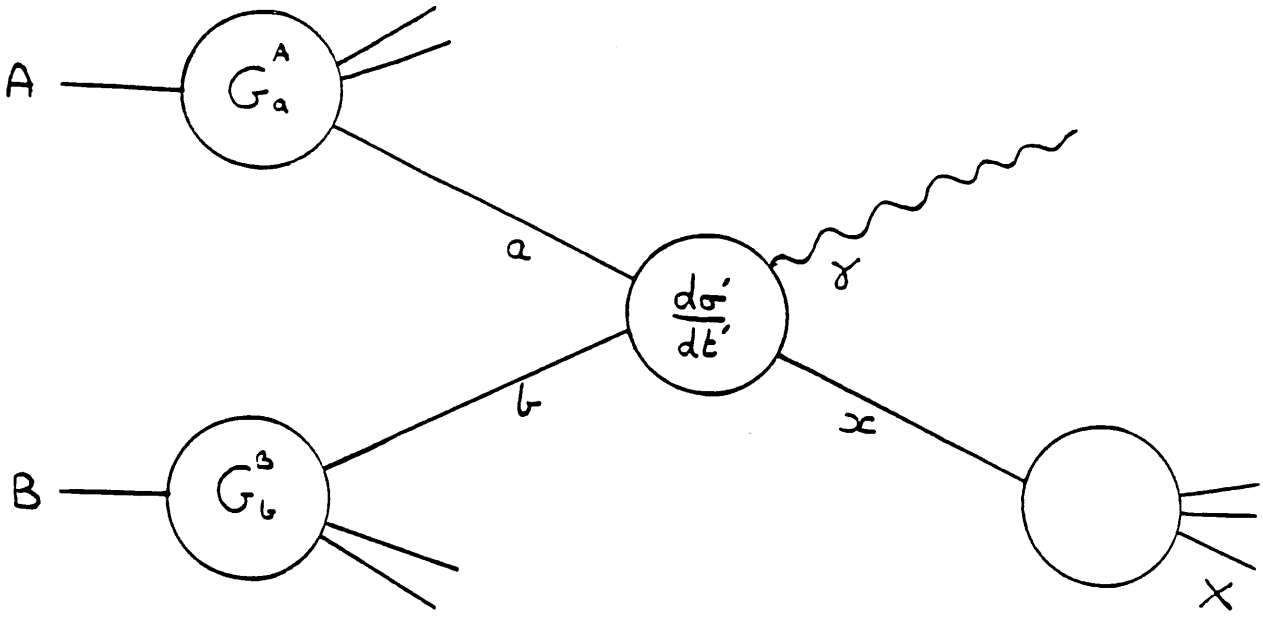

a)

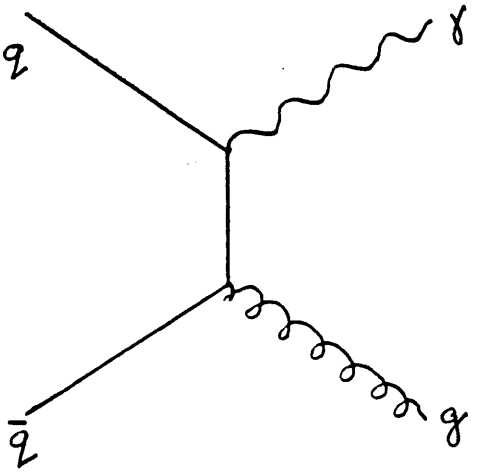

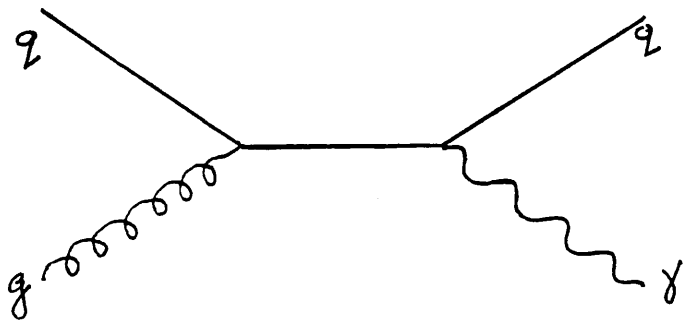

b)

Figure A3: Direct photon production

ter are much simpler, since they do not include the D_p^h functions. In addition, the contribution from the (poorly understood) strong force is of order α_s only, rather than α_s^2 as in section A.2. In practice, this means that the direct photon acts as a clean probe into hard scattering interactions, and that the comparison of theory with experimental results is much simpler here than in other hard scattering experiments.

Higher order diagrams must again be taken into account in making the final cross section calculations. One source of higher order correction are the bremsstrahlung graphs, where the direct photon is emitted as bremsstrahlung from a charged object, rather than as one of the components of the underlying first order diagrams. These graphs may contribute to the direct photon cross section by up to 30%. An example is shown in figure A2 b).

As with ordinary hard scattering, the calculations for higher order contributions are difficult. Often they are given simply as factors, calculated from just the more important types of higher order graphs. These are known as K factors; their values depend very much on how the calculations are made, and whether they are given as constants or as functions of P_t, but are (very) approximately 2 [8] [9] [10].

The exact results of cross section calculations depend strongly on what assumptions are made. The 'variables' include the scales of Λ and Q^2 chosen for the QCD calculations, and the choice of parton distributions within the parent hadrons (the G_p^h functions). However, the general results are qualitatively similar to those given by considering both the lowest order interactions, and the general form of the G_p^h functions.

For instance, the direct photon cross sections for π^-p interactions are expected to be similar to those for π^+p interactions at low P_t, whilst at high P_t the π^-p cross section will be larger. This is because the momentum distribution functions, G_p^h, for the proton are such that the gluons are dominant at low z, while the quarks are dominant at high z. Thus at low P_t, the compton process ($qg -> q\gamma$) dominates, whilst at high P_t the annihilation process ($q\bar{q} -> g\gamma$) dominates. Moreover, the proton has two u-flavour quarks to annihilate with the π^-'s $\bar{u}$ quark, but only one d-flavour quark to annihilate with the π^+'s $\bar{d}$ quark.

A useful theoretical prediction is the ratio of the direct photon cross section to the π^0 cross section. The desirability of measuring this quantity is the fact that it can remove the experimental uncertainties in the normalisation and (to an extent) the energy scale. The ratio is predicted to increase with P_t, as in figure A4. The main reason for this behaviour is that the photon always emerges from the interaction region with the P_t of the hard scattering process, while the P_t of the opposing hadron jet must be split between the hadrons during fragmentation.

Both of the above predictions are born out by experiment [11] [12].

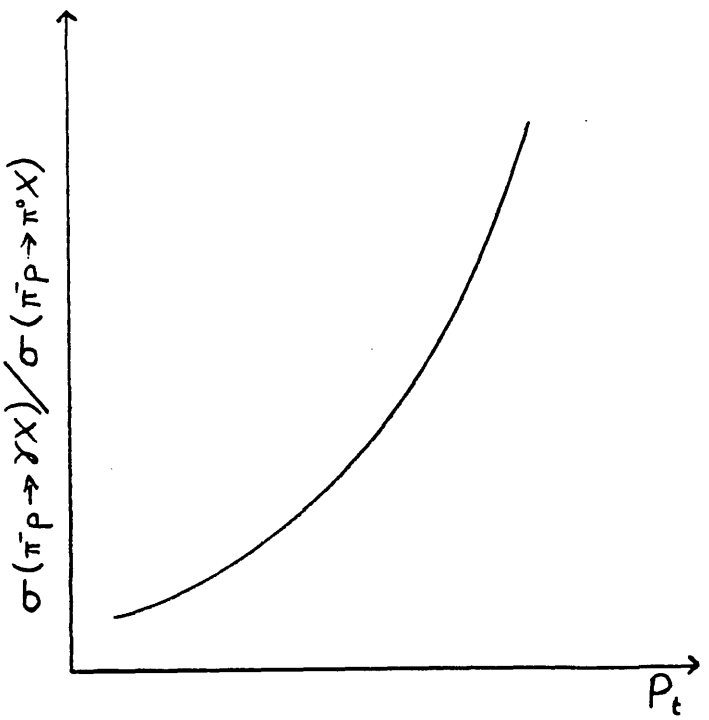

Figure A4: Ratio of direct photon cross section to π^0 cross section

REFERENCES

[1] D.Lichtenberg , Quantum Chromodynamics; Contemporary Physics 22, p311 1981

[2] E.Reya , Perturbative Quantum Chromdynamics; Physics Reports 69 p195 1981

[3] R.D.Field, R.P.Feynman, A Parameterisation of the Properties of Quark Jets; Nuclear Physics B136, p1 1978

[4] D.Sivers et al. ; Physics Reports 23C, p1 1976

[5] B.Combridge et al. , Physics Letters 70B, p234 1977

[6] E.L.Berger et al. , Large P_t Production of Single and double Photons in Proton-proton and Pion-Proton Collisions; Nuclear Physics B239, p52 1984

[7] A.P.Contogouris et al. , Direct Photon Production by Positive and Negative Pion Beams; Physical Review D32 p1134

[8] A.P.Contogouris et al. , Soft Gluon Corrections to Large P_t Direct Photon and Dilepton Production; Physics Letters B104, p70 1981

[9] P.Aurenche et al. , Dealing with Ambiguities in Higher Order QCD Predictions for Large P_t Porcesses Involving Real Photons; Nuclear Physics B286, p509 1987

[10] P.Aurenche et al. , Scheme Invariant Higher Order QCD Predictions for Large P_t Photoproduction Reactions; Nuclear Physics B286, p553 1987

[11] C. De Marzo et al.; Physics Review D 36, p8 (1987)

[12] M. Bonesini et al. , High Transverse Momentum Prompt Photon Production by π^- and π^+ on protons at 280 GeV/c; Zeitschrift fur Physik C 37, p535 1988

APPENDIX B
ABSOLUTE ENERGY CALIBRATION OF THE CALORIMETER FOR ELECTRONS

B.1 Introduction

The following aspects of the calorimeter performance were taken into account when studying its calibration: – the linearity of the electronics associated with each channel (PMs and ADCs), the overall linearity of the calorimeter response, the energy resolution, the accuracy to which the absolute energy scale is known, and the variation of that scale over the calorimeter. They are considered separately in the following sections.

B.2 Linearity of the Channel Electronics

B.2.1 Response of the PM-ADC chain

The calorimeter's laser system [1] has a set of 7 filters between the laser and the light mixer. The accuracy of the filters is ± 1%, and they can be combined to pass between 0.03% and 100% of the incident light. Each PM-ADC channel was examined at the 32 different intensities allowed by the filters, and a fit made to the resulting data points. The fit was a third order polynomial, with deviations from linearity of generally less than 2%.
Figure B1 gives the results of a linear fit and the 3rd order polynomial fit on one channel, for just the low signals (a), and over the entire range (b). The fits were used to correct the calorimeter data before event reconstruction.

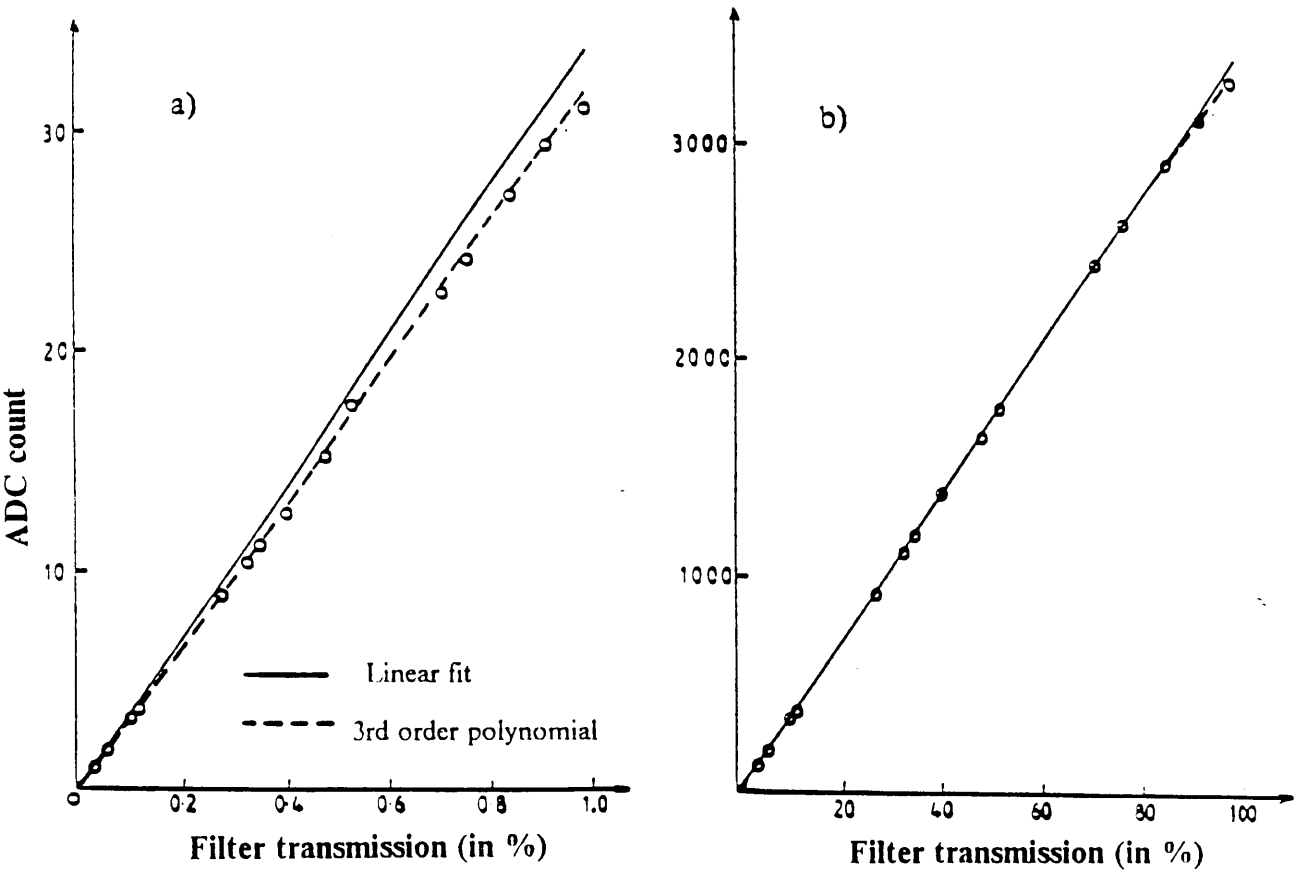

Figure B1: Plot of data and fit for intensity scan of a PM-ADC channel

B.2.2 Changes in the Gain of the PMs

A refinement to the correction described in section B.2.1 was made by measuring the effect of anode currents on the PM gains. During beam bursts, the anode current is higher than outside the beam burst, and this changes the tube's gain [2]. The laser system was used to measure the output from each channel, both inside and outside of the beam burst, from which the change in gain could be derived. The effect near the beam was about 3%, and decreased for PMs further away.

B.3 Calorimeter Response at Different Energies

The reponse of the calorimeter at different energies was measured using an electron beam at three energies – 10 GeV/c, 20 GeV/c and 50 GeV/c. Quadrant 2 was examined.

To direct the electron beam onto the quadrant, the test was made with the OMEGA magnetic field switched on. The three measurements were consequently made at three fixed positions, one for each energy (the positions being determined by the degree of bending of the beam as it passed through the magnetic field).

The electron showers were reconstructed by PATREC, and the average energy (from all three segments combined) compared with the beam energy. The segments could not be examined individually, since electromagnetic showers do not deposit enough of their energy in the second and third segments for a reliable study.

It was found that the plot of average shower energy against beam energy was linear, within the uncertainties of the beam momentum determination (approximately 1%).

B.4 Energy Resolution of the Calorimeter

The energy resolution was examined using two data sets – the electron data used in the linearity test discussed in section B.3, and data from hadron-hadron interactions.

The data was also treated in two different ways. One method was to examine the spread in shower energies. This can be done for the electron data only, since it is the only data set where the shower energies are known (from the beam momentum). The resolution was parameterised in terms of two constants, C_1 and C_2, with the equation

$$(\sigma_e/E)^2 = C_1^2/E + C_2^2$$

The second method treats the shower projections onto the Y and Z co-ordinates as two different measurements of the same value. The quantity D_{energy} can be defined as

$$D_{energy} = (E_y - E_z)/(E_y + E_z)$$

and the spread on this quantity is

$$\sigma_{de} = \sigma_e/E$$

(ignoring any correlation in the errors for E_y and E_z). σ_{de} can therefore be used to calculate σ_e. It was parameterised with the same expression used for σ_e/E:

$$(\sigma_{de})^2 = K_1^2/E + K_2^2$$

where $K_1 = C_1$ and $K_2 = C_2$ if E_y and E_z have the same average energies, and uncorrelated errors.

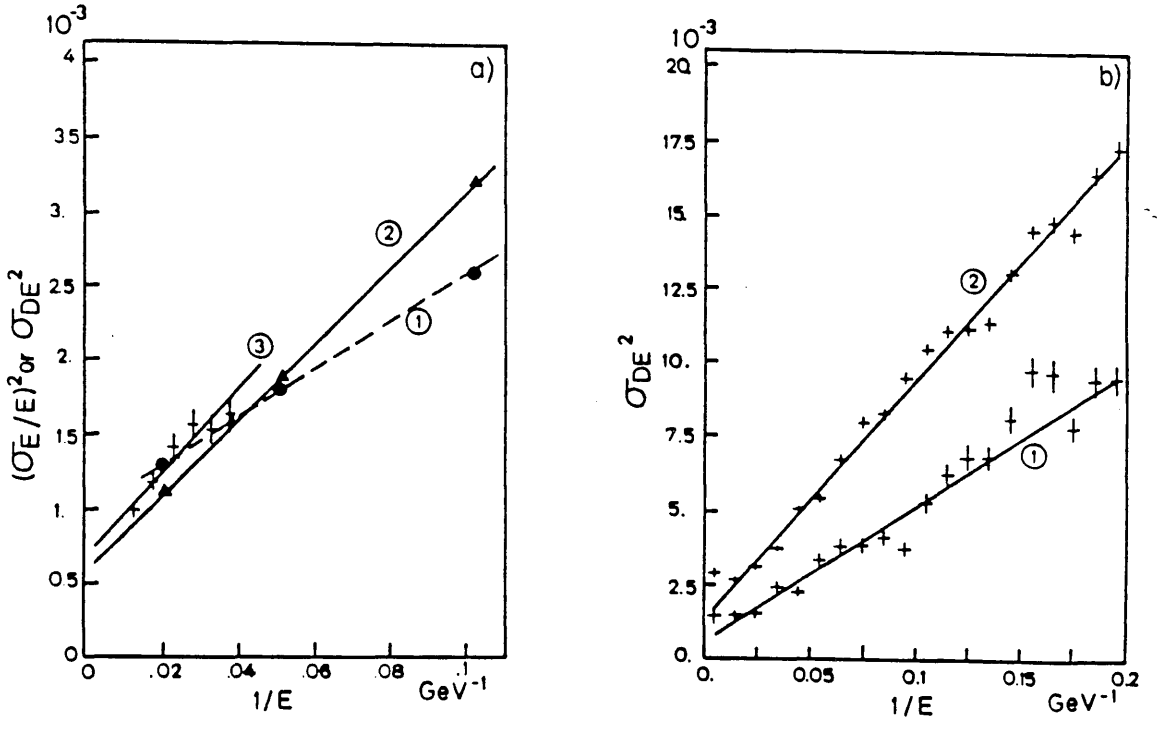

Figure B2: Energy resolution of calorimeter as a function of energy

The values derived for the C and K parameters from the electron data are

$C_1 = 0.126 \pm 0.004$, $C_2 = 0.032 \pm 0.0005$

$K_1 = 0.161 \pm 0.003$, $K_2 = 0.024 \pm 0.001$

The data is plotted in figure 2 a), curves 1 and 2 respectively.

The data for hadron-hadron interactions is shown in figure 2 a) for isolated trigger showers (curve 3) and in figure 2 b) for isolated showers (curve 1) and all showers (curve 2). The plots correspond to calculations of the K parameters only. The values of the parameters are:

$K_1 = 0.167 \pm 0.008$, $K_2 = 0.026 \pm 0.001$ (trigger showers)

$K_1 = 0.216 \pm 0.002$, $K_2 = 0.024 \pm 0.001$ (isolated showers)

$K_1 = 0.284 \pm 0.001$, $K_2 = 0.036 \pm 0.003$ (all showers)

B.5 Variations in Response Across the Calorimeter

The variation of the energy calibration across the calorimeter was studied by plotting the π^0 mass as a function of the Y and Z co-ordinates. It was found that the mass varied by about 5% across a quadrant.

This effect was corrected for by calculating a gain correction, dG to be applied to each detector channel as a function of Y and Z. The correction was linear:

$$dG = a + bY + cZ$$

where the parameters a, b, and c differ for each co-ordinate projection (Y or Z) and quadrant.

dG is a function of Y *and* Z so that it can correct for systematic errors both in the equalisation of the detector channels, *and* in the attenuation length [3] of the scintillator.

B.6 Absolute Energy Scale

The absolute energy scale was set by adjusting the overall scale until the mass of the η peak was at the accepted value for the η mass, 548.8 GeV. A check was made using conversion electrons, that is, e^+e^- pairs from photons that had converted in the material between the target and the calorimeter. The electron energy was calculated both from the calorimeter reconstruction and from the track detected in the OMEGA wire chambers. Figure 3 shows the ratio of the two energies. The average of this ratio deviates from 1.0 by 0.6%. This was taken as the accuracy of the absolute energy scale.

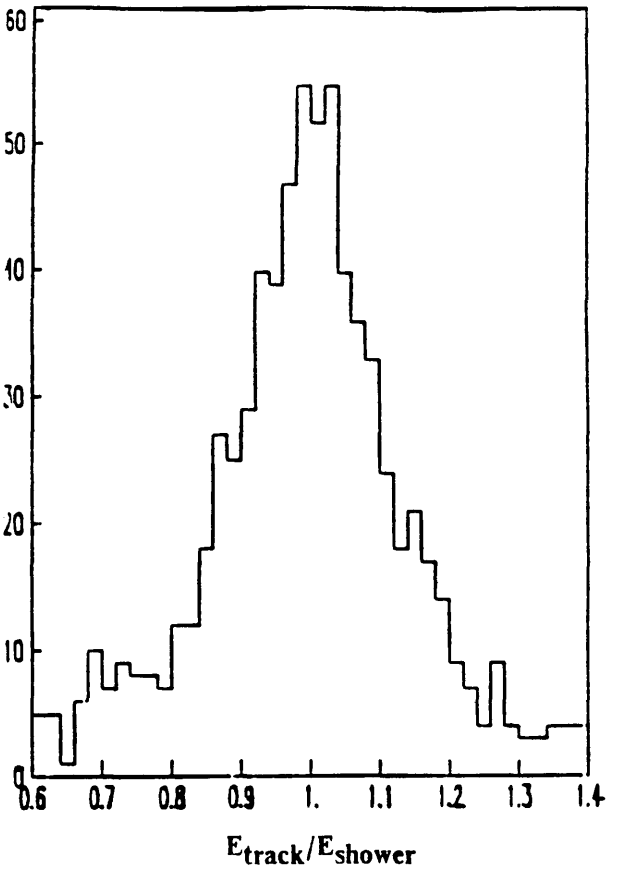

Figure B3: Ratio of electron energy from track data to electron energy from shower data

REFERENCES

[1] M. Bonesini et al. , Calibration of an Electromagnetic Calorimeter for Direct Photon Physics; CERN – EP/87 – 227 November 3rd, 1987 (submitted to Nucl. Instrum. Methods)

[2] M. Bonesini et al. , Study of the Performance of a Large Sample of Phillips Photomultipliers type XP2972; Nuclear Instrumentation and Methods A264 (1988) 205 – 212

[3] M. Bonesini et al. , A Lead – Liquid Scintillator Electromagnetic Calorimeter for Direct Photon Physics; Nuclear Instrumentation and Methods A261 (1987) 471 – 480